



Università
Ca' Foscari
Venezia

**Scuola Dottorale di Ateneo
Graduate School**

**Dottorato di ricerca
in Scienze Chimiche
Ciclo XXV
Anno di discussione 2013**

***Synthesis and Functionalization of Metal Oxide
Nanostructures for Photoelectrochemical Energy
Conversion***

**SETTORE SCIENTIFICO DISCIPLINARE DI AFFERENZA: CHIM/01
Tesi di Dottorato di Michael Ongaro, matricola 955754**

Coordinatore del Dottorato

Prof. Maurizio Selva

Tutore del Dottorando

Prof. Paolo Ugo

Contents

<i>List of Abbreviations</i>	<i>i</i>
<i>Estratto</i>	<i>iv</i>
<i>Abstract</i>	<i>iv</i>
1. General Introduction	1
1.1 THE ENERGY PROBLEM	1
1.1.1 <i>Solar energy as possible alternative</i>	2
1.2 PHOTOELECTROCHEMISTRY WITH SEMICONDUCTOR ELECTRODES	4
1.2.1 <i>The band model in solids</i>	4
1.2.2 <i>The Fermi level</i>	7
1.2.3 <i>Semiconductor-electrolyte junctions</i>	7
1.2.4 <i>Photoelectrochemical water splitting</i>	13
1.3 SEMICONDUCTOR NANOSTRUCTURED MATERIALS	15
1.4 METHODS TO OBTAIN 1-D NANOSTRUCTURES	17
1.4.1 <i>Directional nucleation growth</i>	17
1.4.2 <i>Template synthesis</i>	19
1.5 GOAL OF THE THESIS.....	21
2. Template Synthesis and Characterization of TiO₂ Nanofibres	27
2.1 INTRODUCTION	27
2.2 EXPERIMENTAL	30
2.3 RESULTS AND DISCUSSION	34
2.3.1 <i>Alumina membranes as template</i>	34
2.3.2 <i>Polycarbonate as template</i>	39
2.4 CONCLUSIONS	48
3. Linear and Hierarchically Branched ZnO Nanofibers	52
3.1 INTRODUCTION	52
3.2 EXPERIMENTAL	54
3.3 RESULTS AND DISCUSSION	59
3.4 CONCLUSIONS	74
4. Asymmetrical Modification of Micro and Nanofibers by Bipolar Electrochemistry	77
4.1 INTRODUCTION TO BIPOLAR ELECTROCHEMISTRY.....	77
4.2 EXPERIMENTAL	80
4.3 RESULTS AND DISCUSSION	83
4.4 CONCLUSIONS	98
5. Concluding Remarks	101
Appendix A	103
BASICS OF EBSD	103
Appendix B	106

List of Abbreviations

3D-NEE	Three dimensional ensemble of nanoelectrodes
AcAc	Acetylacetone
AM	Air mass coefficient
AAM	Anodic alumina membrane
BPE	Bipolar electrochemistry
CABED	Capillary-assisted bipolar electrodeposition
CB	Conduction band
CMF	Carbon microfiber
CV	Cyclic voltammetry
CVD	Chemical vapor deposition
d	Spacing of the diffraction plane
d	Diameter
DMBA	Dimethylamineborane
DSSC	Dye sensitized solar cell
e^-	Electron
E	Potential / Electric field
E	Energy
E^0	Standard potential
$E_{1/2}$	Half wave potential
EBS	Electron backscatter diffraction
E_C	Conduction band lower energy level
EDX	Energy dispersive X-ray spectroscopy
E_F	Fermi level
E_{Fp}^*	Quasi-Fermi level for holes
E_{Fn}^*	Quasi-Fermi level for electrons
E_g	Energy gap
EMF	Electromotive force
E_{pb}	Backward peak potential
E_{pf}	Forward peak potential
E_{redox}	Electrochemical potential of a generic redox couple
E_V	Valence band upper energy level

Fc	Ferrocene
FEG-ESEM	Field emission gun environmental scanning electron microscopy
h	Planck constant
h^+	Hole
HMTA	Hexamethylenetetramine
i	Current
i_p	Current flowing through the substrate in open bipolar electrochemistry
i_s	Current flowing through the solution in open bipolar electrochemistry
IR	Infrared
j	Current density
j_{ph}	Photocurrent density
k	Boltzman constant
ITO	Indium tin oxide
l	Length
LSV	Linear sweep voltammetry
MEMS	Micro-electromechanical systems
MF	Microfiber
MWCNT	Multi walled carbon nanotubes
n	Electron density in the conduction band
N_A	Acceptor level density
N_C	Conduction band state density
N_D	Donor level density
NF	Nanofiber
NEE	Nanoelectrode ensemble
NHE	Normal hydrogen electrode
NMR	Nuclear magnetic resonance
NP	Nanoparticle
N_V	Valence band state density
NW	Nanowire
p	Hole density in the valence band
PANI	Polyaniline
PC	Polycarbonate
PEC	Photoelectrochemical cell
PECVD	Plasma enhanced chemical vapor deposition

PPy	Polipyrrole
PT	Polythiophene
r	Radius
RF	Radio frequency
SEM	Scanning electron microscopy
t	Time
TEA	Tetraethylammonium
TEM	Transmission electron microscopy
TGA/DSC	Thermogravimetric analysis / differential scanning calorimetry
TPO	Temperature programmed oxidation
TTiP	Titanium tetraisopropoxide
UV	Ultraviolet
v	Scan rate
VB	Valence band
V_{fb}	Flat band potential
XRD	X-ray diffraction
ΔE_p	Separation between the peak potentials
ΔV	Potential difference
λ	Wavelength
ν	Frequency

Estratto

Questo lavoro di tesi ha l'obiettivo di sviluppare nuovi nanomateriali, a base di ossidi metallici ceramici semiconduttori, per applicazioni in campo energetico. I materiali sintetizzati sono stati impiegati per l'assemblaggio di elettrodi da impiegarsi per il *water-splitting* fotoelettrochimico. Nanofibre di TiO₂-anatasio sono state preparate mediante reazione sol-gel, impiegando membrane nano porose come agente direzionale di struttura (*template*). Nanofibre di ZnO, sono state invece preparate attraverso deposizione elettrochimica su elettrodi ITO trasparenti o, in alternativa, su *ensemble* di nanofili d'oro. Nel primo caso sono state ottenute fibre lineari, nel secondo fibre ramificate gerarchicamente. Queste ultime strutture, si sono dimostrate le più efficienti tra quelle sintetizzate in questa tesi rispetto alla fotossidazione dell'acqua, fornendo valori di fotocorrente 7 volte superiore rispetto ad elettrodi "classici", ricoperti di nano particelle di TiO₂. Infine, nell'ultima parte della tesi, è stata studiata la funzionalizzazione asimmetrica di particelle mediante elettrochimica bipolare. Tale tecnica è stata impiegata con successo nella deposizione asimmetrica di metalli e polimeri conduttori su substrati conduttori prima e, successivamente, su microfibre di semiconduttori. In quest'ultimo caso si è dimostrato come il processo di deposizione elettrochimica possa essere modulato attraverso l'irraggiamento delle nanofibre con luce UV.

Abstract

This thesis has the aim to develop new nanomaterials based on ceramic metal oxide semiconductors for energy applications. The synthesized materials were used for the assembly of electrodes to be used in the photoelectrochemical water-splitting reaction. TiO₂-anatase nanofibers were prepared by sol-gel reaction, employing nano-porous membranes as template. ZnO nanofibers, were instead prepared through electrochemical deposition on ITO transparent electrodes, or alternatively, on ensembles of gold nanowires. In the former substrate, linear nanofibers were obtained, in the latter, hierarchically branched fibers were obtained. Branched nanofibers have proven to be the most efficient among those summarized in this thesis, and have demonstrated efficiencies 7 times higher than that of conventional TiO₂ nanoparticle electrodes. In the last part of the thesis, we studied the asymmetric functionalization of microfibers by bipolar electrochemistry. This technique has been used successfully in asymmetric deposition of metals and conducting polymers on conductors and semiconductors microfibers. In the latter case, has been demonstrated that the electrochemical deposition, can be modulated by UV irradiation.

1. General Introduction

1.1 The Energy Problem

The worldwide energy consumption per person has been increasing since the beginning of the industrial revolution. In fact, while the worldwide population has been experiencing a four-fold increment, the global energy consumption has been experiencing a 60-fold increase from 1870 to nowadays (reaching 142 TWh in 2008) [1]. It is expected that this value will increase by 50% (225 TWh) within 2035 [2]. Only the 18 % (2007) of this energy is produced by renewable sources, among these the 13 % is obtained by biomasses processing (mainly burning) and the residual 5 % by other renewable sources such as wind energy, hydroelectric, geothermic, photovoltaic, etc. Therefore more than 80% of the world's energy supply is still based on the use of hydrocarbons from fossil source, which is a finite source. Furthermore, during the hydrocarbons combustion, a number of pollutants are produced, such as: CO and partially combusted particles which are toxic for the biosphere, but also the products of the complete combustion SO₂, NO and CO₂. The former are involved in the processes leading to acid rain while the latter, although not being toxic, is the main cause of the greenhouse effect. The CO₂ concentration in the atmosphere has been increasing of the 25 % in the last century, leading to an increase of the global temperature estimated in 0.6±0.2 °C. According to the “Intergovernmental Panel on Climate Change” (IPCC), the global temperature will increase between 1.1 and 6.4 °C by 2100.

In addition to this, the fast depletion of the oil reserves leads to an increasing cost of the fossil fuels, which being exploited for almost all human activities, have a direct effect on the overall life cost. Besides that, since the largest oil reserves are located in politically unstable countries, the industrialized countries are more and more interested in finding competitive energy sources. Unfortunately, with the present technology, such an energetic source still does not exist, both in terms of energy production and of energy cost. In fact, the fossil fuels, besides being an abundant and valuable energetic source, are considered convenient energetic vector due to the easiness of storage, transport and to the high energy density (Energy / Volume).

1.1.1 Solar energy as possible alternative

It is clear how the reserves of fossil fuels won't be large enough to meet future demands. Possible solutions to meet the growing energy demand are basically two: the increase of the energy production by means of nuclear fission and, on the other hand, the increase in the use of renewable sources and development of technologies which would make such sources more cost effective by improving their harvesting efficiency. After the major damage suffered by the Fukushima nuclear power plant, from the earthquake and subsequent tsunami that hit Japan on March 11th 2011, which caused partial nuclear meltdowns, explicit critics over the instability of nuclear power plants have risen. Furthermore, uranium sources are just as finite as other fuel sources, and are expensive to mine, refine, and transport; moreover these processes produce a considerable amount of environmental waste (including greenhouse gases). Also from a political point of view, shipping nuclear waste internationally poses an increased potential threat to interception to nuclear terrorism. All of these lead to a fall in the worldwide nuclear output by 4.3%, the largest decline on record, on the back of sharp declines in Japan (- 44.3%) and Germany (- 23.2%) [2]. For such a reason, an increase attention is growing towards the use of renewable energy sources.

A renewable energy source is defined as a natural resource which: i) is replenished at an higher rate than it is consumed by anthropogenic activities; ii) is found in nature in inexhaustible quantities in the time scale of the human life. Among renewable sources, solar energy is attracting the higher attention from the scientific community and environmental political movements. The sun provides energy to the Earth in a quantity equal to 120'000 TW under the form of electromagnetic radiation. By covering 0.16% of the land surface with solar energy conversion systems having an efficiency of 10%, 20 TW of power would be obtained, such a quantity is much larger than the world's current energy needs [3]. The solar energy conversion is achieved mainly by four different routes: 1) obtaining electrical energy by means of thermal systems (the radiation heats the water in a reservoir in order to obtain a high-pressure steam which is then expanded in a turbine); 2) farming of biomasses to be used for the extraction of starting products for the refinement of fuels (biofuels); 3) the direct obtainment of electrical energy by the so-called photovoltaic cells, where light energy is used for the generation of electrical charges, which are separated by the potential built at a solid-solid junction; 4) the use of photoelectrochemical cells, where the separation of the photogenerated charges happens at

General Introduction

a semiconductor-electrolyte junction. Among the solid-solid junction cells, the silicon panels are by far the most common photovoltaic systems, making a good compromise in terms of efficiency and energy cost; however, they still aren't competitive, considering the much lower cost of the fossil fuels. Also photoelectrochemical cells exhibit several advantageous features, such as the facilitated junction formation at the electrolyte interface, low temperature processing, and scalability typically achieved by self-organized processes at the solid-liquid interface [4, 5]. In addition, photoelectrochemical cells can operate in photovoltaic [6-8] (for direct electric energy production) as well as in photoelectrocatalytic mode [9-12] (for the production of energy vectors, such as H₂), the latter being of particular importance because global energy consumption is dominated by the use of fuels for automobiles, compared to electricity [2].

As far as photovoltaic mode concerns, Dye Sensitized Solar Cells [13] (DSSC) are by far the most promising photoelectrochemical cells. DSSC, also known as Graetzel cell, was originally co-invented in 1988 by Brian O'Regan and Michael Graetzel at the University of Berkley and this work was later developed by the aforementioned scientists at the École Polytechnique Fédérale de Lausanne until the publication of the first high efficiency DSSC in 1991 [13]. At the moment an increasing number of publications are appearing in the literature, dealing with different components of the cells leading to a record efficiency of 12.3% [14]. DSSCs are constituted by a mesoscopic semiconductor electrode on the surface of which is adsorbed a photoactive dye. The incident photons are absorbed by the sensitizer dye which injects electrons to the semiconductor (further details on the functioning mechanism are reported in paragraph 1.2.3).



Figure 1.1. DSSCs modules commercialized by 3Gsolar Photovoltaic Ltd.

Despite showing encouraging improvements in the overall photoelectrochemical efficiency, these cells are still less efficient than conventional silicon cells, but their production cost is considerably lower, since the mesoscopic semiconductors commonly used are much cheaper than ultrapure crystalline silicon [15]. Nevertheless the commercialization of DSSC will be difficult unless the issues of efficiency and lifetime (durability) are overcome. The most important element of a photoelectrochemical cell is the photoelectrode. This element is constituted by a semiconductor material which absorbs incident light, giving rise to an electrochemical reaction at the electrolyte-semiconductor junction. Since the electrochemical behavior of semiconductor electrodes may be quite different with regard to conventional metallic electrodes, an in depth description of the mechanism involved in such electrochemical systems is required.

1.2 Photoelectrochemistry with Semiconductor Electrodes

1.2.1 The band model in solids

The crystal lattice in solids may be described by a chemical approach, considering a bulk material as a huge molecule formed by a quasi infinite number of atoms. Isolated atoms contain vacant and occupied atomic orbitals. When two atoms are combined, occupied bonding orbitals and unoccupied antibonding orbitals are formed. When this process is repeated for a very large number of times, the bonding and antibonding orbitals form continuous bands. The bonding orbitals form the valence band (VB) and the antibonding orbitals form the conduction band (CB). The bands are separated by a forbidden band of energies called band gap. The energy difference between the lowest edge of the VB and the upper edge of the CB is denoted as E_g (energy gap or band gap) and is measured in eV. The magnitude of E_g is closely related to the nature of the atoms constituting the material, on the structure of the crystal lattice and the atoms spacing inside that. In the CB the electrons are poorly bonded to the atoms and are free to move inside the lattice. Then a metallic behavior will be observed when CB and VB are partially overlapped or when $E_g \ll kT$, so that CB is partially filled with electrons. Metallic behavior is also observed in materials with partially filled VB (e.g., in metallic Li). In this case the electrons move in the VB by an electron hopping mechanism. This mechanism may also be described as a positive charge (holes) transport, so that holes are the charge carriers in the VB. For large E_g values, in materials where VB is completely filled and CB is completely

General Introduction

empty, there is no conductivity; but for relatively low E_g values, at high enough temperatures, electrons from the VB may be thermally excited to the CB. The excited electrons are free to move in the CB and similarly, the vacancy (hole) left behind in the VB may be filled by neighboring electrons, resulting in a positive charge transport. Therefore, the excitation of an electron from the VB to the CB, results in the production of two charged species with different mobility in the lattice: holes in the VB and electrons in the CB. In Figure 1.2 a representation of energy levels in solids is reported.

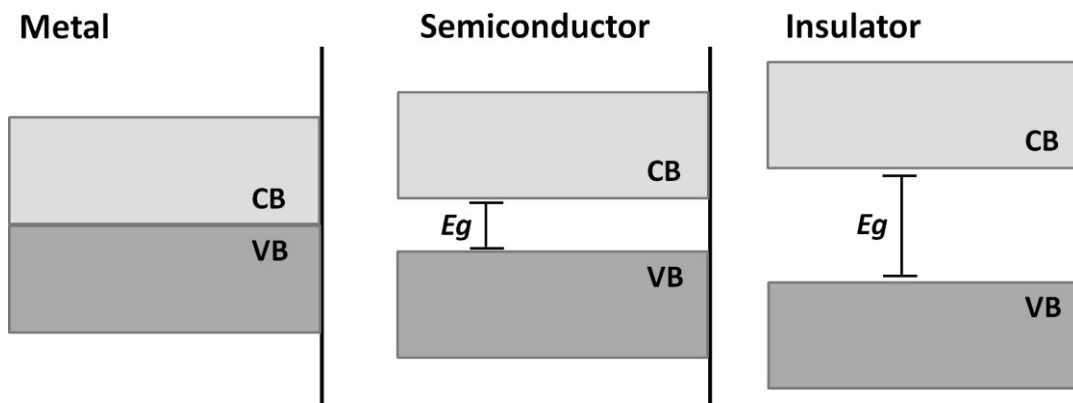


Figure 1.2. Electronic energy levels in solids. In a metal, VB and CB are overlapped or $E_g \ll kT$. Both in insulators and semiconductors, VB is completely filled and CB is completely empty, but in insulators E_g is small enough to allow promotion of electrons from VB to CB, in insulators instead, E_g is too large and electron promotion is practically not attainable.

When an undoped material shows semiconducting properties, it is called intrinsic semiconductor, still, energetic levels may be introduced in the lattice by doping the solid with different atoms, inducing semiconducting behavior in otherwise insulating materials. Dopants introducing energy levels close to the lower edge of the CB are called donors, since such shallow level states are easily ionized at room temperature, introducing electrons to the CB and leaving behind positively charge sites. Usually the concentration of dopants inside a material are in the order of magnitude of a few ppm.

Materials doped with electron donor impurities are called n-type extrinsic semiconductors. Since even in extrinsic semiconductors, electrons excitation from the VB occurs at a small extent at room temperature, the total density of electrons in the CB is given by:

$$n = p + N_D \quad (1.1)$$

General Introduction

where n is the electron density in the CB, p is hole density in the VB and N_D is the dopant density. But since usually $N_D \gg p$, $n \approx N_D$. For this reason, in n-type semiconductors electrons are the majority carriers, while holes are the minority carriers. Since the positive sites left behind by donor atoms are far away (from an energetic point of view) from the VB, they do not contribute to the overall conductivity.

When an insulating material is doped with electron accepting species, energetic levels slightly above the VB upper edge are introduced in the lattice and p-type semiconductors are obtained. In this case, electrons are thermally promoted from the VB to the shallow unfilled levels, leaving behind mobile holes in the VB. Again, the hole density p , in such a material, is given by:

$$p = n + N_A \quad (1.2)$$

Where N_A is the acceptor density. But since $N_A \gg n$, $p \approx N_A$. Therefore, in p-type semiconductors, holes in VB are the majority carriers and electrons in the CB are the minority carriers. If acceptor or donor levels are introduced in the middle of the band gap, they are called deep level impurities and do not contribute as much to the overall conductivity. In Figure 1.3 a schematic representation of the doping mechanism for n-type and p-type semiconductors is reported.

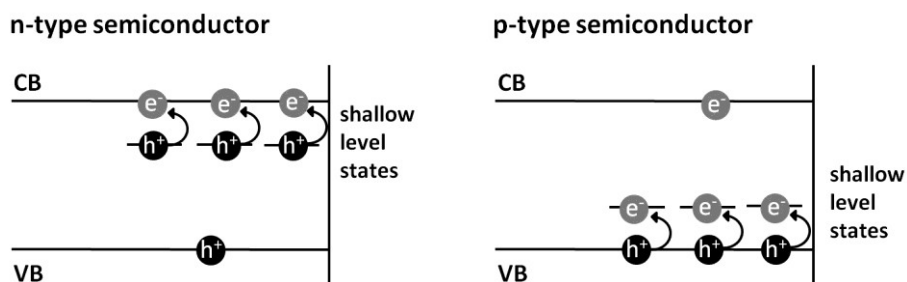


Figure 1.3. Schematic representation of the energy levels in n-type and p-type semiconductor.

In compound semiconductors, such as TiO_2 , ZnO or GaAs , whether the impurity substitutes a constituent atom of the material or occupies an interstitial position, determines if the impurity is a donor or an acceptor dopant. In this contest even vacancies in the lattice or broken bonds can be considered as dopants, since they are effectively acceptors. In fact TiO_2 is typically obtained as an n-type semiconductor because of oxygen vacancies in the

lattice. ZnO is also typically obtained as n-type semiconductor because of interstitial Zn atoms.

1.2.2 The Fermi level

The probability, $f(E)$, that an electronic level, E , is occupied by an electron at thermal equilibrium is given by the Fermi-Dirac equation:

$$f(E) = \frac{1}{1 + \exp\left(\frac{E - E_F}{kT}\right)} \quad (1.3)$$

where E_F is the Fermi level. The Fermi level is an energetic level for which $f(E) = 1/2$, i.e. the level where the probability that the level is occupied or unoccupied equals.

For an intrinsic semiconductor, where $p = n$, the Fermi level lies in the middle of the band-gap, midway between the CB lower edge and the VB upper edge. For an extrinsic semiconductor, instead, the location of the Fermi level depends on the extent of the doping, so that acceptors move the E_F towards the VB and donors move it towards the CB. The Fermi level may be calculated by the following equations:

$$E_F = E_C - kT \ln(N_C/N_D) \quad (\text{for n-type semiconductors}) \quad (1.4)$$

$$E_F = E_V + kT \ln(N_V/N_A) \quad (\text{for p-type semiconductors}) \quad (1.5)$$

Where N_C is CB state density, and N_V is the VB state density. Note that these equations are valid for $N_A < N_V$ and $N_D < N_C$, that is for moderate doping levels. For high doping levels, where such conditions are not met, the semiconductor become degenerate and the E_F moves into the CB or into the VB and the material starts to show metallic conductivity. For example, SnO₂ is a wide band gap semiconductor, that at high In doping level becomes degenerate and conductive.

1.2.3 Semiconductor-electrolyte junctions

When a semiconductor and an electrolyte solution are brought into contact an interface is created. If we consider an ideal semiconductor-solution interface, in order for

the two phases to be in equilibrium, their electrochemical potential must be the same. The electrochemical potential of the solution is determined by the redox potential of the electrolyte solution, while the electrochemical potential of the semiconductor is determined by the Fermi level. If the redox potential of the solution and the Fermi level do not lie at the same energy, a movement of charge between the semiconductor and the solution is required in order to equilibrate the two phases, until a common Fermi level is reached and an electrochemical equilibrium is attained. The consequent excess charge that is located on the semiconductor does not lie at the surface, as it would for a metallic electrode, but, since the charge carrier densities are much smaller, extends into the electrode for a significant distance (10- 1000 nm). This region is commonly named space charge region, and is associated with an electric field, which prevents further charge transfers.

For an n-type semiconductor electrode at open circuit, the Fermi level is typically higher than the redox potential of the electrolyte, and hence electrons will be transferred from the electrode into the solution. Therefore, there is a positive charge associated with the space charge region, and the depletion in electrons in this region is reflected in an upward bending of the band edges. Since the majority charge carrier of the semiconductor has been removed from this region, this region is also called depletion layer (Figure 1.4c).

If an external potential is applied to the semiconductor electrode, the Fermi level of the semiconductor is shifted, and the band edges in the bulk of the electrodes also shift accordingly to it. However, the energies of the bands at the interface are not affected by the applied potential, therefore the magnitude of the band bending varies with the applied potential. If the potential is made more positive than the open circuit potential, the interface is further depleted in electrons, and a situation can be eventually reached in which the hole density is greater than the electron density at the space charge region. Under this condition the surface behaves as a p-type, and an inversion layer is formed (Figure 1.4d). On the other hand, if a negative potential is applied to the electrode, a situation where the Fermi level of the electrode lies at the same energy of the solution will be eventually reached. At such potentials, there is no net charge transfer and there is no band bending. The potential at which such a condition is reached is named flat-band potential (Figure 1.4b). When the potential is made even more negative than the flat-band potential, the electron density grows at the interface, the bands bend downward and an accumulation layer is formed (Figure 1.4a). In such a condition the surface becomes degenerate and the semiconductor approaches metallic behavior. Similar behavior is observed with a p-type semiconductor-solution junction. In this case accumulation layer is observed when the electrode is made

General Introduction

more positive than the solution, while depletion and inversion layers form when the electrode is made more negative than the solution. The charge transfer abilities of a semiconductor electrode depend on the density of the majority carriers in the interface. If there is an accumulation layer, the behavior of a semiconductor electrode is similar to that of a metallic electrode, since there is an excess of the majority carriers available for charge transfer. In contrast, if there is a depletion or an inversion layer, then there are few charge carriers available for charge transfer, and electron transfer is negligible.

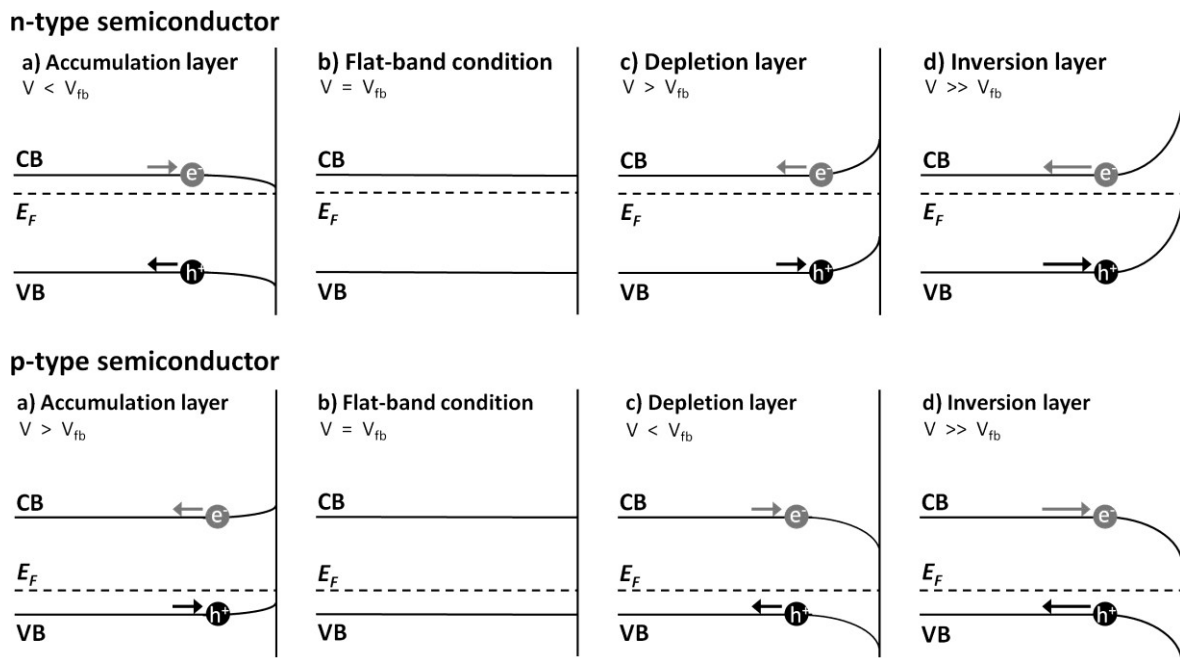


Figure 1.4. Effect of the varying potential at a semiconductor-solution junction. Both n-type and p-type semiconductors are taken into consideration. a) Accumulation layer, b) flat-band condition, c) depletion layer and d) inversion layer.

However, if an n-type semiconductor electrode is exposed to radiations with sufficient energy ($h\nu > E_g$), electrons can be promoted to the conduction band. These photogenerated carriers perturb the electrons and holes concentration in the semiconductor. The system will tend to relax to equilibrium by recombining electrons with holes (producing heat) or by rearranging the charge distribution at the interface. In fact, if a depletion layer existed in the junction in the dark, the photogenerated electrons will move away from the junction toward the bulk, while holes will move towards the interface. The holes arriving at the interface are characterized by a quasi Fermi level, E_{Fp}^* . Quasi-Fermi level represent the energy levels of electrons and holes, in a semiconductor under illumination. But since in n-type semiconductor $n \gg p$, the perturbation in holes

General Introduction

concentration is much greater than in electrons concentration, for this reason the electron density is not altered noticeably and the quasi-Fermi level for electrons, E_{Fn}^* , approaches the Fermi level E_F , the quasi-Fermi level of holes, instead, approaches the VB upper edge. If E_{Fp}^* is more positive than the redox potential of a couple Red/Ox^+ , then an electrochemical reaction occurs:



The electrons, instead, move inside the semiconductor to the outer circuit and finally to a metal counter electrode where they may react with an electroactive species Red'/Ox' with a redox potential below E_F , so that:



In Figure 1.5, a schematic representation of the operation mechanism of a photoelectrochemical cell is reported. The same representation may be given for a p-type semiconductor. In this case the electric field in the space charge region promotes the electrons migration towards the interface while the holes migrate towards the counter electrode.

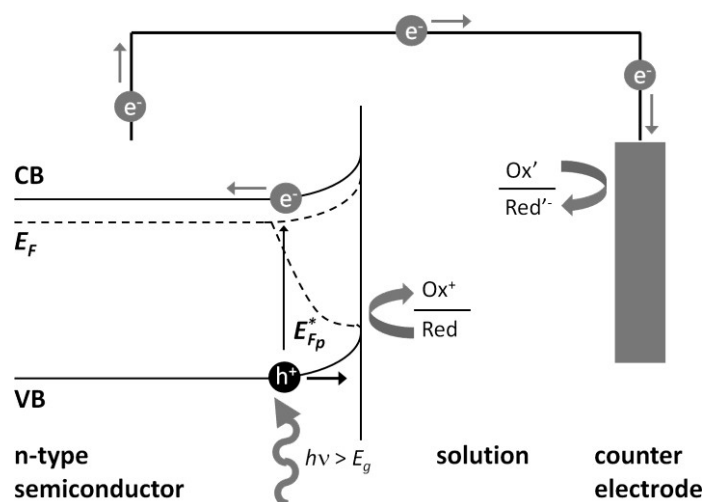


Figure 1.5. Schematic representation of a photoelectrochemical cell based on an n-type semiconductor electrode [e.g., n-SrTiO₃ / H₂O / Pt (H₂O → H₂ + ½ O₂)] [16].

General Introduction

Diagrams as the one reported in Figure 1.6 are used to represent the relative locations of the semiconductor bands edges and the redox potentials of electroactive species, E_{redox} . Note that reduction by an electron in the CB can take place when E_{redox} lies below the CB lower edge; oxidation by holes in the VB can take place when E_{redox} lies above the upper edge of the VB.

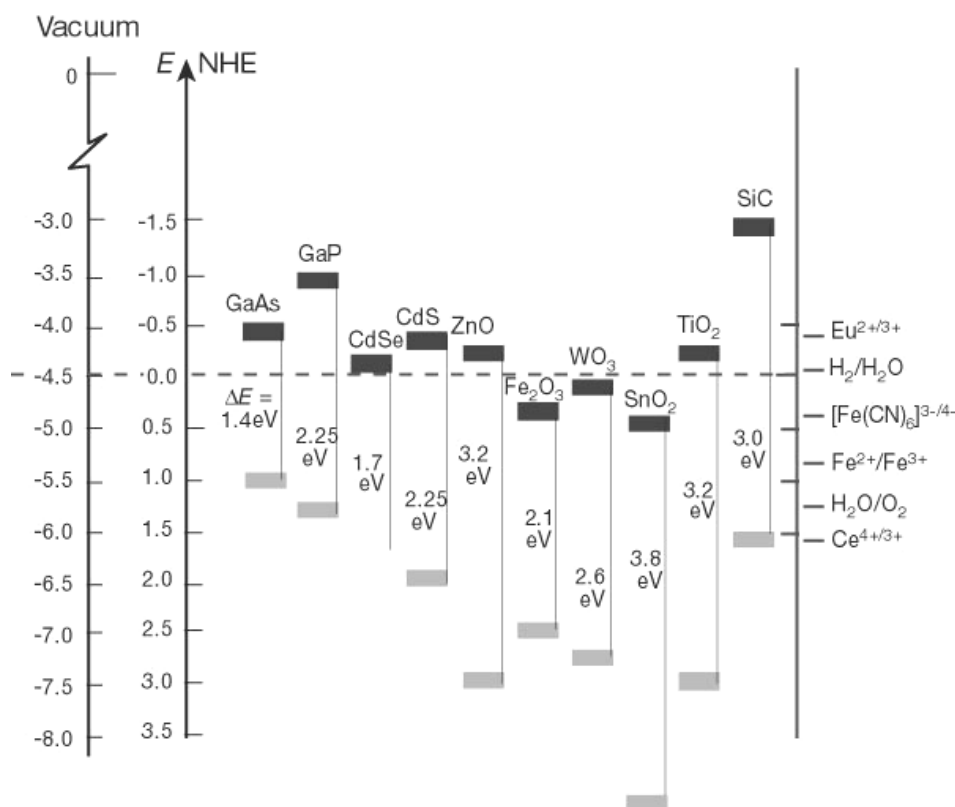


Figure 1.6. Band-edge positions of semiconductors with respect to several redox couples in aqueous solution at pH 1. Band positions are given both versus normal hydrogen electrode and versus electron in vacuum [3].

Another consideration to take into account is the stability of the semiconductor under light irradiation. In fact, in n-type semiconductors, the holes photogenerated at the interface, besides oxidizing a redox species in the solution, may undergo oxidation of the semiconductor. For example in n-type TiO_2 the following reaction can occur under illumination [17]:



General Introduction

For all these reasons, the design of a photoelectrochemical system goes through an accurate choice of the proper semiconductor, redox couples, solvent and counter electrode. An example is the application of n-Si photoanode for the synthesis of chlorine [18]. In aqueous solution under irradiation Si tends to be unstable and corrosion occurs following the reported reaction:



A passivating SiO_2 layer would readily form on the surface of the electrode, preventing any further electrochemical reaction. By protecting the surface of the electrode with a thin layer of iridium silicide, the electrode is stabilized and photoelectrochemical oxidation of Cl^- reaction is observed for several hours. Furthermore, using a very concentrated solution, i.e. 11 M LiCl, the hole capture efficiency of Cl^- is increased, limiting the silicon oxidation. The application of such a photoelectrosynthetic system, allows to obtain the chlorine evolution at a photopotential which is about 0.4 V less positive than the standard potential of the reaction. A number of other photoelectrochemical systems, for the oxidation or reduction of species of interest have been reported [16, 19, 20].

Another important application of semiconductor metal oxide electrodes is in the DSSC [13] (see paragraph 1.1.1). The semiconductor electrode is generally constituted by thin layer of TiO_2 nanoparticles casted on a transparent electrode. A sensitizing dye is either adsorbed or covalently attached to the surface of the nanoparticles. The counter electrode is generally a transparent platinized electrode while the electrochemical contact among the electrodes is granted by an I_3^-/I^- solution. In these cells, dyes are adsorbed to the semiconductor surface to sensitize the electrons to visible light and produce photocurrents with photons with smaller energy than the band-gap of the semiconductor. The schematic representation of the operation mechanism of a DSSC is shown in Figure 1.7. Absorption of light occurs in the dye adsorbed on the surface of the semiconductor (1). The photoexcited electron in the dye (D^*) is injected in the conduction band of the semiconductor (2). Since $\Delta E_{(\text{D}/\text{D}^*)} < E_g$, lower energy photons (i.e. visible light) are needed in order to generate photoexcited electrons. The space charge region of the semiconductor generate an electric field which prevents the photogenerated electrons from recombining with the oxidized dye. The electrons eventually reach the outer circuit, where they are transported to the load and subsequently to the counter electrode (3). The redox species

present in the contacting solution, shuttles the electron from the counter electrode to the photoanode where the oxidized dye (D^+) is reduced and regenerated (4).

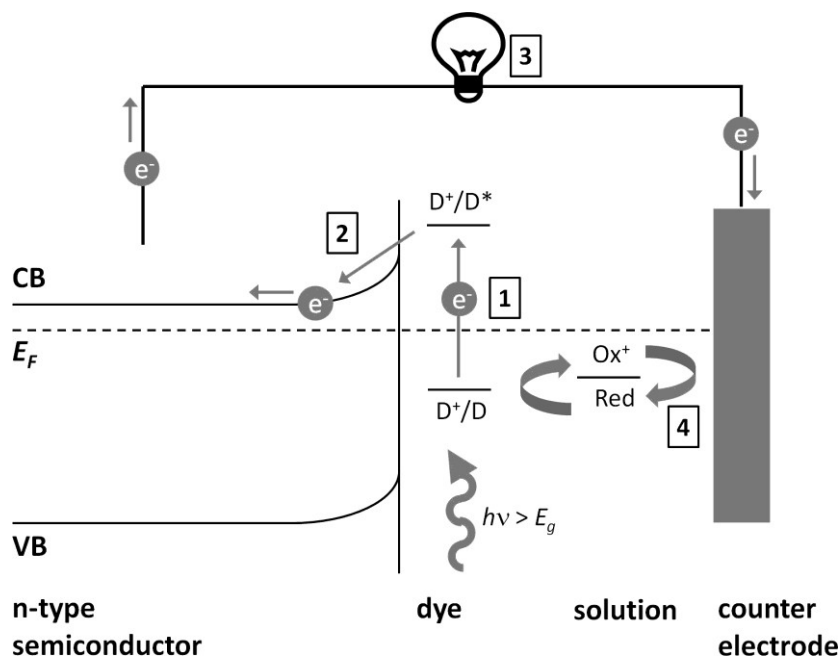


Figure 1.7. Functioning mechanism of a DSSC.

1.2.4 Photoelectrochemical water splitting

One of the most important field of application of photoelectrochemical cells (PECs) is by far the photoelectrochemical water splitting for the production of hydrogen from water. Hydrogen is considered an environmentally friendly fuel since the product of hydrogen combustion is water, which neither results in air pollution nor leads to the emission of greenhouse gases. This consideration is correct, assuming that hydrogen is generated using a source of renewable energy, such as solar, wind, hydroelectric, or hydrothermal energy. To date, photoelectrochemical water decomposition using solar energy is considered the most promising [21-25]. Since the first reports of this method published by Honda et al. [21] almost 30 years ago, there have been many papers published on different structures and materials to be applied on PECs. In simple terms, photoelectrochemical water decomposition is based on the conversion of light energy into electrical energy for the electrochemical decomposition of water. The most common arrangement of water splitting PEC is a photo-anode made of n-type semiconductor and cathode made of metal. In this arrangement a platinum cathode is usually used due to its

General Introduction

catalytic properties towards the hydrogen reduction, decreasing the energetic barrier for this reaction. As explained in the previous paragraph, light promotes electrons of the semiconductor over the band gap, leading to the formation of electron-holes pairs which can undergo electrochemical reactions. Gaseous oxygen evolves at the photoanode and the hydrogen ions migrate to the cathode. Simultaneously, the photogenerated electrons are transferred over the external circuit to the cathode, resulting in the reduction of hydrogen ions into gaseous hydrogen:



Accordingly, the overall reaction of the PEC may be expressed in the form:



The most studied material for the photo-anode is TiO_2 [21-25]. Despite TiO_2 has a high band gap, which makes its light harvesting capabilities limited to UV light, it is the favored material owing to its high corrosion resistance. Moreover, the electrochemical potentials of reactions (1.10) and (1.11) are located between TiO_2 VB and CB edges (see Figure 1.6), which, from an energetic view point, is essential to achieve a thermodynamically spontaneous process. Nonetheless, without an applied bias, poor photocurrent or gaseous product is obtained [26]. This shows that electron-hole recombination is a primary factor limiting PEC efficiency. The application of a positive bias, helped the separation of the photogenerated charges and greatly increased hole lifetimes [26, 27]. Consequently, at present, the application of this material as a photoelectrode requires a bias in order to decompose water to a significative extent. Such an external bias can be considered as environmentally friendly only when provided by a source of renewable energy, such as a photovoltaic unit. A bias also may be imposed through the use of electrolytes of two different pH values over the anode and cathode, so producing a chemical bias. This arrangement requires the use of an ionic bridge (e.g., agar) dividing the two electrolytes. Unfortunately, the photo-current flowing between the electrodes lead to the consumption of OH^- and H^+ ions at the anodic and cathodic cell compartments, respectively.

Consequently, this results in the neutralization of the electrolyte and to a reduction of the bias.

To date, the technologies for hydrogen generation using renewable energy are at the incubation stage. In any case, the energy conversion efficiency of water photoelectrolysis is principally determined by the properties of the materials used for the photoelectrodes. Consequently, commercial applications for hydrogen generation from solar energy and water will be determined by the progress in materials science and engineering applied to the candidate materials for photoelectrodes. Improving spatial separation between charge carriers to maintain a larger fraction of long-lived holes can be achieved by several strategies, such as controlling the size and morphology of the semiconductor structures.

1.3 Semiconductor Nanostructured Materials

The application of nanostructured semiconductor materials, with tailored dimensions and morphology may lead to great advantages in the development of more efficient energy conversion and storage devices. Many types of nanostructures have been applied to various energy conversion enhancement strategies. One of the most promising being quasi-1D structures, e.g. nanowires (NWs), nanofibers (NFs), nanotubes, nanorods. Quasi-1D structures have been extensively studied in the last decades since the early work on whisker growth performed by Wagner and Ellis [28]. In the 1970s and 1980s there was much work performed on synthesis of various whisker materials [29]. In the 1990s pioneering research performed by Haraguchi et al. on InAs/GaAs-based nanowires culminated in the demonstration of a light emitting diode (LED) based on an array of such structures [30]. More recently, nanotubes and nanorods of semiconductor materials such as: GaN [31], TiO₂ [32], ZnO [33] etc., have been reported.

All these elongated nanostructures can be synthesized by many methods, including: laser ablation [34], chemical vapor deposition [28], chemical synthesis [35], electrochemical deposition [36], template deposition [37].

The quasi-1D morphology, of nanorods and nanowires, is responsible for their unique properties, which are different from the bulk material. In fact, the larger surface/volume ratio in the fibers allows to extent the space charge region, which is built on the semiconductor electrolyte interface and is responsible for the electron hole separation process (see paragraph 1.2). Moreover such morphology allows a direct path for the transport of charges through the nanowires, minimizing their permanence in the

semiconductor and as a consequence increasing the lifetime of the carriers [38] (Figure 1.8b). On the contrary, in nanoparticles layers, the electron transport is described as a tortuous migration through the film, greatly increasing the permanence of the charges in the semiconductor material (Figure 1.8a). Such advantages are particularly interesting for a number of applications. These include: electronics [39], biological and chemical sensors [40], light emitting diodes [30], laser and numerous others. The energy applications of semiconductor nanowires are mainly focused on the development of energy storage devices, photoelectrochemical cells [41-43] and new generation solar cells [13]. For the latter, the earliest demonstration was from Alivisatos and co-workers, in which CdSe nanorods were used as the conducting layer of polymer-matrix solar cell [44]. The application of nanowires lead to an enhancement in the performance compared to solar cells employing nanostructures with aspect ratios approaching 1. Similar structures have been applied as photoanode for DSSC using smooth [38] and dendritic [45] ZnO nanowires. For example, Yang and coworkers [38] have shown a two-fold increase in the short circuit current density compared to a nanocrystalline TiO₂-based DSSC, with a maximum power conversion efficiency under AM 1.5¹ of about 1.5%.

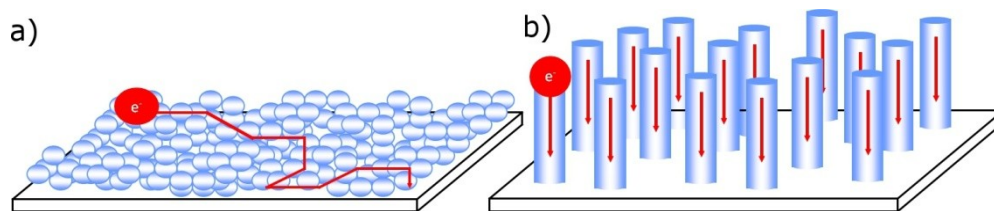


Figure 1.8. Figured representation of the electron path through a metal oxide nanoparticles film (a) and a metal oxide nanowires film (b).

As far as photoelectrosynthetic cells are concerned, the water splitting reaction is by far the most studied. In the literature, a number of examples of elongated nanostructures applied to the H₂ synthesis may be found. For example, Grimes and coworkers [46] prepared WO₃ NWs, by a solvothermal method, showing improvement in the efficiency of the photoelectrochemical water splitting, by increasing their aspect ratio. Khan et al. prepared, studied and compared the photoelectrochemical properties of TiO₂ thin films and

¹ The **air mass coefficient (AM)** defines the direct optical path length through the Earth's atmosphere and helps to characterize the solar spectrum after solar radiation has traveled through the atmosphere. The air mass coefficient is commonly used to characterize the performance of solar cells under standardized conditions. AM 1.5 is almost universal when characterizing terrestrial power-generating panels and corresponds to a solar-zenith angle of 48.2°.

NWs. The authors reported that the NWs exhibited a higher efficiency than the thin films [47].

In the course of this research different techniques, for the preparation and functionalization of metal oxide nanowires and nanorods, were taken into consideration, one of the most used being the template deposition. For this reason, this technique will be describe in detail in the next paragraph.

1.4 Methods to Obtain 1-D Nanostructures

Metal oxide 1-D nanostructures are commonly synthesized by gas phase approaches such as chemical vapor deposition [48, 49] thermal evaporation [50] and pulsed laser deposition [51]. These methods can produce high-quality, single crystalline wires with lengths of several microns. However, these processes require elevated temperatures of 450-900 °C and often face other limitations in terms of sample uniformity, substrate choice, and low product yield. In contrast, solution growth approaches are appealing because of the low growth temperatures (<350 °C), potential for scaling up, and straightforward methods of producing high-density arrays (nanowire number density $>10^{10}$ cm⁻²) [52]. Different solution growth approaches have been proposed in the last decade. These methods can be divided into two main categories which are templated deposition and directional nucleation growth.

1.4.1 Directional nucleation growth

One dimensional growth of metal oxides can be obtained by hydrothermal synthesis. In this procedure the nucleation of the final material is induced by tailoring the reaction conditions such as temperature, pH and concentration. If the nucleation rates on the crystal planes of the growing nuclei are significantly different, anisotropic particles can be obtained. When such growth mechanism is predominant on one direction, 1-D structures can be obtained. The crystal morphology can be controlled by various species in the solution, which act as promoters or inhibitors for nucleation and growth. These species can include anions, additives such as amines, and acids and bases. This mechanism is well exemplified by ZnO, for which this approach is widely used for the preparation of NFs. In aqueous solution, zinc cations are solvated by water, giving rise to aquo ions. In dilute

General Introduction

solutions, zinc(II) can exist as several monomeric hydroxyl species [53]; these species include $\text{ZnOH}^+_{(\text{aq})}$, $\text{Zn}(\text{OH})_{2(\text{aq})}$, $\text{Zn}(\text{OH})_{2(\text{s})}$, $\text{Zn}(\text{OH})_{3}^-_{(\text{aq})}$ and $\text{Zn}(\text{OH})_{4}^{2-}_{(\text{aq})}$. At a given zinc(II) concentration, the stability of these complexes is dependent on the pH and temperature of the solution [54]. Solid ZnO nuclei are formed by the dehydration of these hydroxyl species. The ZnO crystal can continue to grow by the condensation of the surface hydroxyl groups with the zinc-hydroxyl complexes [54]. The hydrolysis and condensation reactions of zinc salts result in one-dimensional ZnO crystals under a wide variety of conditions. Alkaline conditions are crucial because divalent metal ions do not readily hydrolyze in acidic media [55]. For growth at $\text{pH} < 9$, an additive such as hexamethylenetetramine (HMTA) or dimethylamineborane (DMBA) must be used to promote one-dimensional ZnO precipitation. It has been suggested [54] that these additives function, in part, by decomposing during the reaction, increasing the pH to above 9, and adsorbing preferentially on specific crystalline surfaces, hindering the nucleation of metalhydroxi ions. As an alternative, the pH of the solution can be increased exploiting an electrochemical reaction such as H_2O_2 reduction. In this case, the increase in the OH^- concentration is localized at the surface of the working electrode and metal oxide nanorods are likely to grow on its surface [56], the reaction mechanism will be explained in more detail in chapter 3.1. In Figure 1.9 a representation of the, HMTA assisted, electrochemical growth is reported. Besides ZnO, hydrothermal growth has been applied for the preparation of nanowires of TiO_2 -rutile [57, 58], MgO [59], $\alpha\text{-Fe}_2\text{O}_3$ [60], CdS [61] and V_2O_5 [62].

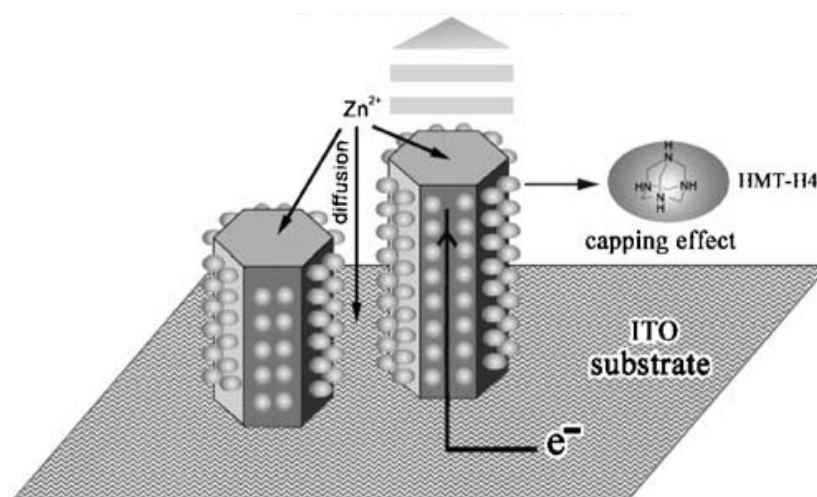


Figure 1.9. Electrochemical growth model via HMTA assisted deposition [63].

1.4.2 Template synthesis

Template synthesis is a relatively simple and easy procedure which has made the fabrication of rather sophisticated nanomaterials accessible to almost any laboratory. The method is based on the simple but effective idea that the pores of a host material can be used as a template to direct the growth of new materials. Historically template synthesis was introduced by Possin [64] and refined by Williams and Giordano [65], who prepared different metallic nanowires with widths as small as 10 nm within the pores of etched nuclear damaged tracks in mica. It was further developed by Charles Martin's group [66-68] and followed by others [69] with a number of examples and applications [70]. Afterwards, various examples of membrane templated electrochemical deposition of nanowires of semiconductors [71], metals (e.g. Ni and Co) [72], oxides [73] and conducting polymers [70] appeared in the literature.

The nanoporous membranes usually employed as templates are alumina or track-etched polymeric membranes which are widely used as ultrafiltration membranes. Track etched membranes are flexible with a smooth surface while alumina films are brittle and rather rough. Another difference is the pore density which is typically 10^9 pores cm^{-2} for track-etched membranes compared to 10^{11} pores cm^{-2} for alumina membranes. Alumina membranes are therefore interesting as templates for producing high-density nanomaterials. Track etched membranes are more suitable for obtaining low density nanomaterials, for example in the fabrication of nanoelectrode ensembles where low nanoelectrode densities are often desired. As shown in Figure 1.10, a problem with track-etched membranes is the fact that the pores are not always parallel to each other, their shape is not always cylindrical and pore positions are randomly distributed unless special procedures are applied [74].

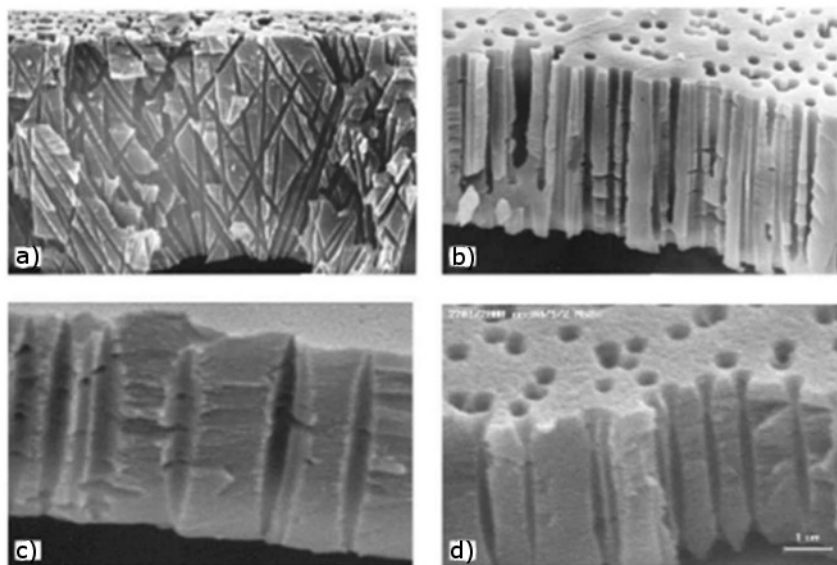


Figure 1.10. Porous structures obtained in polymeric films using different methods of irradiation and etching conditions: a) polycarbonate membrane with cylindrical, non-parallel pores; b) polypropylene with slightly conical parallel pores; c) polyethylene terephthalate with cigar shaped pores; d) polyethylene terephthalate with bow-tie pores [75].

1.4.2.1 Electrochemical deposition

The electrochemical deposition inside the pores of a nanoporous membrane requires that one side of the membrane be made conductive. This can be done by plasma or vacuum deposition of a thin layer of metal (typically, 100 - 200 nm) on one side of the membrane. The membrane should be robust enough to tolerate this kind of treatment, for this reason alumina membranes are more indicated. Since the process is based on the progressive growth and filling of the pores from the bottom metallic layer toward the open end of the pores, final products are nanowires and not hollow structures (e.g. nanotubes).

The template electrodeposition has been mostly studied to obtain metal nanowires, but also other materials, such as, for instance, alloys (NiFe [76], FeSiB [77]) salts (Bi_2Te_3 [78], CdS [71]) and metal oxides (TiO_2 [79], RuO_2 [80]). As far as metal oxides are concerned, the deposition mechanism can exploit an electrochemical reaction to change the pH at the surface of the electrode and induce the metal oxide precipitation (see paragraph 1.4.1), or, as an alternative, oxidize the metal cation to a redox state, which is more prone to react with water and precipitate as metal oxide/hydroxide. For example, RuO_2 nanowires were prepared by template-assisted anodic deposition on an alumina membrane, from an

aqueous solution of 10 mM RuCl₃ [80]. Crystalline RuO₂ nanotube arrays were readily obtained by annealing at elevated temperatures.

1.4.2.2 Template filling techniques

The direct template filling from a liquid precursor is the most straightforward and versatile method for preparing NW arrays. The drawback of this approach is the difficulty to ensure complete filling of the template pores. A number of methods have been developed in order to force metal oxide precursors inside the pores, the most diffused being: electrophoresis [81, 82], centrifugation [83], solvent evaporation [84], capillary forces [37].

Martin et al. [37] have studied the formation of various oxide nanorods and nanotubules filling, by capillary force, the templates with colloidal dispersions. Colloidal dispersions were prepared using appropriate sol-gel processing techniques. The template was placed in a the sol for a defined period of time. The capillary force drives the sol into the pores if the sol has good wettability for the template. After the pores were filled with sol, the template was withdrawn from the sol and dried. The template was chemically etched and the fibers calcined at elevated temperatures to densify the sol-gel derived nanorods.

1.5 Goal of the Thesis

The goal of this thesis is the development of techniques for the synthesis of nanostructured metal oxide ceramic materials to be used as photoelectrodes in energy conversion devices. In chapter 2 a new sol-gel template synthesis for the production of TiO₂ nanowires will be presented. This procedure is based on the approach developed by Martin [37], but several modification has been introduced in order to make this procedure more robust and reproducible. Furthermore, the obtained material was tested as electrode in a photoelectrochemical reaction of interest in energetic field. In chapter 3, the concept of quasi-1D structure will be further developed in the synthesis of hierarchical structures, exploiting a synthetic method which overcomes the limits encountered in the former synthetic procedure. Finally in chapter 4 will be presented a promising technique for the functionalization of micro and nanoobjects. The goal being the production of metal oxide

General Introduction

micro and nanowires to be used in self sustaining energetic devices like micro-electromechanical systems (MEMS) [85] and nanosensors.

References

- [1] M. Pehnt, D. Jessing, P. Otter, R. Vogt, G. Reinhardt, W. Krewitt, M. Nast, J. Nitsch, F. Trieb, *Renewable Energies – Innovations for a Sustainable Energy Future*, Federal Ministry for the Environment, Nature Conservation and Nuclear Safety, Germany, (2009)
- [2] BP Statistical Review of World Energy (2011), International Energy Agency, Key World Energy Statistics (2012)
- [3] M. Graetzel, *Nature* **414** (2001) 338
- [4] K. Rjeshwar, *J. Appl. Electrochem.* **25** (1995) 1067
- [5] R. C. Alkire, D. M. Kolb, J. Lipkowski, P. N. Ross, *Advances in Electrochemical Science and Engineering* (2010) Wiley-VCH, Weinheim
- [6] B. A. Parkinson, A. Heller, B. Miller, *Appl. Phys. Lett.* **33** (1978) 521
- [7] L. Fornarini, B. Scrosati, *Electrochim. Acta* **28** (1983) 667
- [8] D. Cahen, G. Hodes, M. Graetzel, J. F. Guillemoles, I. Reiss, *J. Phys. Chem.* **104** (2000) 2053
- [9] T. Inoue, A. Fujishima, S. Konishi, K. Honda, *Nature* **277** (1979) 1035
- [10] O. Khaselev, J. O. Turner, *Science* **280** (1998) 425
- [11] H. Tributsch, *Catal. Today* **39** (1997) 177
- [12] V. M. Aroutiounian, V. M. Arakelyan, G. E. Shahnazaryan, *Sol. Energy* **78** (2005) 581
- [13] B. O'Regan, M. Graetzel, *Nature* **353** (1991) 737
- [14] A. Yella, H. W. Lee, H. N. Tsao, C. Yi, A. K. Chandiran, M. K. Nazeeruddin, E. W.-D. Diao, C.-Y. Yeh, S. M. Zakeeruddin, M. Graetzel, *Science* **6056** (2011) 629
- [15] C.-Y. Wang, M. Wang, J.-Y. Li, N. Pootrakulchote, L. Alibabaei, C. Ngoc-le, J. D. Decoppet, J.-H. Tsai, C. Graetzel, C.-G. Wu, S. M. Zakeeruddin, M. Graetzel, *ACS Nano* **3** (2009) 3103
- [16] A. J. Bard, L. R. Faulkner, *Electrochemical Methods* (1980) Wiley, New York
- [17] V. K. Mahajan, S. K. Mohapatra, M. Misra, *Int. J. Hydrogen Energ.* **33** (2008) 5369
- [18] F.-R. Fan, R. G. Keil, A. J. Bard, *J. Am. Chem. Soc.* **105** (1983) 220
- [19] K. J. McDonald, K.-S. Choi, *Chem. Mater.* **23** (2011) 4863
- [20] T. Arai, S. Sato, K. Uemura, T. Morikawa, T. Kajino, T. Motohiro, *Chem. Commun.* **46** (2010) 6944
- [21] A. Fujishima, K. Honda, *Nature* **238** (1972) 37

- [22] H. Yoneyama, H. Sakamoto, H. Tamura, *Electrochim. Acta* **20** (1975) 341
- [23] Y. Liu, A. Hagfeldt, X. R. Xiao, S. E. Lindquist, *Sol. Energy Mater. Sol. Cells* **55** (1998) 267
- [24] R. N. Pandey, M. Misra, O. N. Srivastava, *Int. J. Hydrogen Energ.* **23** (1998) 861
- [25] V. Aranyos, H. Grennberg, S. Tingry, S. E. Lindquist, A. Hagfeldt, *Sol. Energy Mater. Sol. C.* **64** (2000) 97
- [26] A. J. Cowan, J. Tang, W. Leng, J. R. Durrant, D. R. Klug, *J. Phys. Chem. C* **114** (2010) 4208
- [27] A. J. Cowan, C. J. Barnett, S. R. Pendlebury, M. Barroso, K. Sivula, M. Graetzel, J. R. Durrant, D. R. Klug, *J. Am. Chem. Soc.* **133** (2011) 10134
- [28] R. S. Wagner, W. C. Ellis, *Appl. Phys. Lett.* **4** (1964) 89
- [29] E. I. Givargizov, in: E. Kaldis (Eds.) *Current Topics in Material Science* (1978) North-Holland, Amsterdam
- [30] K. Haraguchi, T. Katsuyama, K. Hiruma, K. Ogawa, *Appl. Phys. Lett.* **60** (1992) 745
- [31] J. Goldberger, R. He, Y. Zhang, S. Lee, H. Yan, H.-J. Choi, P. Yang, *Nature* **422** (2003) 599
- [32] T. Kasuga, M. Hiramatsu, A. Hoson, T. Sekino, K. Niihara, *Adv. Mater.* **11** (1999) 1307
- [33] I. Mora-Sero, F. Fabregat-Santiago, B. Denier, J. Bisquert, R. Tena-Zaera, J. Elias, C. Levy-Clement, *Appl. Phys Lett.* **89** (2006) 203117
- [34] A. M. Morales, C. M. Lieber, *Science* **279** (1998) 208
- [35] J. Wang, S. He, S. Zhang, Z. Li, P. Yang, X. Jing, M. Zhang, Z. Jiang, *Mat. Sci. Pol.* **27** (2009) 477
- [36] M. E. Toimil Molaes, V. Buschmann, D. Dobrev, R. Neumann, R. Scholz, I. U. Schuchert, J. Vetter, *Adv. Mater.* **13** (2001) 62
- [37] B. B. Lakshmi, C. J. Patrissi, C. R. Martin, *Chem. Mater.* **9** (1997) 2544
- [38] M. Law, L. E. Greene, J. C. Johnson, R. Saykally, P. Yang, *Nat. Mater.* **4** (2005) 455
- [39] D.-S. Han, Y.-K. Moon, S. Lee, K.-T. Kim, D.-Y. Moon, S.-H. Lee, W. S. Kim, J.-W. Park, *J. Electron. Mat.* **41** (2012) 2380
- [40] Z. Zhao, W. Lei, X. Zhang, B. Wang, H. Jiang, *Sensors* **10** (2010) 1216
- [41] Y.-J. Hwang, C. Hahn, P. Yang, *ACS Nano* **6** (2012) 5060
- [42] Y. Li, J. Z. Zhang, *Laser Photonics Rev.* **4** (2010) 517
- [43] M. Frites, Y. A. Shaban, S. U. M. Kahn, *Int. J. Hydrog. Energ.* **35** (2010) 4944
- [44] W. U. Huynh, J. J. Dittmer, A. P. Alivisatos, *Science* **295** (2002) 2425

- [45] J. B. Baxter, E. S. Aydil, *Appl. Phys. Lett.* **86** (2005) 053114
- [46] J. Su, X. Feng, J. D. Sloppy, L. Guo, C. A. Grimes, *Nano Lett.* **11** (2011) 203
- [47] S. U. M. Kahn, T. Sultana, *Sol. Energ. Mat. Sol. C.* **76** (2003) 211
- [48] W. I. Park, G. C. Yi, M. Y. Kim, S. J. Pennycook, *Adv. Mater.* **14** (2002) 1841
- [49] J. J. Wu, S. C. Liu, *Adv. Mater.* **14** (2002) 215
- [50] J. Y. Lao, J. Y. Huang, D. Z. Wang, Z. F. Ren, *J. Mater. Chem.* **14** (2004) 770
- [51] Y. Sun, G. M. Fuge, M. N. R. Ashfold, *Chem. Phys. Lett.* **396** (2004) 21
- [52] E. L. Greene, D. Y. Benjamin, M. Law, D. Zitoun, P. Yang, *Inorg. Chem.* **45** (2006) 7535
- [53] K. Govender, D. S. Boyle, P. B. Kenway, P. O'Brien, *J. Mater. Chem.* **14** (2004) 2575
- [54] S. Yamabi, H. Imai, *J. Mater. Chem.* **12** (2002) 3773
- [55] M. A. Verges, A. Mifsud, C. J. Serna, *J. Chem. Soc. Faraday T.* **86** (1990) 959
- [56] S. Peulon, D. Lincot, *Adv. Mater.* **8** (1996) 166
- [57] Y. J. Hwang, C. Hahn, B. Liu, P. Yang, *ACS Nano* **6** (2012) 5060
- [58] B. Liu, J. E. Boercker, E. S. Aydil, *Nanotechnology* **19** (2008) 505604
- [59] A. A. Al-Ghamdi, F. Al-Hazmi, F. Alnowaiser, R. M. Al-Tuwirqi, A. A. Al-Ghamdi, O. A. Alhartomy, F. El-Tantawy, F. Yakuphanoglu, *J. Electroceram.* **29** (2012) 198
- [60] C. C. Lucas, C. C. Ferraz, W. M. Carvalho, D. Criado, F. L. Souza, *ACS Appl. Mater. Interfaces* **4** (2012) 5515
- [61] R. Varadharajan, S. Durai, *Int J. Mat. Res.* **103** (2012) 358
- [62] K. Takahashi, S. J. Limmer, Y. Wang, G. Z. Cao, *Jpn J. Appl. Phys.* **44** (2005) 662
- [63] F. Xu, Y. Lu, Y. Xie, Y. Liu, *J. Solid State Electr.* **14** (2010) 63
- [64] G. E. Possin, *Rev. Sci. Instrum.* **41** (1970) 772.
- [65] W. D. Williams, N. Giordano, *Rev. Sci. Instrum.* **55** (1984) 410
- [66] R. M. Penner, C. R. Martin, *Anal. Chem.* **59** (1987) 2625
- [67] J. F. Cheng, C. R. Martin, *Anal. Chem.* **60** (1988) 2163
- [68] V. P. Menon, C. R. Martin, *Anal. Chem.* **67** (1995) 1920
- [69] K. Uosaki, K. Okazaki, H. Kita, H. Takahashi, *Anal. Chem.* **62** (1990) 652
- [70] C. R. Martin, D. T. Mitchell, in: A. J. Bard, I. Rubinstein (Eds.) *Electroanalytical Chemistry, A Series of Advances* (1999) Marcel Dekker, New York
- [71] D. Routkevitch, T. Bigioni, M. Moskovits, J.-M. Xu, *J. Phys. Chem.* **100** (1996) 14037

- [72] C. Schoenberger, B. M. I. van der Zande, L. G. J. Fokkink, M. Henny, C. Schmid, M. Kruger, A. Bachtold, R. Huber, H. Birk, U. Staufer, *J. Phys. Chem. B* **101** (1997) 5497
- [73] M. Zheng, G. Li, X. Zhang, S. Huang, Y. Lei, L. Zhang, *Chem. Mater.* **13** (2001) 3859
- [74] L. D.-D. Pra, E. Ferain, R. Legras, S. Demoustier-Champagne, *Nucl. Instrum. Methods Phys. Res. B* **196** (2002) 81
- [75] P. Y. Apel, *Radiat. Meas.* **34** (2001) 559
- [76] H. Chiriac, A. E. Moga, M. Urse, T.-A. Ovari, *Sens. Actuators A* **106** (2003) 348
- [77] K. R. Pirota, D. Navas, M. Hernandez-Vélez, K. Nielsch, M. Vasquez, *J. Alloy Compd.* **369** (2004) 18
- [78] A. L. Prieto, M. S. Sander, M. S. M. Gonzalez, R. Gronsky, T. Sands, A. M. Stacy, *J. Am. Chem. Soc.* **123** (2001) 7160
- [79] Y. Lei, L. D. Zhang, J. C. Fan, *Chem. Phys. Lett.* **338** (2001) 231
- [80] C. C. Hu, K. H. Chang, M. C. Lin, Y. T. Wu, *Nano Lett.* **6** (2006) 2690
- [81] I. Zhitomirsky, *Adv. Colloid Interfac.* **97** (2002) 279
- [82] O. O. Van der Biest, L. J. Vandeperre, *Annu. Rev. Mater. Sci.* **29** (1999) 327
- [83] T. Wen, J. Zhang, T. P. Chou, S. J. Limmer, G. Z. Cao, *J. Sol–Gel Sci. Techn.* **33** (2005) 193
- [84] K. Takahashi, Y. Wang, K. H. Lee, G. Z. Cao, *Appl. Phys. A* **82** (2006) 27
- [85] J. Lueke, W. A. Moussa, *Sensors* **11** (2011) 1433

2. Template Synthesis and Characterization of TiO₂ Nanofibres

2.1 Introduction

TiO₂ is one of the most studied photoactive materials, finding application in a wide number of fields, the most important being: photocatalysis [1], biosensors [2], photoconversion [3], batteries [4], drug release [5] etc. This is mainly due to its important characteristics of low cost, low toxicity, excellent photoactivity and photochemical stability [6-9].

Titanium dioxide is a large band-gap material (3.2 eV) which is found in three main crystallographic phases:

- Rutile
- Anatase
- Brookite

These structures can be described using an octahedron as building block; the three crystalline forms differ among each other for the distortion and assembly of the various chains of octahedra. In anatase, the octahedra share vertices, in rutile they share edges, while are both shared in brookite (see Figure 2.1).

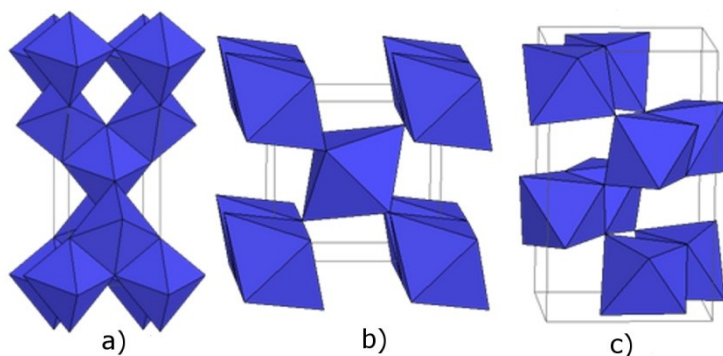


Figure 2.1. Crystallographic structures of anatase (a), rutile (b), brookite (c).

Thermodynamic calculations based on calorimetric data, show that rutile is the most stable phase at all temperatures and pressures up to 60 kbar [10], and is therefore the most favored structure. The small differences in terms of free energy (4-20 kJ mol⁻¹) between the three phases, suggest that the metastable polymorphs have stability comparable to that of rutile for values close to the room temperature and ambient pressure.

Anatase is commonly considered the most photoactive phase, this should be related to a slower charge recombination in this phase [8], still has to be taken into account that some authors argue that this process can be further slowed down in a TiO₂ in which a second crystalline phase is present in minority extent [11].

In the sol-gel process [12], the particles of a colloidal dispersion react together forming a continuous matrix filled with the solvent, which eventually, leads to a ceramic material. A colloid is a dispersion in which the dispersed phase is so small that the gravitational force is negligible and interparticle interactions control the system stability. When the particles of a colloidal system are dispersed in a liquid, the system is called sol. If the particles of a sol react and bind together forming larger particles or polymer matrices filled with the solvent, a gel is formed and eventually, if the solvent is removed by a thermal treatment, a ceramic material is obtained. A ceramic material is an inorganic non metallic material; therefore, metal oxides, nitrides and carbides, both crystalline and non crystalline, are included. Sol-gel is one the most used reactions used for the production of photoactive TiO₂.

In the sol-gel process, the precursors (the starting compounds) for the preparation of the sol are metal or metalloid elements surrounded by organic or inorganic ligands, which do not include another metal/metalloid atom. Alkoxides are the most diffused precursors in the sol-gel process, but inorganic salts are also used.

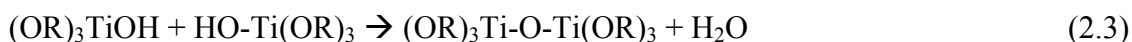
Metal alkoxides are popular precursors because they easily react with water by an hydrolysis reaction, which, for Ti precursors, may be described by the following scheme:



Depending on the amount of water, the presence of a catalyst and the reactivity of the precursor, the reaction can go to completion:



Two hydrolyzed, or partially hydrolyzed, molecules can react together in condensation reactions 2.3 and 2.4 respectively:



or



The condensation reaction continues giving large macro molecules and eventually polymers and goes on even after the gel is formed. In fact, gel segments are still free to move close enough to allow further condensation, moreover, non-reacted sol particles can still be present in the solution and bind to the polymeric network. Further condensation reactions lead to a gel shrinkage and expulsion of liquid from the pores of the gel. As long as the condensation goes on, the flexibility of the polymeric network is reduced and the rigidity of the gel is increased. Usually the gels produced by sol-gel process are amorphous even after complete drying of the material, therefore, a thermal treatment is often applied if a crystalline material is required. When the temperature of the thermal treatment is high enough, a pore-free ceramic is obtained.

The metal alkoxides from the transition metals, especially from group d0 (Ti, Zr), are widely used as starting material for metal oxide production. These metal alkoxide are more reactive with respect to the metalloids precursors, since their electronegativity is lower and for this reason are more prone to react with a nucleophilic molecules. Moreover transition metals exhibit several coordination states, so that coordination expansion spontaneously occurs upon reaction with water or other nucleophilic molecules. Such a reactivity requires a careful control of the reaction conditions in order to obtain homogeneous gels. Chemical modification of the transition metals precursors, with complexing molecules such as alcohols, chlorides, acids and chelating molecules, is often used to slow down the hydrolysis and condensation reactions and achieve a better control over the gelation process [13].

When the sol-gel reaction occurs inside the pores of a membrane (see paragraph 1.3), it is possible to obtain ceramic nanowires. However, both faces of the membrane, will be also covered with a thin layer of metal oxide. Such thin layer must be removed from one side of the membrane, before etching the templating material, so obtaining self standing NWs. A scheme of this process is shown in Figure 2.2.

Two different methods reported in literature, for the preparation of the TiO₂ NWs, were tested and optimized. At first the reaction rate was controlled by decreasing the reaction temperature [14], in the second method a chelating agent was added to the precursor mixture [15].

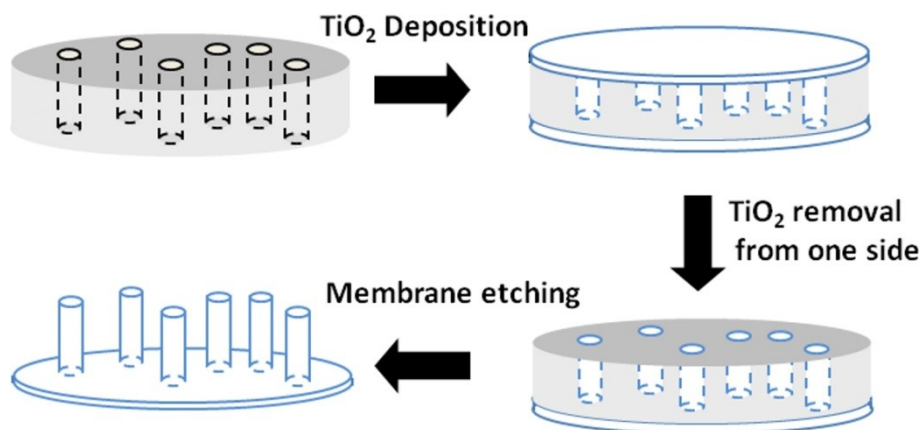


Figure 2.2. Schematic representation of the synthetic procedure of template TiO₂ nanofibers on alumina or polycarbonate membrane.

2.2 Experimental

Chemicals and materials

All the chemicals employed were of reagent grade quality. For the preparation of the titanium sol, titanium tetraisopropoxide (TTiP) 97% *Sigma-Aldrich*, ethanol (99.8%) *Carlo Erba*, HCl 0.1 N solution *Carlo Erba* and acetylacetone ($\geq 99\%$) *Sigma-Aldrich* were used. Alumina membranes were purchased from *Whatman International Ltd*, polycarbonate membranes were purchase from *Osmonic Inc*. In Table 2.1, the morphological parameters of the membranes used for the experiments are reported.

Membrane type	Pore diameter (nm)	Pore density (pores cm ⁻²)	Thickness (μm)
Alumina	200	10 ⁹	60
Polycarbonate	200	3*10 ⁸	10

Table 2.1. Morphological parameters of the membranes used for the experiments.

Low temperature gelation

TTiP (5 mL) was added to 20 mL of ethanol, the solution was subsequently stirred for 30 minutes in an ice bath. A second solution, containing 35 mL of ethanol, 1 mL of distilled water and 0.5 mL of 0.1 M HCl was slowly added drop by drop to the first solution obtaining a white

suspension. The molar composition of the final bath is TTiP 1 / H₂O 3.3 / EtOH 56 / HCl 0.003. When the solutions were completely mixed, an alumina membrane was immersed in the suspension for 90 seconds. The modified membrane was extracted from the reaction vessel, dried in air for 6 hours and in an oven at stationary regime at 100°C for 6 hours. Finally the membrane was calcined at 500°C with an air flux of 30 mL min⁻¹ for 3 hours.

The TiO₂ outer layer was subsequently removed from one side of the membrane using sandpaper and the template was dissolved in a 3 M NaOH solution.

Chemical modification of the titania precursor

In these experiments, 15 mL of titanium tetraisopropoxide were mixed to 30 ml of ethanol. In a different becker, 5.26 mL of acetylacetone (AcAc) and 2.72 mL of distilled water were mixed to 30 mL of ethanol. Then the first solution was slowly poured, drop by drop, on the second solution and stirred at room temperature for 2 hours. The molar composition of the final bath is TTiP 1 / H₂O 3 / AcAc 1 / EtOH 20. Both alumina and polycarbonate membranes were used as templating material. 20 mL of the dark yellow colored sol was pumped using a syringe through the membrane, which was placed inside a filter-holder (see Figure 2.3). The pumping procedure was repeated 8-10 times until the color of the suspension changed to light yellow, indicating that the suspension was impoverished in sol particles.

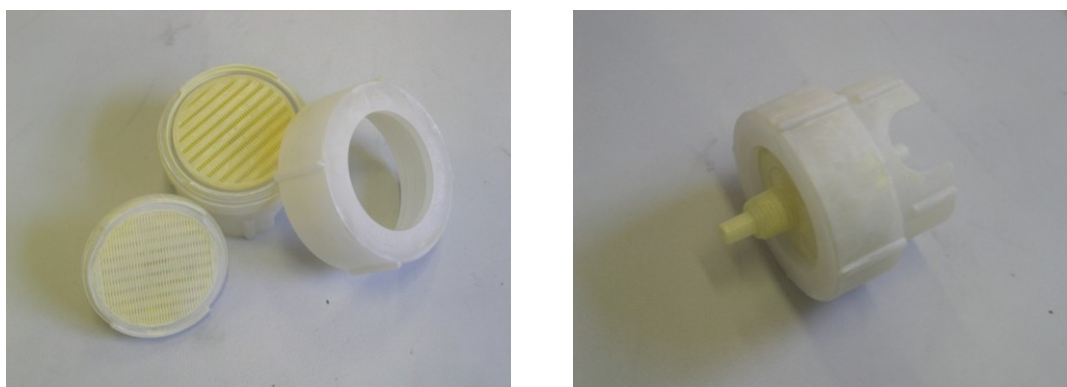


Figure 2.3. Membrane-holder used during the TiO₂ nanofibers synthesis by precursor modification process.

The membrane was subsequently immersed in the remaining 40 ml of suspension, which was previously taken to boiling temperature. After 20 minutes, the membrane was removed from the sol bath and dried in an oven at stationary regime for three hours at 100°C or at 200°C.

As far as alumina membranes are concerned, again the TiO₂ outer layer was removed from one side using sandpaper and the template was dissolved in a 3 M NaOH solution. In order to remove the polycarbonate membrane, chemical etching (in CH₂Cl₂ for 1 h), pyrolysis, or plasma etching were taken into consideration. Plasma etching was also applied to the TiO₂ outer layer removal from PC.

Finally the free standing TiO₂ nanofibers were calcined at 500°C for 3 hours with an air flux of 60 mL min⁻¹.

Plasma etching

The etching procedure on the polycarbonate TiO₂ modified membranes was performed by radio frequency plasma enhanced chemical vapor deposition (RF-PECVD) in a Plasma Electronics industrial apparatus with a vacuum chamber of 1 m³ of cubic shape (Plasma Electronic PORTA 900). Gas distribution from one side of the cube and pumping from the opposite side allows a uniform distribution of the process gases, the chamber walls serve as anodes in the discharge while the cathode consists in a plate electrode at the bottom side of the cube. The etching procedure was conducted using CF₄ and O₂ as feeding gases at the constant flow rate of 100 mL min⁻¹. The substrates were positioned on the cathode and the RF power was set at 700 W.

Morphological and crystallographic characterization

SEM analyses were performed with a JEOL JSM-5600LV, equipped with a Vega LVM TESCAN Energy-dispersive X-ray spectrometer (EDX). FT-Raman spectra were obtained at room temperature using a Thermo Fisher (Nicolet Almega XR) spectrometer equipped with an InGaAs detector. The Raman spectra were obtained with a DXR Raman Microscope (Thermo Scientific, MA, USA) equipped with an automatic stage for mapping capability and a 532 nm and 780 nm lasers with a maximum laser power at sample of 10 mW and 24 mW respectively. The spectra were recorded in the range 3500 – 50 cm⁻¹ using a full range grating with 900 lines mm⁻¹.

TiO₂ electrode fabrication

10 mg of TiO₂ NF were gently mixed in the mortar, using a pestle, with 1 drop of acetic acid solution, until obtaining a lump free homogeneous and dense suspension. In the meantime, an ITO electrode was cleaned by sonication for 30 minutes in isopropanol (iPrOH) and 30 minutes in

deionized water. A hole, 5 mm in diameter, was punched on a kapton adhesive tape strip which was attached on the conductive side of the ITO electrode and used as a mask (Figure 2.4a). The TiO₂ paste was casted over the masked ITO glass by doctor-blade technique (b). The paste was allowed to air dry for 1 hour (c), subsequently the mask was removed and the electrode was placed in an oven at 150°C for 1 hour in order to allow the TiO₂ paste sinterization on the ITO (d). Finally, the electrode was abundantly rinsed with deionized water in order to remove the poorly attached TiO₂ particles. A strip of copper conductive tape was used to create the electrical contact (e) and a strip of kapton tape with a circular hole is used to define the geometric area of the electrode, namely 0.07 cm² (f).

The same technique was applied for the preparation of an electrode using a commercial TiO₂ nanoparticles (Degussa p25), to be used as reference material.

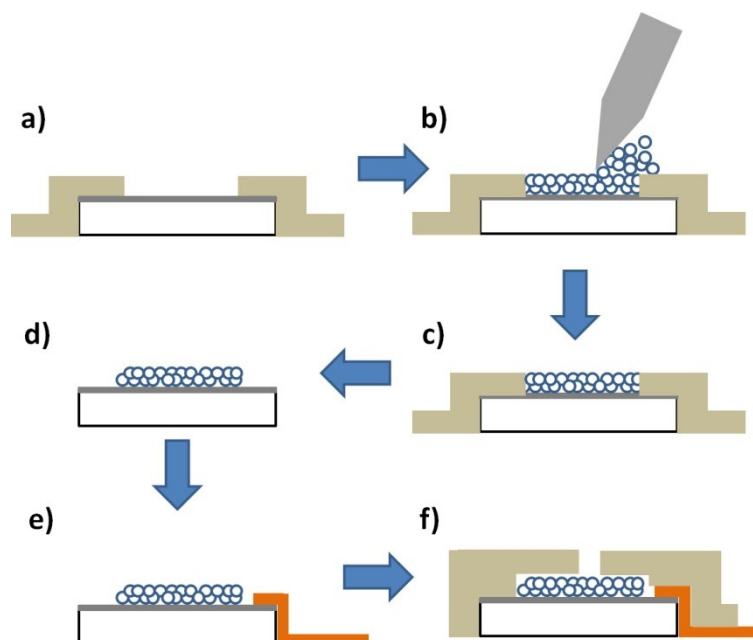


Figure 2.4. Schematic representation of TiO₂ NP electrode fabrication by doctor blade technique (not in scale). a strip of adhesive tape is placed on the ITO glass electrode (a), the TiO₂ paste is casted on the surface of the electrode by doctor blade technique (b). The paste is allowed to dry for 1 hour (c), then the mask is removed and the electrode place in an oven at 150°C for 1 hour (d). A strip of copper adhesive tape is used to make an electrical contact (e) and another strip of kapton tape is used to define the geometric area of the electrode (0.07 cm²) (f).

Photoelectrochemical water oxidation experiments

Commercial TiO₂ nanopowder (Degussa p25) electrode and templated TiO₂ nanofiber electrode were both tested for the photoelectrochemical water oxidation. All the

photoelectrochemical analysis were performed using a CH 660 B potentiostat, in a three electrodes quartz cell. An Ag/AgCl/KCl saturated electrode was used as reference electrode and a Pt coil was used as counter electrode. UV light irradiation was performed using three 'TL' 20W/05 PHILIPS UV-lamps.

Amperometric I-t curves were recorded applying a constant potential of 0.400 V in 0.1 M phosphate buffer solution pH 7.0. The current was measured for the first thirty seconds in the dark, then the lamps were turned on and the electrode was irradiated with UV light with an irradiance of 6 W m⁻².

2.3 Results and Discussion

2.3.1 Alumina membranes as template

Thermal control of the kinetic

In this procedure an alumina membrane is immersed in a sol-gel reacting solution. The reaction mixture, composed of a TiO₂ precursor in acidified hydroalcoholic solution, should penetrate inside the pores of the membrane and the TiO₂ gel should fill the pores. In order to prevent the blocking of the pores, which would prevent the formation of a continuous metal oxide network within the pores, the reaction should be really slow. For this reason the control of the reaction rate is extremely important in this procedure, and it was performed by conducting the reaction in a cold bath at a controlled temperature of 0°C. Unfortunately after a few seconds from the start of the addition of the hydroalcoholic solution to the TTiP solution a white suspension was formed, suggesting that the reaction was already taking place. In fact TTiP is a very reactive species which readily reacts with water (even with the moisture of the air) following reactions 2.1, 2.2, 2.3.

The Ti(OH)₄ species give rise to polycondensation reaction leading to the formation of macromolecules and eventually nanoparticles formed by a network of O-Ti-O bonds. Figure 2.5 shows a compact layer of TiO₂ particles on the surface of the alumina membrane. Since the mean diameter of these particles is 100 - 200 nm larger than the pores diameter, it is unlikely that the pores be filled with TiO₂ nanofibers.

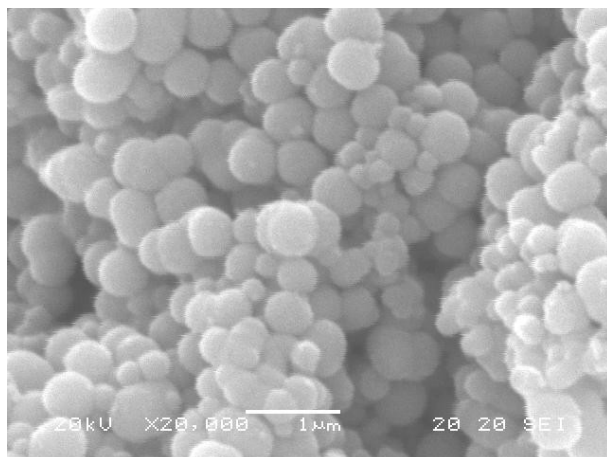


Figure 2.5. SEM image of TiO₂ particles on the surface of the modified alumina membrane.

In order to confirm this consideration, the modified membrane was cut with a diamond tip and the cross section observed by SEM. In Figure 2.6 it is possible to see a thick deposit of TiO₂ particles on the outer surfaces of the membrane, the pores, instead, look empty or barely filled. Likely, the small amount of particles present on the membrane section comes from the surface of the membrane. In fact their diameter is larger than the diameter of the pores. Therefore this method does not allow to fill the pores with TiO₂ sol because the gelation process is too fast.

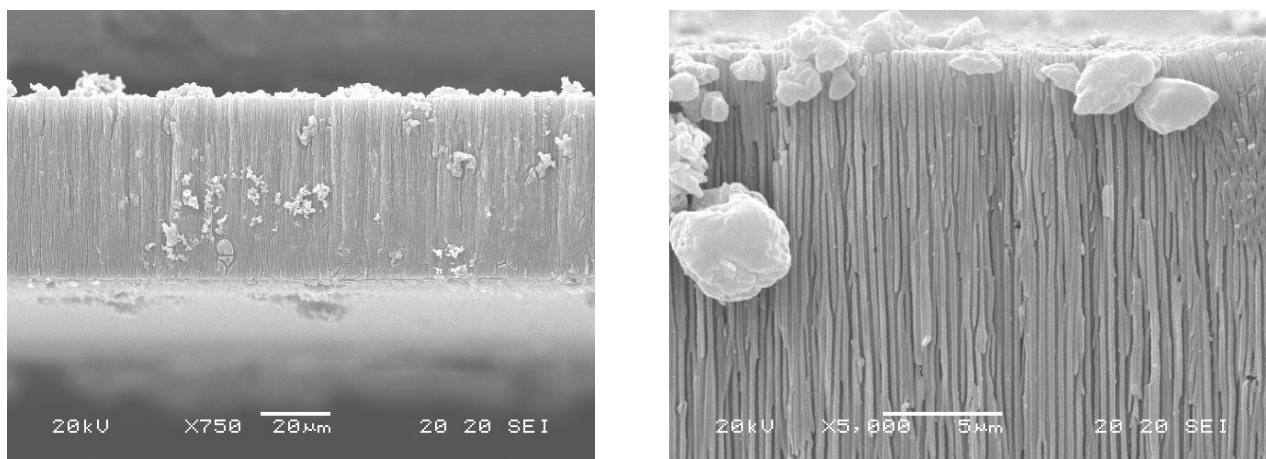
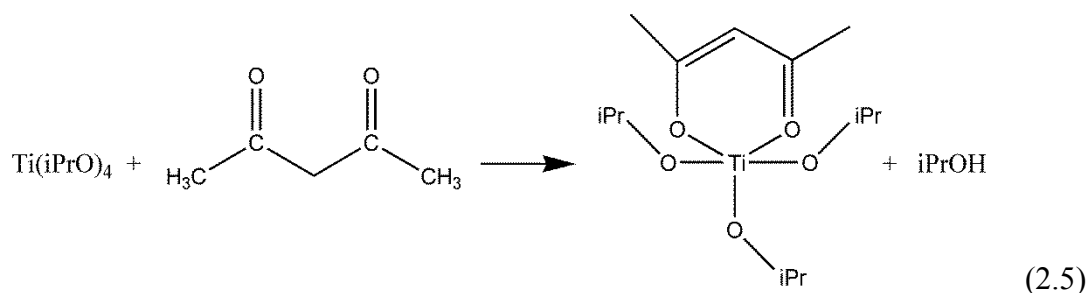


Figure 2.6. SEM images of the cross section of a TiO₂ modified alumina membrane.

Chemical modification of the titania precursor

One of the additives commonly employed to decrease the hydrolysis rate of TTiP is AcAc [13]. We decided to use this complexing agent to stabilize the precursor for the time of the pore filling process. It is well known from the literature that an equimolar mixture of TTiP and AcAc in alcoholic solvent produces a yellow colored solution, via the exothermic reaction (2.5) [12, 16].



¹H and ¹³C NMR studies, reported in the literature [12], indicate that in an equimolar mixture of AcAc and TTiP, there is no free AcAc in solution, meaning that the reaction is quantitative. This consideration was confirmed by IR spectra, which showed a broad adsorption band at 620 cm⁻¹ corresponding to ν(Ti-O-Prⁱ), and bands at 1590 and 1530 cm⁻¹ assigned to AcAc groups bonded to Ti. The addition of three water equivalents to the Ti(iPrO)₃AcAc precursor causes -iPrO ligands to be preferentially hydrolyzed. In fact, if an excess of water is added, the band at 620 cm⁻¹ completely disappears, bands at 1700 and 1720 cm⁻¹ associated to free AcAc begin to appear, but the doublet associated to AcAc bonded to Ti doesn't completely disappear even when 20 equivalents of water are added [12]. For this reason, an accurate control of the calcination step, in order to completely remove the AcAc from the TiO₂ framework, is required.

The presence of AcAc in the gelation mixture that we prepared greatly stabilized the TiO₂ precursor which, at room temperature, was stable for several hours. This long term stability, allowed us to use a syringe to push the solution inside the pores of the membrane, which was previously placed inside a special membrane holder. After the pore filling process, the membrane was yellow colored, indicating the presence of Ti complex on the membrane. Subsequently the sol filled membrane was allowed to dry at room temperature, by this way the gelation is completed and a continuous structure is obtained.

In order to get an ensemble of free standing TiO₂ nanowires the membrane was treated to remove the superficial TiO₂ layer from one side of the membrane and subsequently the template was removed without damaging the nanofibres. In order to identify the best strategies to obtain free standing TiO₂ nanowires, the best procedure for performing both steps was carefully studied as described in the following section.

Superficial TiO₂ layer removal and template etching

Previously published papers dealing with the template synthesis of metal oxide nanowires reported that surface films can be removed simply polishing the surface of the membrane with sandpaper [14,15]. Different polishing times were taken into account and successively the template was dissolved in 3 M NaOH. In Figures 2.7, 2.8, 2.9 are reported SEM images of TiO₂ nanofibers obtained with different polishing times, namely 1 minute, 3 minutes and 5 minutes, respectively, using sandpaper with grit-size 600.

In Figure 2.7a it is possible to see that the superficial TiO₂ layer was not completely removed. The titania surface layer was partially etched by NaOH solution, which eventually reached the alumina template, dissolving it. In the cracks in between the surface layer is possible to see an intricate network of TiO₂ nanofibers. Figure 2.7b reports a magnification of the modified membrane where the TiO₂ nanofibres are visible. This polishing treatment was not enough to completely remove the surface layer, demonstrating the importance of this step in defining the final morphology of the fibers.

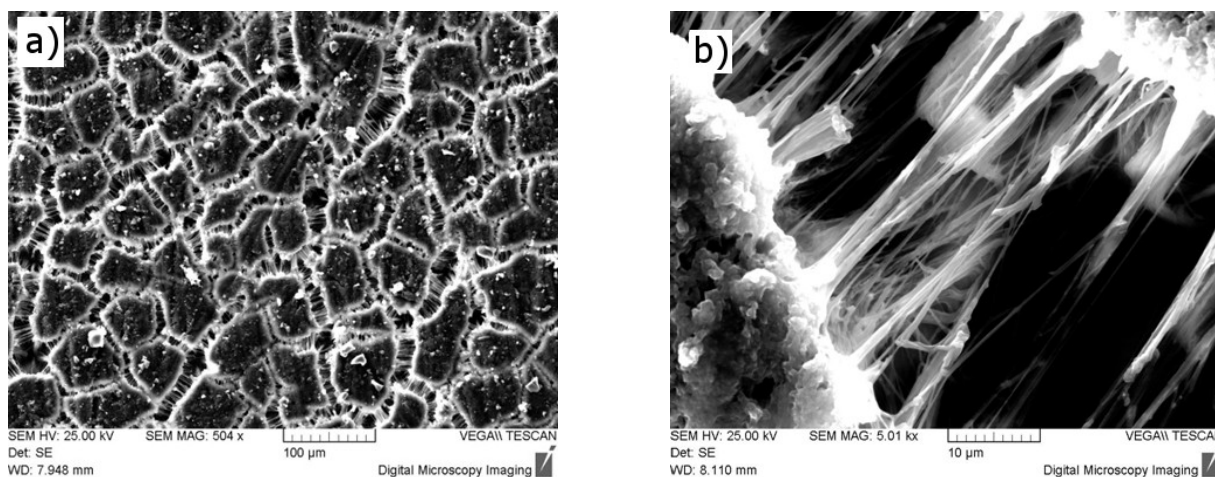


Figure 2.7. SEM image of modified alumina membrane, after 1 minute of sand paper polishing and 30 minutes of 3M NaOH etching treatment (a) and detail of the obtained TiO₂ nanofibers (b).

Figure 2.8a shows a SEM picture of the modified membrane after 5 minutes of sand paper polishing and NaOH etching. In this case it is possible to see that the surface layer was completely removed and the template was completely dissolved, nevertheless the nanofibers ensemble looks damaged and not homogeneous. Probably in some areas the nanofibres were partially removed by the polishing treatment. In Figure 2.8b an SEM image of the TiO₂ nanofibers at higher magnification is presented. The fibers look bent and shorter than expected, in fact the geometry of the nanofibres is related to the shape of the template material, since the membrane average

thickness is 60 μm , the length of the nanofibres should be nearly the same, but actually their length is approximately 10 μm , likely the nanofibres were damaged or removed during the polishing treatment.

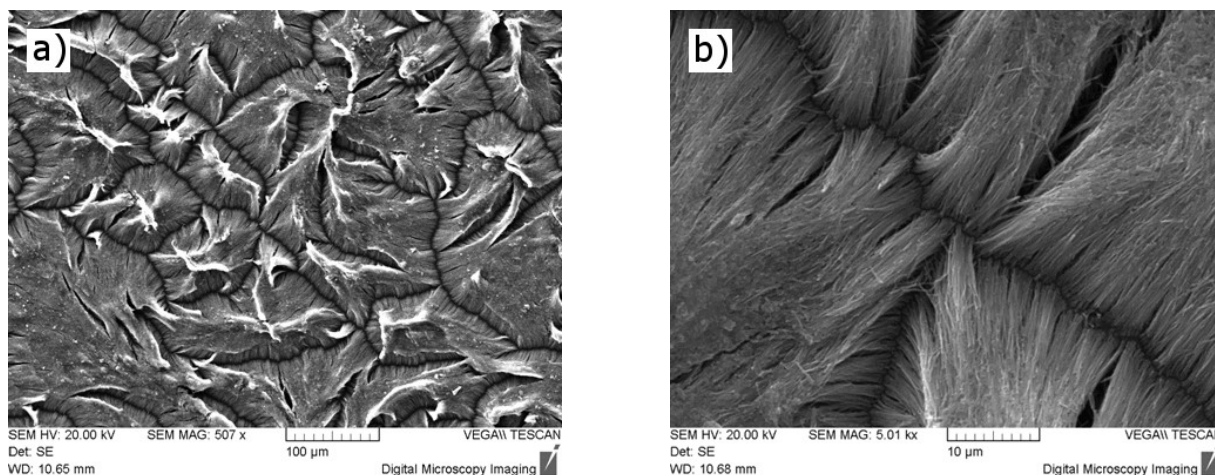


Figure 2.8. SEM image of modified alumina membrane, after 5 minutes of sand paper polishing and 30 minutes of 3M NaOH etching treatment (a) and detail of the obtained TiO₂ nanofibers (b).

Finally in Figure 2.9a is reported the SEM image of the membrane after 3 minutes of sand paper polishing and 3 minutes of NaOH etching. The picture shows nice TiO₂ nanofibers but some undesirable features are also visible. First of all, the tips of the fibers merge in bundles, limiting their surface area and the diffusion of the solution between the bundles. Since the pores of the alumina membranes are not interconnected among each other, this singular feature could be due to a surface activation toward condensation during the etching process. Secondly, high magnification SEM image, in Figure 2.9b, shows that some of the bundles are cracked, limiting the overall electron transport efficiency of the structure.

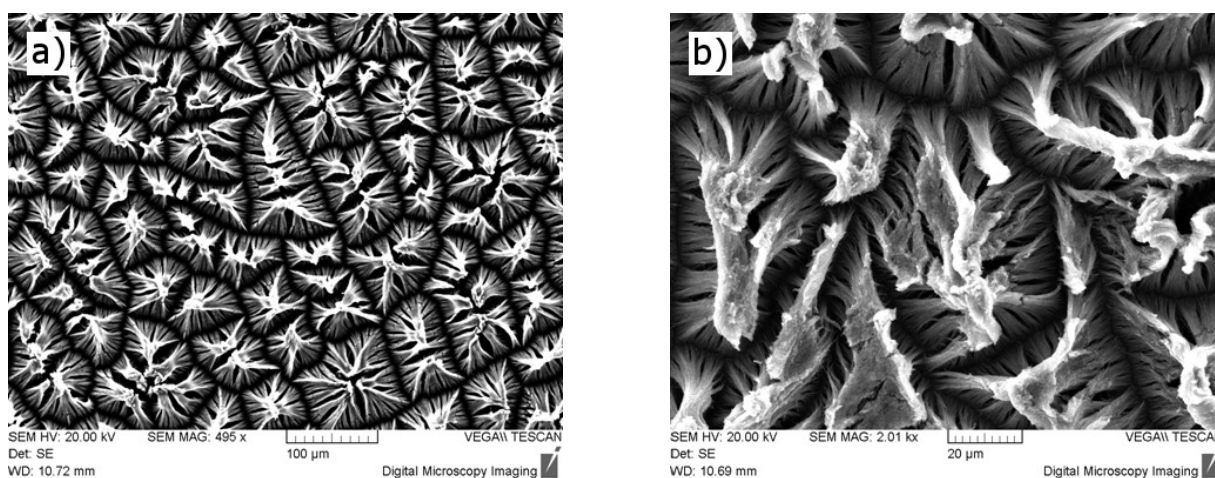


Figure 2.9. SEM image of modified alumina membrane, after 3 minutes of sand paper polishing and 30 minutes of 3M NaOH etching treatment (a) and detail of the obtained TiO₂ nanofibers (b).

The morphology of the TiO₂ nanofibers obtained by this method was not completely satisfactory, beside that, the reproducibility of the method was scarce. Several membranes were apparently polished by the same way, leading to quite different results, as far as the TiO₂ layer is concerned. Nonetheless, the chemical modification of the precursor with AcAc proved to be a viable method to slow down the reaction rate and control the stability of the sol for the time of the pore filling process. For this reason we decided to apply the same reaction procedure to a different templating material, such as a polymeric membrane, in order to exploit the different chemical properties of the organic template with regard to metal oxide fibers. This is expected to allow us to explore different techniques in the template removal procedure allowing to reduce the detrimental effects on the TiO₂ fibers.

2.3.2 Polycarbonate as template

Superficial TiO₂ layer removal and template etching

The use of a polymeric membrane should lead to an easier removal of the templating material, since the membrane may be dissolved with suitable solvents [17, 18], pyrolysed or etched by plasma treatment [19], these procedures are not detrimental for the metal oxide fibers (as in the case of NaOH). On the other hand the polymeric membranes are usually thinner and have a smaller pore density in comparison with the alumina membranes, leading to shorter fibers although in a lower number (see paragraph 1.4.2).

The nanofibers synthesis was conducted following the procedure described in paragraph 2.2 (*Chemical modification of the titania precursor*). As expected, after the synthesis, the membranes were covered with a thin yellow layer, confirming the presence of a TiO₂ layer on its surface.

In order to verify the effects of the chemical etching on the TiO₂ NWs morphology, the modified membrane was dried in an oven (100 °C) and etched in CH₂Cl₂ (without removing the outer TiO₂ layer). The suspension was subsequently filtered on an alumina membrane and the filter analyzed by SEM. Figure 2.10 reports SEM images of the TiO₂ fibers on the alumina membrane used to filter the suspension. It's possible to see that, short cylinders of 200 nm in diameter and about 500 nm in length are present. EDX analysis reported in Figure 2.11 confirms that the cylinders are fragmented TiO₂ fibers. Probably the TiO₂ fibers were broken during the chemical etching process because of the poor mechanical strength of the xerogel.

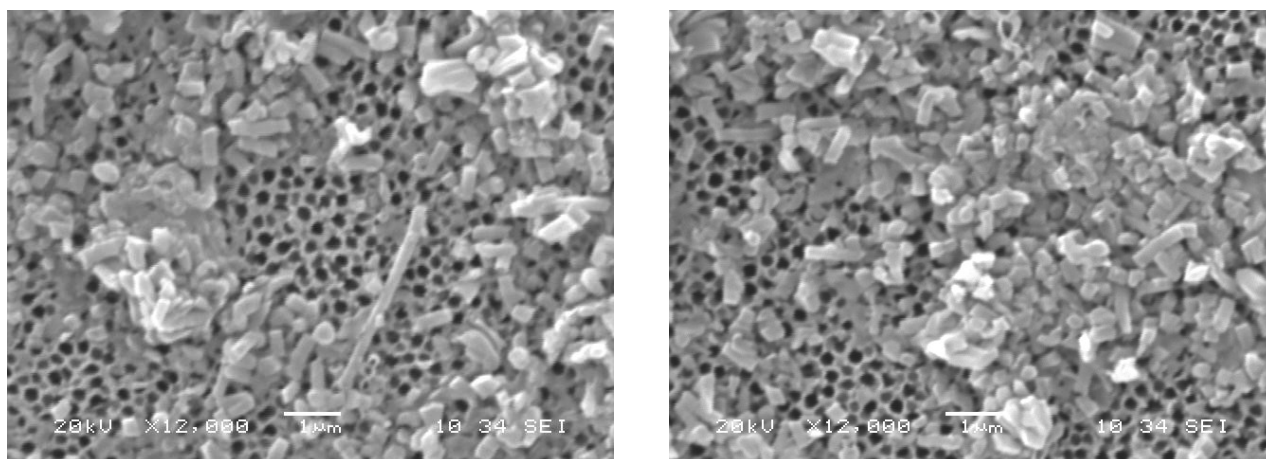


Figure 2.10. SEM image of fragmented TiO₂ nanofibers after thermal treatment at 100°C and chemical etching with CH₂Cl₂. Note that the pores in the pictures come from the membrane used for the filtration, not from the template.

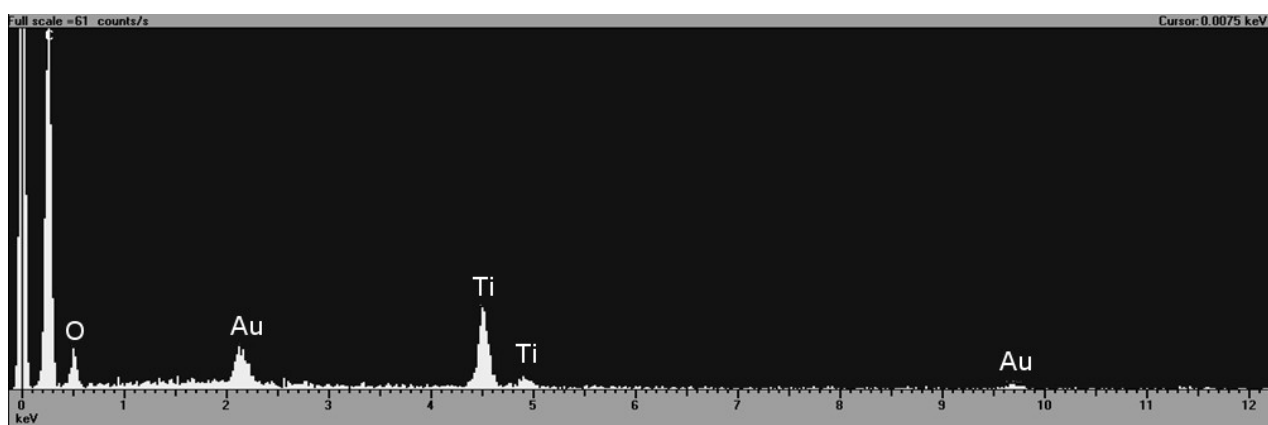


Figure 2.11. EDX analysis of the cylinders obtained after thermal treatment at 100°C and chemical etching process.

For this reason, before treatment with CH₂Cl₂, the TiO₂ modified PC membrane was heated at 200°C in order to favor the reticulation in the xerogel, consequently increasing its robustness. SEM images reported in Figure 2.12 show the sample treated at 200°C, after the etching treatment with CH₂Cl₂. In this case the self standing nanofibers are clearly visible. The fibers were not significantly damaged by the etching process and the geometry of the templating material is retained. As expected, since the outer TiO₂ layer was not removed from the template, the fibers are linked together, on both sides, by a TiO₂ film. The main drawback of this procedure is the glass transition undergone by the PC at temperatures above 150°C, which makes the polymer extremely fragile and therefore hard to handle for the following treatments.

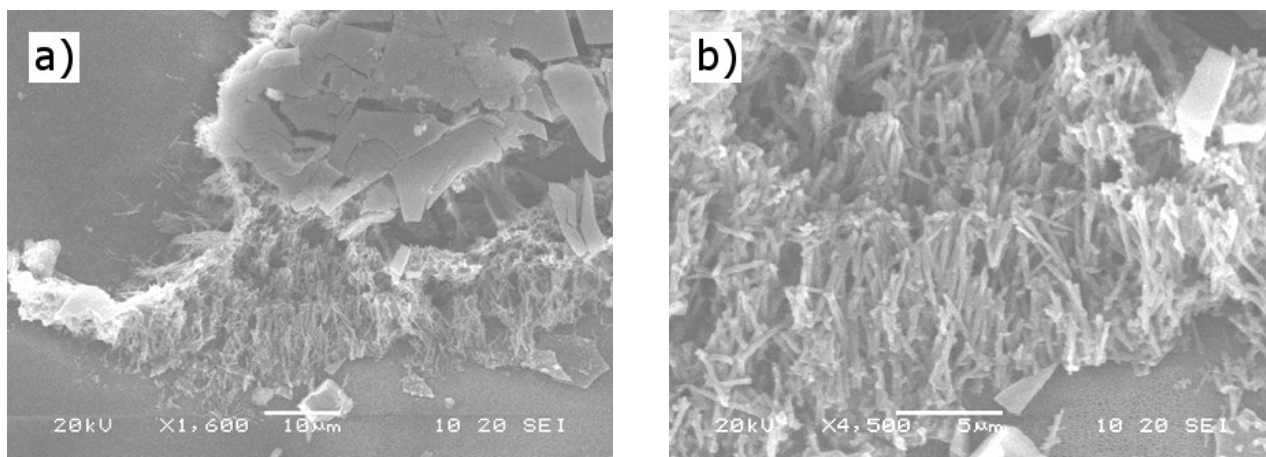


Figure 2.12. SEM image of the TiO₂ nanofibers after thermal treatment at 200°C and chemical etching with CH₂Cl₂ (a) and detail of the TiO₂ nanofibers (b).

Pyrolysis

Due to the problems encountered with the chemical etching procedure, we decided to remove the PC membrane by pyrolysis; by this way it would be also possible to oxidize the AcAc still present in the xerogel and crystallize the TiO₂ in one step. In order to choose the best pyrolysis temperature, it is necessary to evaluate the oxidation temperature of both AcAc and PC. The former was determined by temperature programmed oxidation (TPO) analysis on a non-templated TiO₂ sample, prepared with the same sol-gel recipe reported in paragraph 2.2. As shown in Figure 2.13, there is no oxygen consumption until 250°, afterward a peak is observed at 300°C. At temperatures above 400°C there is no oxygen consumption, indicating that the AcAc is already fully oxidized. From this analysis it is possible to conclude that the TiO₂ must be calcined at temperatures above 400°C in order to completely remove the AcAc from the TiO₂ framework.

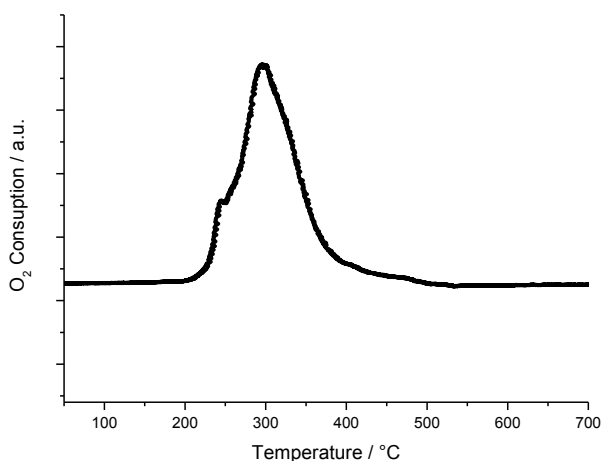


Figure 2.13. TPO graph of a non-templated TiO₂ sample prepared by modified sol-gel reaction (see paragraph 2.1.2).

The ideal temperature for the pyrolysis of the polycarbonate was evaluated by performing a thermogravimetric analysis / differential scanning calorimetry (TGA/DSC) on a non modified polycarbonate membrane. The thermogravimetric profile, reported in blue in Figure 2.14, shows that at temperatures above 600°C, the polymer is almost completely oxidized, then one could conclude that a thermal treatment at temperatures above 600°C should allow the removal of both PC and AcAc, however, at such high temperatures, TiO₂ undergoes a crystalline transition from anatase to rutile [15, 20]. Since the most photoactive crystalline phase has been reported being anatase, this kind of treatment would be detrimental for photoelectrochemical applications [8, 21]. For this reason we don't consider pyrolysis a convenient method for the template removal.

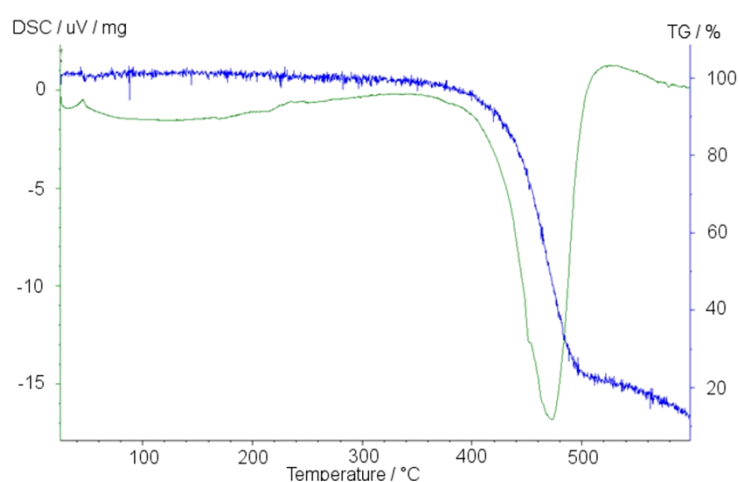


Figure 2.14. DSC/TGA of a polycarbonate membrane. TG profile is reported in blue, DSC profile is reported in green.

Plasma etching

Both the membrane oxidation and the chemical etching treatment showed limits in the removal of the templating material, besides, a suitable strategy to effectively remove the TiO₂ outer layer was not found yet. For these reasons we decided to apply a plasma treatment both for removing the outer TiO₂ layer and for etching the template. It is possible, indeed, to remove selectively the superficial TiO₂ layer and the polycarbonate membrane by using different feeding gas during plasma treatment, namely CF₄ for removing the TiO₂ and O₂ for the polycarbonate etching. Pearton et al. [22] reported that the plasma obtained with fluorinated compounds shows an improved etching of metal oxides with respect to not-fluorinated compounds (CH₄, O₂, etc.) or inert gases such as Ar. Such an improved etching rate is due to the combined physical action of the atoms colliding with the material to be etched, with a pronounced reactivity of the CF₄ ions towards metal-oxides. The reaction mechanism proposed for the plasma etching is reported below [23, 24]:



First of all the thickness of the TiO₂ outer layer was evaluated. A modified polycarbonate membrane was immersed for a few seconds in liquid nitrogen in order to decrease the resilience of the materials. The membrane was easily broken, and a cross section was observed by SEM. In this way it is possible to avoid using of cutting tools, which would lead to plastic deformations of the material, producing artifacts. The SEM image reported in Figure 2.15 indicates that the TiO₂ layer is about 800 nm in thickness. The etching rate of the CF₄ plasma was evaluated on different TiO₂ layers cast coated on silicon wafers. Different TiO₂ etchings were performed at increasing time, screening part of the sample. The height difference between the etched and screened TiO₂ film was evaluated using an optical profilometer. By this way, the etching rate has been evaluated being about 16 nm min⁻¹ (nearly 1 μm h⁻¹).

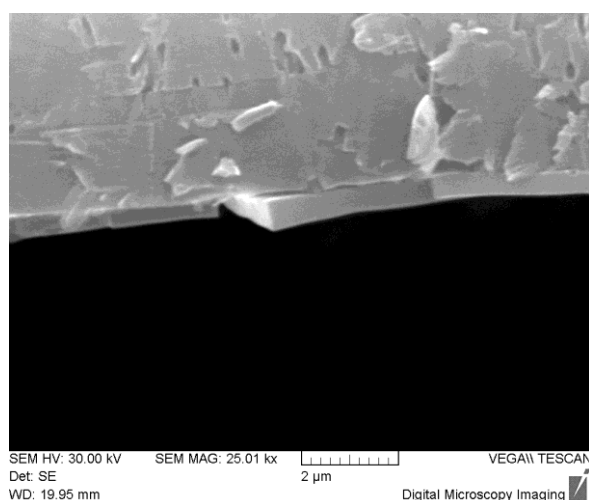


Figure 2.15. SEM image of the cross-section of a polycarbonate membrane, after TiO₂ deposition.

On this basis, we adopted the following etching procedure: the sample was treated for 1 h with CF₄ plasma to remove the outer TiO₂ layer, afterwards, the feeding gas was switched from CF₄

to O₂ in order to selectively remove the polycarbonate membrane without etching the TiO₂ nanofibers. Note that, in this case the sample did not receive any further thermal treatment to increase the robustness of the fibers (see chemical etching procedure).

In order to better understand the effect of the plasma etching on the TiO₂ outer layer, part of the membrane was covered with a thin silicon slide. By this way, the part of the membrane covered with the silicon slide was screened from the plasma etching. In Figure 2.16, SEM images of a TiO₂ modified polycarbonate membrane, after CF₄ and O₂ plasma etching, are reported. In Figure 2.16a is quite evident the difference in morphology, between the right side of the membrane, which was screened from the plasma, and the left side of the membrane which was exposed to the plasma etching. The slits on the surface of the TiO₂ layer are probably due to the shrinkage of the gel during the drying step. In Figure 2.16b the TiO₂ nanofibers are reported in more detail. They are self standing and do not show any evident damage. This images clearly confirms that the plasma treatment allows to effectively remove both the outer metal oxide layer and the polymeric template. Furthermore this procedure allows to obtain unbroken fibers even without thermal treatment, as in the case of the chemical etching. This could be due to a reticulating effect of the oxygen plasma on the TiO₂ fibers which increased their robustness.

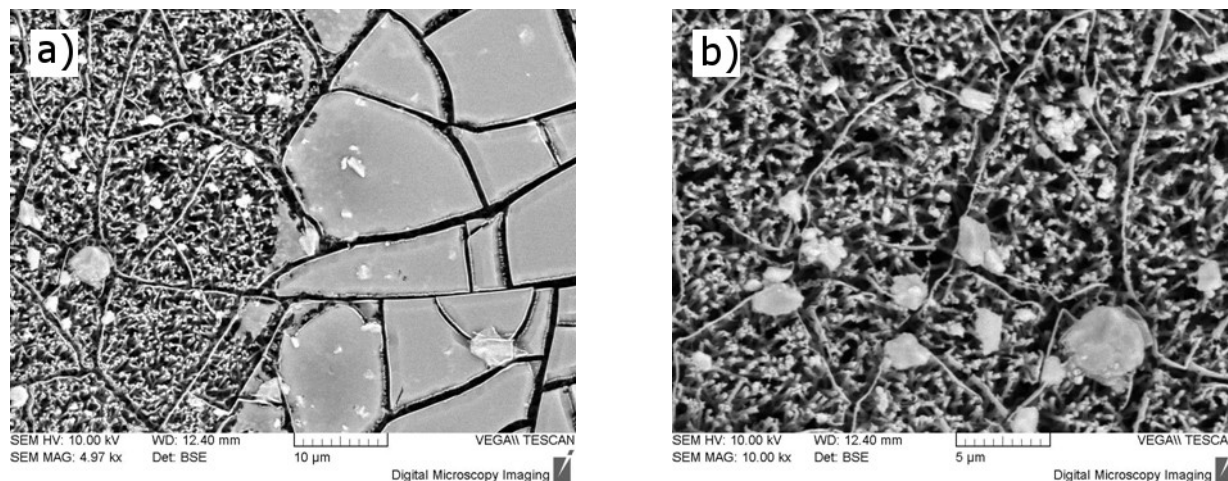


Figure 2.16. SEM image of a TiO₂ modified polycarbonate membrane after the CF₄ and O₂ plasma treatment (a), on the left side the membrane was exposed to the plasma, on the right side the membrane was screened using a Si slide. (b) Magnification of the TiO₂ nanofibers after the plasma treatment.

In order to better evaluate the effect of the thermal treatment on the morphology of the nanofibers, TiO₂ modified membranes, which were heated at 200°C, were also submitted to the plasma etching treatment. The membranes were subsequently characterized by SEM (see Figure 2.17). Again the fibers were self standing and unbroken even after the template was removed. All

the membranes gave a density of nanofibers between $2.5\text{-}3 \times 10^8$ fibers cm^{-2} . Note that the pore density in the polycarbonate membrane we used as templating material is 3×10^8 indicating that by this procedure, almost all the pores were filled with TiO₂. This result confirms that the etching with reactive ion plasma allows to avoid a thermal pretreatment, as in the case of chemical etching, nonetheless a calcination step, in order to favor the crystallization of the fibers, is still needed.

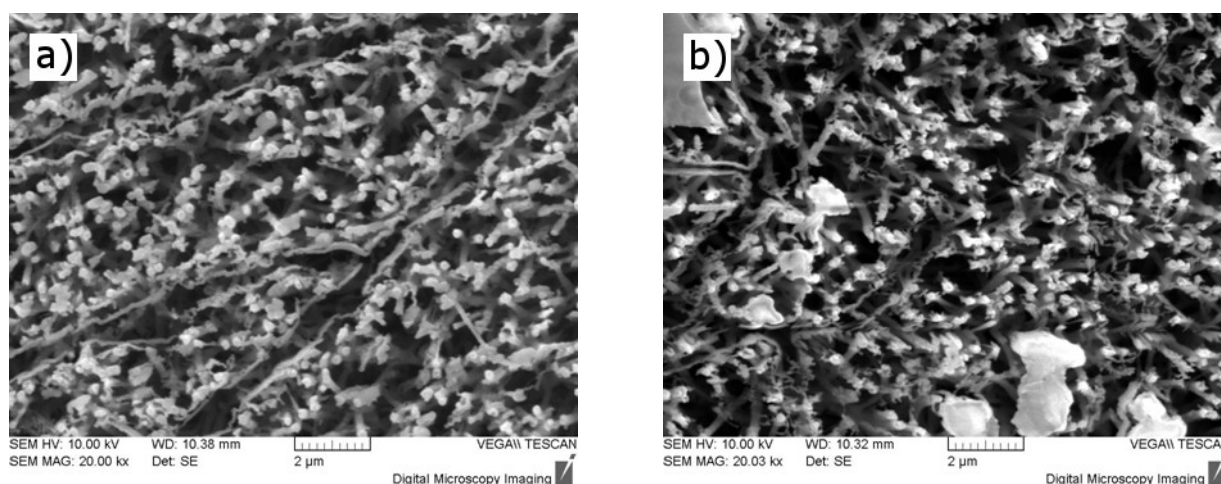


Figure 2.17. SEM images of TiO₂ modified membranes, heated at 100°C (a) and 200°C (b), after CF₄ and O₂ plasma etching.

Crystallographic phase characterization

Figure 2.18 shows the Raman spectrum of TiO₂ nanofibers obtained by sol-gel template on PC membrane, after plasma treatment and calcination at 500°C. According to factor group analysis, anatase has six Raman active modes (A_{1g} + 2B_{1g} + 3E_g). The Raman spectrum of an anatase single crystal shows that the six allowed modes appear at 144 cm^{-1} (E_g), 197 cm^{-1} (E_g), 399 cm^{-1} (B_{1g}), 513 cm^{-1} (A_{1g}), 519 cm^{-1} (B_{1g}), and 639 cm^{-1} (E_g) [25]. The main spectral features of the sample are closely similar to those of reference TiO₂-anatase, which means that the prepared nanofibers are crystalline in the anatase form [26].

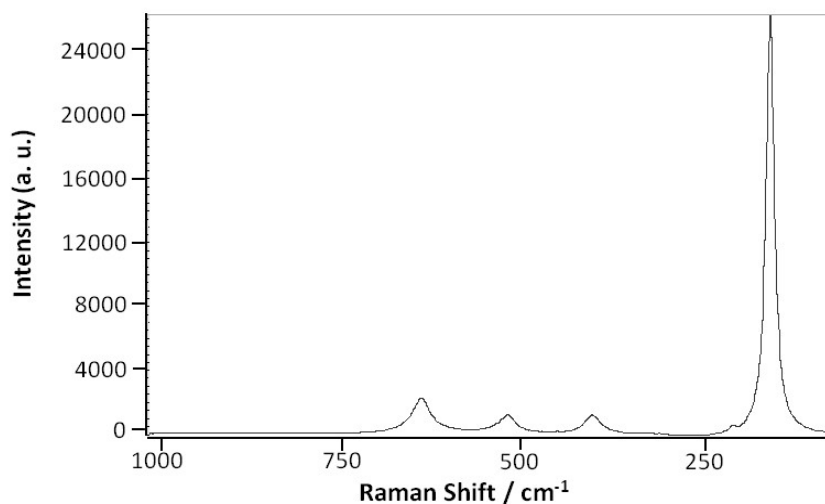


Figure 2.18. Raman spectrum of TiO₂ nanofibers.

Electrode fabrication

In order to exploit the TiO₂ nanofibers as a nanostructured semiconductor electrode for photoelectrochemical applications, it is necessary to obtain an electrical contact between an electrode and TiO₂ back layer. We tried different approaches to this aim, such as:

- Using a TiO₂ nanoparticles paste as binder between the ITO and the TiO₂ NF array;
- Using a small volume of sol as binder,

Unfortunately all our efforts didn't allow us to obtain an usable electrode. For this reason, we decided to mill the etched membrane as already described in paragraph 2.2. The same technique was used for the fabrication of TiO₂ nanoparticles (NPs) electrode. The reference material, used for this purpose, is a commercial TiO₂ powder (Degussa p25), extensively used as reference material in photochemical applications due to its remarkable photochemical activity and elevated crystallinity. The surface of both electrodes were characterized by SEM (see Figure 2.19). As expected, the long range order of the TiO₂ NF array is lost due to the milling process. In fact, as evident from Figure 2.19a, the NF array was broken in pieces as small as 50-100 μm² where the NF are still protruding from the TiO₂ back layer. The commercial TiO₂ powder, instead, formed a dense and homogeneous layer nearly 80 μm thick (see Figure 2.19b). The nanoparticles constituting the commercial sample are too small to be seen with a conventional SEM, being as small as 20-30 nm [27].

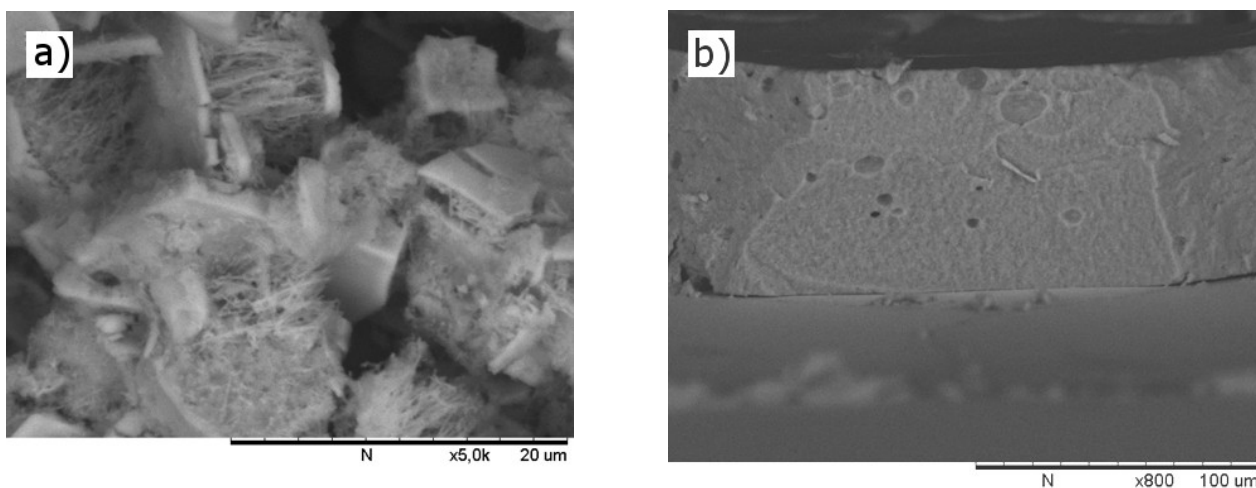


Figure 2.19. SEM images of TiO₂ NF electrode a) and cross section of a p25 electrode b), both prepared by doctor-blade technique.

Photoelectrochemical water oxidation

Both the electrodes prepared using a commercial TiO₂ powder and TiO₂-anatase NF were tested in the photoelectrochemical water oxidation. This reaction could be particularly important for the production of H₂ to be used as energetic vector (see paragraph 1.2.4).

The amperometric *i*-*t* curves recorded are reported in Figure 2.20.

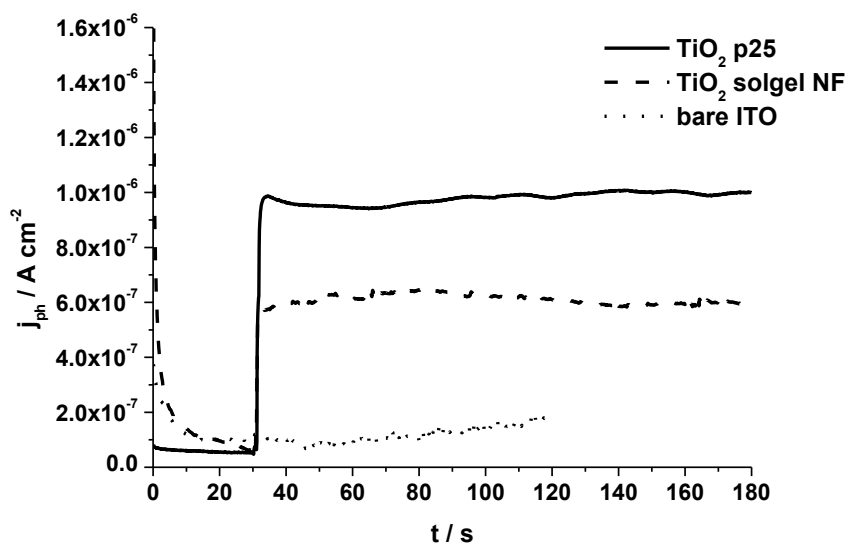


Figure 2.20. Photocurrent measured at 0.400 V vs Ag/AgCl KCl sat. in 0.1 M phosphate buffer solution pH 7. (Straight line p25 electrode, dashed line template NF electrode, dotted line bare ITO electrode).

The current measured under UV irradiation includes the current related to the photoelectrochemical oxidation at the semiconductor electrode plus the double layer and space charge region charging current. Since also charging and residual currents scale with the surface area of the working electrode, it is necessary to evaluate the contribution of these currents, in order to extract the real photoelectrochemical contribution from the overall current. For this reason, a preemptive polarization measurements in the dark was performed (first 30 s on the plots), afterwards, the UV lights were turned on and the photocurrent was recorded. The final photocurrent values taken into account are indeed the difference between the current measured in the dark and the plateau current recorded after 140 s of irradiation. Note that, using a bare ITO, as photoanode, no photocurrent is recorded. The photocurrents values obtained as described above are $0.53 \mu\text{A cm}^{-2}$ using a TiO₂ NF electrode and $0.95 \mu\text{A cm}^{-2}$ using a p25 electrode. This result could be due to a lower surface area of the NF electrode compared to the NP electrode. In fact, similar results were reported in the literature [28, 29]. Law et al., for example, used an array of ZnO nanofiber as photoanode in a DSSC, obtaining an overall conversion efficiency lower than the NP counterpart. Nevertheless, quasi 1-D structures (i.e nanorods, nanowires, nanofibers) proved to be promising materials for photoelectrochemical application, due to an improved electron transport coefficient [30], which would allow a fast electron transport towards the counter electrode, limiting the electron-hole recombination events. On top of that, the milling procedure which allowed us to obtain a paste to be casted on the surface of the ITO, disrupts the long term order of the NF array, limiting in some extent, the advantages related to linear nanostructures.

2.4 Conclusions

A sol-gel templated procedure, for the preparation of TiO₂ nanofibers, was developed, using nanoporous membrane as structure directing agents. An accurate control of the reaction rate was found to be crucial in order to allow the sol to penetrate inside the pores of the membranes and to obtain an array of self standing TiO₂ nanowires. The control of the kinetics by reducing the temperature of the reaction bath, was found insufficient for our purposes, the titania precursor gelation was too fast under these conditions and resulted in poorly filled pores. For this reason AcAc was used as complexing agent of the TiO₂ precursor, reducing effectively the hydrolysis and condensation reaction kinetics. Both alumina and polycarbonate membranes were taken into account as templating material. In both cases self standing and dense TiO₂ nanofibers were obtained. PC was found preferable, due to the easier removal of the outer TiO₂ layer and templating

material. Moreover, the crystallographic structure of the obtained nanofibers were characterized by Raman and has been identified as anatase.

Unfortunately it was not possible to obtain an effective electrical contact between the TiO₂ NF array and a transparent conductive electrode, without disrupting the long range structure of the semiconductor material. Nonetheless, the TiO₂ nanofibers were used for the fabrication of a semiconductor electrode to be tested in the photoelectrochemical water oxidation. The photocurrent obtained using this electrode was found being lower than the corresponding nanoparticles electrode. This result is probably due to the limited surface area of the nanofibers. Besides, the advantages in term of fast electron transport and electron-hole separation efficiency are obtained when the orientation of the nanofibers allows a direct path from the tips of the nanofibers to electrode substrate, probably, such a condition is not met by our TiO₂ NF electrode which is constituted by a stack of randomly oriented nanofibers.

Therefore, it is essential to find a reliable method to obtain an handable electrode maintaining the long term structure of the TiO₂ array, for example by sputtering a layer of gold on the outer TiO₂ layer, in order to increase its robustness. This electrode would be tested for the photoelectrochemical water oxidation reaction in order to confirm the beneficial effect of 1D nanostructures on the charge carrier separation, but also as photoanode in DSSC.

As long as we will not be able to attach the fibers array to the ITO, without disrupting its order, it will not be possible to exploit the full potentials of this material. For this reason we decided to explore a different technique for the preparation of nanostructured semiconductor electrodes. Furthermore, we decided to obtain a morphology which allows an increase of the surface area keeping the electron transport as fast as possible.

References

- [1] M. Signoretto, E. Ghedini, V. Trevisan, C. L. Bianchi, M. Ongaro, G. Cruciani, *Appl. Catal. B-Environ.* **95** (2010) 13
- [2] A. K. M. Kafi, G. S. Wu, P. Benvenuto, A. C. Chen, *J. Electroanal. Chem.* **662** (2011) 64
- [3] B. O'Regan, M. Graetzel, *Nature* **353** (1991) 737
- [4] H. Li, S. K. Martha, R. R. Unocic, H. Luo, S. Dai, J. Qu, *J. Power Sources* **218** (2012) 88
- [5] M. Signoretto, E. Ghedini, F. Pinna, V. Nichele, V. Crocella, G. Cerrato, *Mat. Res. S. C.* **139** (2011) 189
- [6] J. Yu, J. C. Yu, M. K.-P. Leung, W. Cheng, B. Ho, X. Zhao, J. Zhao, *J. Catal.* **217** (2003) 69
- [7] M. Kolar, H. Mestankova, J. Jirkosvky, M. Heyrovsky, J. Subtr, *Langmuir* **22** (2006) 598
- [8] K. Yanagisawa, J. Ovenstone, *J. Phys. Chem. B* **103** (1999) 7781
- [9] C. B. Almquist, P. Biswas. *J. Catal.* **212** (2002) 145
- [10] A. Narotsky, J. C. Jamieson, O. J. Kleppa, *Science* **158** (1967) 338
- [11] S. Bakardjieva, V. Stengl, L. Szatmary, J. Subrt, J. Lukac, N. Murafa, D. Niznansky, K. Cizek, J. Jirkovskyc, N. Petrova, *J. Mater. Chem.* **16** (2006) 1709
- [12] C. J. Brinker, G. W. Scherer, *Sol-Gel Science: The Physics and Chemistry of Sol-Gel Processing* (1990) Accademic Press, UK
- [13] J. Livage, M. Henry, C. Sanchez, *Prog. Solid State Chem.* **18** (1988) 259
- [14] B. B. Lakshmi, P. K. Dorhout, C. R. Martin, *Chem. Mater.* **9** (1997) 857.
- [15] A. S. Attar, M. S. Ghamsari, F. Hajiesmaeilbaigi, Sh. Mirdamadi, K. Katagiri, K. Koumoto, *J. Mater. Sci.* **43** (2008) 5924
- [16] U. Schubert, *J. Mater. Chem.* **15** (2005) 3701
- [17] M. De Leo, A. Kuhn, P. Ugo *Electroanalysis* **19** (2007) 227
- [18] K. Krishnamoorthy, C.G. Zosky *Anal Chem.* **77** (2005) 5068
- [19] S. Yu, N. Li, J. Wharton, C. R. Martin *Nano Lett.* **3** (2003) 815
- [20] K. Okada, N. Yamamoto, Y. Kameshima, A. Yasumor, K. J. D. MacKenzie, *J. Am. Ceram. Soc.* **84** (2001) 1591
- [21] A. Fujishima, T. N. Rao, D. A. Tryk, *J. Photochem. Photobiol. C* **1** (2000) 1
- [22] S. Norasetthekul, P. Y. Park, K. H. Bark, K. P. Lee, J. H. Shin, B. S. Jeong, V. Shishodia, E. S. Lambers, D. P. Norton, S. J. Pearton, *Appl. Surf. Sci.* **185** (2001) 27
- [23] S. J. Pearton, D. P. Norton, *Plasma Process Polym.* **2** (2005) 16
- [24] X. Zhang, M. Jin, Z. Liu, D. A. Tryk, S. Nishimoto, T. Murakami, A. Fujishima, *J. Phys. Chem. C* **111** (2007) 14521

- [25] H. C. Choi, Y. M. Jung, S. B. Kim, *Vibr. Spectrosc.* **37** (2005) 33
- [26] X. Xue, W. Ji, Z. Mao, H. Mao, Y. Wang, X. Wang, W. Ruan, B. Zhao, J. R. Lombardi, *J. Phys. Chem. C* **116** (2012) 8792
- [27] K. J. A. Raj, B. Viswanathan *Indian J. Chem.* **48A** (2009) 1378
- [28] M. Law, L. E. Greene, J. C. Johnson, R. Saykally, P. Yang, *Nat. Mater.* **6** (2005) 455
- [29] M. Y. Song, D. K. Kim, K. J. Ihn, S. M. Jo, D. Y. Kim, *Synth. Mat.* **15** (2005) 77
- [30] P. S. Archana, R. Jose, C. Vijila, S. Ramakrishna, *J. Phys. Chem. C* **113** (2009) 21538

3. Linear and Hierarchically Branched ZnO Nanofibers

3.1 Introduction

ZnO is a semiconductor characterised by a wide band gap (3.37 eV) with large exciton binding energy (60 meV) [1]; it finds application in many fields such as photovoltaics, gas sensors, photocatalysis, energetics, optics, and photoelectrochemical cells. Thanks to its superior electron mobility, the ease of crystallization and possibility of anisotropic growth [2], ZnO is considered a suitable substitute for TiO₂. Moreover, ZnO can be prepared in a variety of morphologies such as: nanorods [3], nanobelts, nanosaws [4], nanosprings, nanorings [5], nanostars [6]. As already seen in chapter 1, the nanostructuring of this semiconductor into quasi 1-D nanostructures (nanowires) is considered promising for photoelectrochemical applications [7-9]. However, a limit in the photoelectrochemical performances of linear nanostructures can come from their relatively low surface area, in comparison with other morphologies. Recently, many efforts were put on the integration of 1D nanoscale building blocks into 3D architectures. The goal is to develop hierarchical structures in which the surface area of the semiconductor is enhanced, while keeping the electron transport efficiency as high as possible. Shen et al. [10] reported the growth of a number of hierarchical structures, such as ZnO nanocones or nanobottles. Some of these complex structures are obtained by exploiting physical methods of preparation, such as chemical vapour deposition (CVD), plasma enhanced chemical vapour deposition (PECVD) and thermal evaporation; however, such methods require expensive instrumentation, are energy consumptive and are not suitable for large-scale production. Hydrothermal growth is considered a good candidate for low cost production of nanostructured ZnO materials, but this technique can be time consuming since a seeding layer deposition step is required [3]. Cathodic electrodeposition has been recognized as one of the most effective methods to prepare nanomaterials since it is simple and economic, does not require vacuum or extreme temperature and can be easily scaled up. By changing the process parameters, (i.e. applied potential, concentration and pH of the electrolyte, operating temperature and deposition time), the film morphology and thickness can be controlled [11]. Electrochemical deposition methods are based on the fast and cheap cathodic deposition of ZnO onto a suitable working electrode substrate. Usually, the mechanism is based on the reduction of a precursor such as nitrate [12] (see eq. 3.1), hydrogen peroxide [13] (see eq. 3.2) or dissolved O₂ [14] (see eq. 3.3); all these three reactions produce at the electrode/solution interface a large OH⁻ concentration:

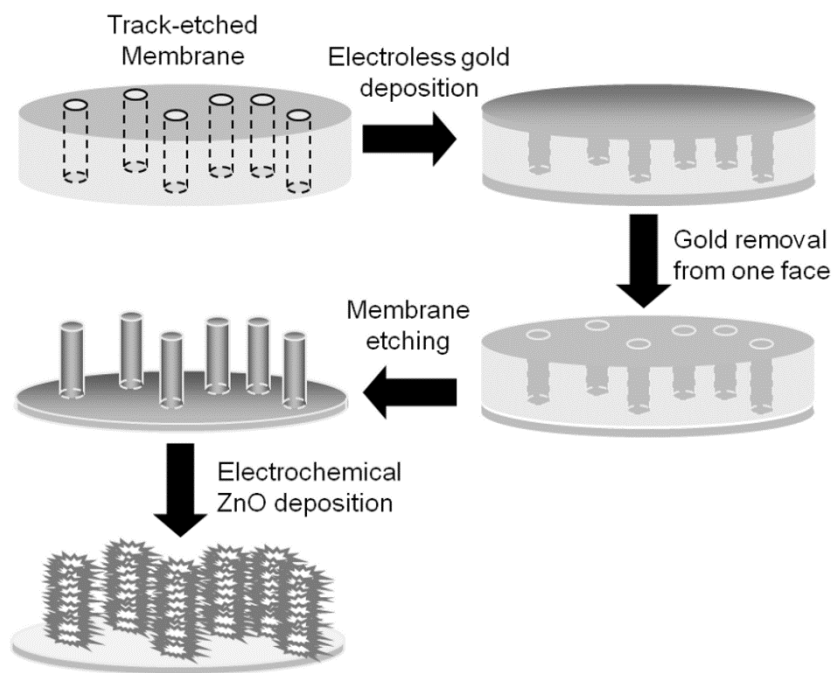


The local generation of hydroxyl anions causes the precipitation of $\text{Zn}(\text{OH})_2$ on the electrode surface, which, at relatively high temperatures ($>34^\circ\text{C}$) [15], is dehydrated to ZnO (see eq. 3.4). Since the growth of the semiconductor on the [0001] plane of the ZnO crystals is faster, a deposit with the shape of nanorods or nanowires is typically obtained [16].



If a nanostructured electrode is employed as the substrate, a hierarchical semiconductor electrode can be obtained. For instance, Xu et al. [17,18] developed a synthetic route for the preparation of twofold and sixfold hierarchical structures, by multiple electrochemical depositions on transparent electrodes. More recently, Elias et al. [19] developed a synthetic approach, based on O_2 reduction, to fabricate ordered hollow urchin-like ZnO NWs grown on a multilayer of polystyrene micro-spheres used as the templating substrate.

In the present work we focus on the electrochemical growth of ZnO nanowires (NWs), onto ensembles of gold nanowires (Au NWs); the final product of the process being an ensemble of hierarchically branched ZnO -Au nanostructures. The preparation sequence is summarized in Scheme 3.1.



Scheme 3.1. Preparation of ZnO branched nanowires.

At first, an ensemble of Au nanoelectrodes is obtained by membrane template deposition [20, 21], then, it is etched to expose the nanowires [22, 23], which are finally used as the substrate for the electrochemical growth of the ZnO NWs. By this way, hierarchically built nanostructures are generated, in which the ZnO NWs were grown as fir needles on Au nanobranched.

At the best of our knowledge this is the first example of combined use of membrane template deposition of 1-D nanostructures, with electrochemically directed branching of semiconductor subnanostructures.

One problem encountered with the characterization of so small and complex nanomaterials is the determination of the crystal structure of the individual nanostructure. To this aim we applied the electron back scatter diffraction (EBSD) technique, which allows one to perform the crystallographic analysis with high spatial resolution [24,25].

3.2 Experimental

Electrochemical and photoelectrochemical apparatus

All the electrochemical analysis and depositions were performed using a CH 660 B potentiostat. The photoelectrochemical water oxidation experiments were conducted in a three

electrode quartz cell. UV light irradiation was performed using three 'TL' 20W/05 PHILIPS UV-lamps.

FEG-ESEM (Field Emission Gun Environmental Scanning Electron Microscopy) and electron backscatter diffraction analysis

SEM and FEG-ESEM analyses were performed with a tabletop Hitachi TM3000 SEM and with a FEI Quanta FEG-ESEM, respectively. EBSD analyses were conducted in the FEI Quanta FEG-ESEM microscope operating at an accelerating voltage of 20 kV, with a working distance of 10 mm and the sample tilted of 75° to horizontal. The EBSD facility included the EDAX-TSL DigiView detector consisting of a DVC-1412M digital camera with CCD sensor and a circular phosphor screen as intensifier. The TSL software OIM 5.31™ package was used to collect, index and analyse EBSD patterns.

Template fabrication of NEEs

Specific details, related to the synthetic procedure and to the electrochemical and optical properties of NEEs, can be found in the first original papers [20, 23, 26, 27] as well as in more recent reviews [21, 28-30]. Briefly, polycarbonate filtration membranes (SPI-Pore, 47 mm filter diameter, 6 µm filter thickness, $6 \cdot 10^8$ pores cm^{-2}) with a nominal pore diameter of 80 nm were used as template to prepare 3D-NEEs. After sensitizing the polycarbonate membrane by immersion into a 0,026 M SnCl_2 solution and 0,07 M CF_3COOH in 50:50 methanol/water for 45 minutes the membrane was immersed in a 0,029 M $\text{Ag}[(\text{NH}_3)_2]\text{NO}_3$ solution for 10 minutes. Afterward the membrane was immersed into a gold plating bath ($7.9 \cdot 10^{-3}$ M $\text{Na}_3[\text{Au}(\text{SO}_3)_2]$ and 0.127 M Na_2SO_3) which was kept at 0°C. After 20 minutes, 1 mL of formaldehyde (37 %) was added and after 1 hour one additional mL of formaldehyde (37 %) was added. The deposition was then allowed to proceed for another 23 hours after which the membrane was rinsed in deionized water and immersed in HNO_3 10 % for 12 hours. The membrane was finally rinsed in water and dried, resulting in the deposition of continuous gold nanowires within the pores and on both sides of the membrane faces. The smooth side of the membrane was peeled off with adhesive tape 3M (scotch Magic™) so that the tips of the nanowires remain exposed on one side. All the nanowires are interconnected to each other by a gold back layer which acts as current collector. Afterwards the membrane was etched with oxygen plasma to completely remove the polycarbonate, obtaining the so called 3D-NEEs. The

following etching conditions have been used: oxygen flux 100 mL min^{-1} , power 700 W, etching time 60 minutes. Figure 3.1 shows the SEM image of an ensemble of Au NWs 80 nm in diameter.

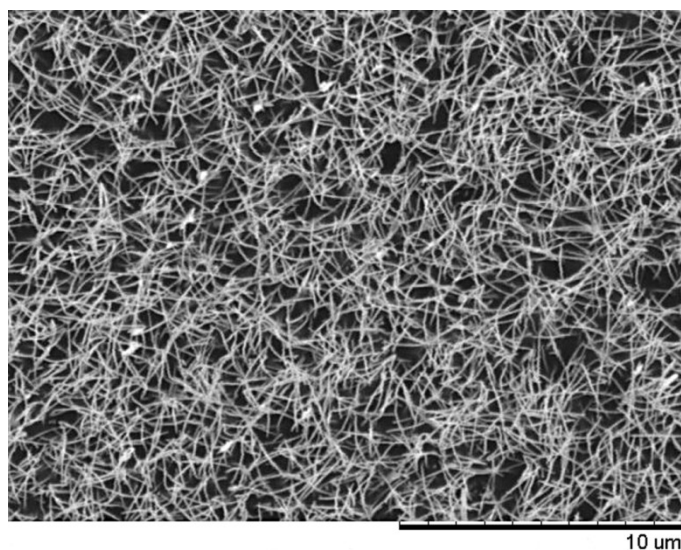


Figure 3.1. SEM image of 3D-NEE obtained by electroless gold deposition on track-etched polycarbonate membrane with nominal pore diameter of 80 nm, after oxygen plasma treatment.

The gold “nanobrush” was assembled to obtain an electrode as sketched in Figure 3.2 according to the following procedure. A piece of copper adhesive tape (5x60 mm) with conductive glue (Ted Pella, Inc.) is first affixed on a small adhesive non conductive aluminium square and then to a 5x5 mm piece of gold “brush”, so that only a small part is in contact with the copper tape, this is because the conductive glue on the copper tape contains Ni particles which could damage the gold layer [20]. Finally strips of non conductive tape are applied to the lower and upper side of the assembly in order to insulate the aluminium and copper tape. A circular hole with an area of 0.07 cm^2 is punched into the upper piece of insulator prior to its placement on the assembly. This hole defines the geometric area of the ensembles, that is the area exposed to the solution.

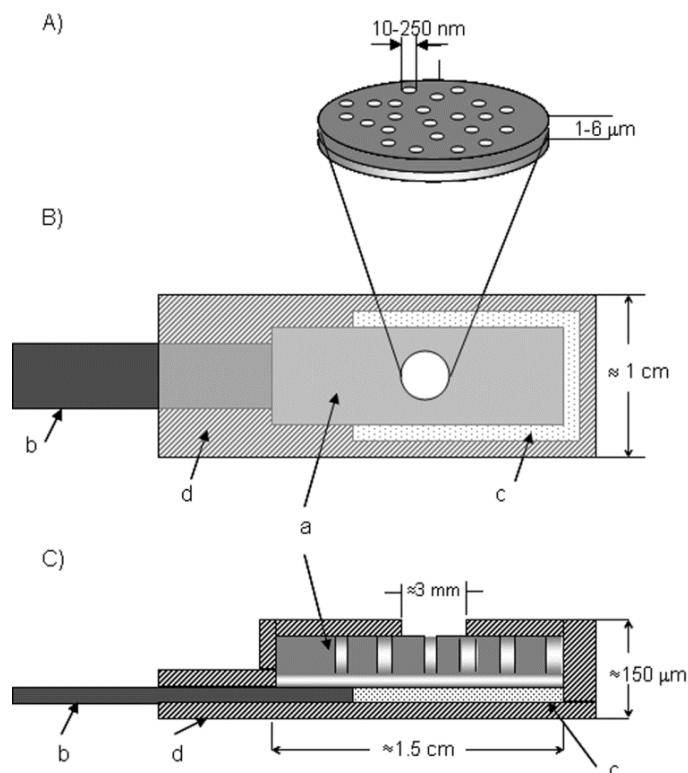


Figure 3.2. Scheme of an Au-NEE prepared using a track-etched polycarbonate membrane as template. A). Particular of the section of the active area; B) top view, C) section of the all NEE ready for use as working electrode. a: track-etched golden membrane; b: copper adhesive tape with conductive glue to connect to instrumentation; c: aluminium adhesive foil with non-conductive glue; d: insulating tape. Not all details (namely, the nanoelectrodes dimension) are in scale.

Optimization of ZnO deposition parameters

The electrochemical system involved in the ZnO deposition has been studied by cyclic voltammetry (CV). The analysis was performed in a thermostated three electrodes cell, at 85°C in a 5 mM hexamethylenetetramine ($C_6H_{12}N_4$, HMTA) and 5 mM $Zn(NO_3)_2$ or 5 mM $ZnCl_2$ aqueous solution. The reagents were used as received from Alfa Aesar. Both ITO (Delta technologies, Indium Tin Oxide coated glass, $R_s = 4 - 8 \Omega$) electrodes and 3D-NEEs were used as working electrode, an Ag/AgCl KCl saturated electrode was the reference electrode and a platinum coil was the counter electrode. In this chapter, all potentials are quoted versus Ag/AgCl KCl saturated electrode. The potential was scanned from 0 V to -0.800 V with a scan rate 10 mV s^{-1} . In order to evaluate the effect of oxygen concentration, the voltammetric analysis was performed before and after deoxygenating the solution and in oxygen saturated solution. The oxygen was

removed/dissolved by bubbling nitrogen/oxygen in the solution for thirty minutes and performing the experiments under a nitrogen/oxygen atmosphere.

Semiconductor electrode fabrication

ZnO electrodeposition experiments, were performed using the above reported conditions, operating at a constant potentials of -0.550 V or -0.700 V. Gold nanowires arrays and ITO electrodes were alternatively used as the working electrode. Also the electrodeposition experiments were conducted at three different oxygen concentration, namely, in nitrogen purged solution, in the presence of dissolved oxygen and in oxygen saturated solution. At the end of the growth time (typically 30 minutes) the working electrode was removed from the solution and immediately rinsed with deionized water to remove any residual salt from the surface.

Twenty different samples, one for each deposition condition and substrate, were obtained and labeled using the format “WWWXXXYYZZ”, where “WWW” defines the substrate i.e. ITO or NEE, “XXX” defines the deposition potential that is 550 if the deposition was conducted at -0.550 V and 700 if it was conducted at -0.700 V, “YYY” defines the zinc salt used in the deposition, NO3 for Zn(NO₃)₂ or Cl2 for ZnCl₂, and finally “ZZ” defines if the deposition was performed in air “Ai” in nitrogen purged solution “N2” or in oxygen saturated solution “O2”. For example, ZnO NWs grown on 3D-NEE at a potential of -0.700 V in a Zn(NO₃)₂ deoxygenated solution would be labeled NEE700NO3N2.

Photoelectrochemical water oxidation experiments

Amperometric I-t curves were recorded applying a constant potential of 0.400 V in 0.1 M phosphate buffer solution pH 7.0. The current was measured for the first thirty seconds in the dark, then the lamps were turned on and the electrode was irradiated with UV light with an irradiance of 6 W m⁻².

3.3 Results and Discussion

Electrochemical ZnO deposition

Preliminary CV experiments showed that oxygen reduction takes place at -0.450 V while nitrate reduction occurs at approximately -0.700 V, on ITO and at -0.500 V on 3D-NEE (not shown). The observed anticipation of the NO_3^- reduction potential at the 3D-NEE suggests the operativity of a catalytic effect on this process, related to the fact that the Au-nanowires, which compose the NEE, present indeed a subnanomorphology made of merging gold nanoparticles. It is indeed known that gold nanoparticles are good electrocatalyst for nitrate reduction.

On the basis of these preliminary results, a series of experiments was performed in order to study the effect of the applied potential and of the zinc salt precursor on the morphology of the deposit formed. To this aim, two different potentials, namely -0.550 V and -0.700 V, were applied to the electrodes dipped in 5 mM HMTA and alternatively 5 mM $\text{Zn}(\text{NO}_3)_2$ or ZnCl_2 . The influence of the oxygen concentration was studied performing the deposition in air, in nitrogen purged and in oxygen saturated solution. Following previous reports [12], HMTA was added as nucleation control agent; it was demonstrated that HMTA releases hydroxyl ions and acts as organic soft template at high temperature in aqueous solution [16].

Figure 3.3 reports the comparison between the chronoamperograms recorded when a constant potential of -0.550 V was applied at an ITO. The electrodes used in these experiments were labeled as described in section 2.5: ITO550NO3N2 (blue line), ITO550Cl2N2 (green line), ITO550NO3Ai (red line), ITO550Cl2Ai (black line), ITO550NO3O2 (cyan line), ITO550Cl2O2 (fuchsia line). The curve recorded in nitrogen purged solutions, both using $\text{Zn}(\text{NO}_3)_2$ and ZnCl_2 , does not show any cathodic current, while at ITO550Cl2Ai and at ITO550NO3Ai a constant current of about $10 \mu\text{A cm}^{-2}$ was detected. In O_2 saturated solution the current is almost three times higher for both ITO550NO3O2 and ITO550Cl2O2, but in the former case the current increases with time, suggesting an increase in the surface area, while in the latter case the current decreases. This behavior could be due to Cl^- adsorption on the surface of the deposited ZnO, limiting the O_2 reduction. These evidences confirm that at -0.550 V on ITO oxygen reduction occurs.

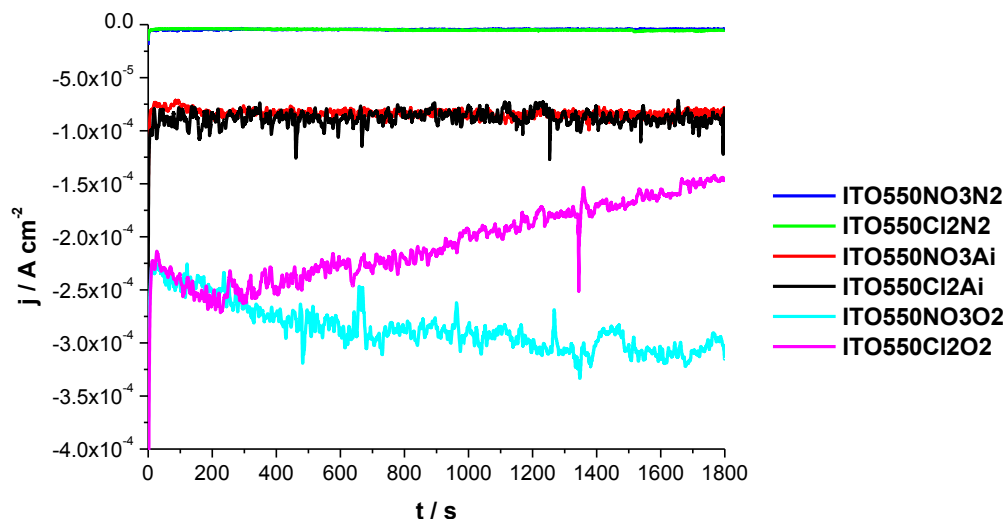


Figure 3.3. Chronoamperograms of ZnO depositions on ITO electrodes, performed both 5 mM $\text{Zn}(\text{NO}_3)_2$ or ZnCl_2 , in the presence of air, in nitrogen purged or in oxygen saturated solution. Constant potential bias -0.550 V at 85°C .

With regard to 3D-NEE electrodes (Figure 3.4), again the cathodic current for NEE550Cl2N2 is negligible, slightly increases in NEE550Cl2Ai and is threefold in NEE550Cl2O2, confirming that at this potential oxygen is reduced at 3D-NEEs.

On the other hand, when $\text{Zn}(\text{NO}_3)_2$ is used as ZnO precursor, a cathodic current is also visible in the nitrogen purged solution (i.e. NEE550NO3N2), confirming that the nitrate reduction is anticipated on this substrate. When the deposition is conducted in air the cathodic current is slightly increased at the beginning of the experiment, suggesting that both the reduction of nitrate and dissolved O_2 occur. In fact at higher O_2 concentration (i.e. NEE550NO3O2) the cathodic current is twofold. It is worth pointing out that the progressive current increase agrees with a progressive increase of the surface area with deposition time. Finally, the achievement of a final plateau current suggests the operativity of a mass transport diffusive limitation, in agreement with previous studies performed on 3D-NEEs [23].

It can be seen that the deposition current at the 3D-NEE is significantly higher than the one recorded at the flat electrode because of the higher surface area of the former.

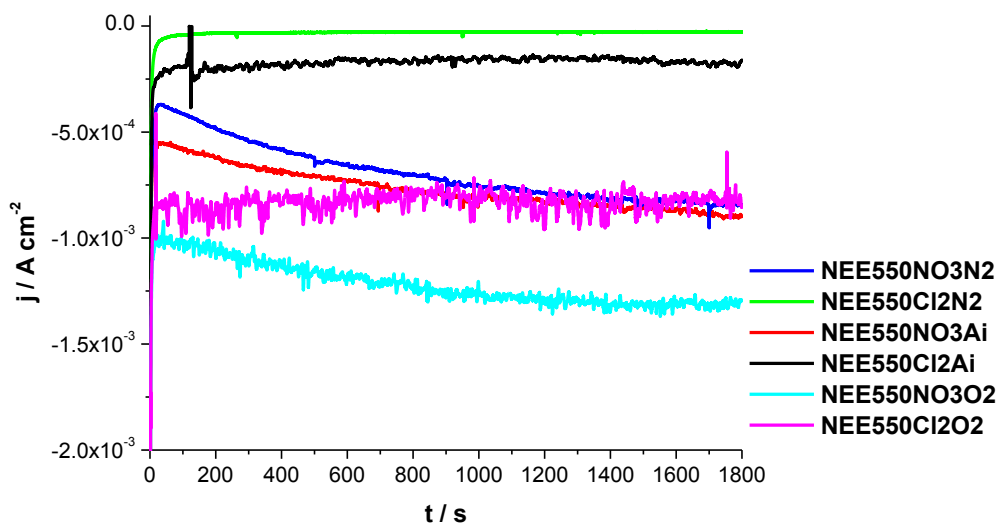


Figure 3.4. Chronoamperograms of ZnO depositions on 3D-NEE electrodes, performed both 5 mM $\text{Zn}(\text{NO}_3)_2$ or ZnCl_2 , in the presence of air, in nitrogen purged or in oxygen saturated solution. Constant potential bias -0.550 V at 85°C .

Figure 3.5 shows the chronoamperograms recorded, using ITO electrodes, with a constant potential of -0.700 V. As far as the deposition using ZnCl_2 is concerned, the cathodic current is negligible in deoxygenated solution and slightly increases in the presence of air, while a cathodic current is detected both on ITO700NO3N2 and on ITO700NO3Ai, so confirming that at such a potential, both nitrate and oxygen reduction are operative. In agreement with the possible concomitant occurrence of both reduction processes, the current at the beginning of the deposition is higher for ITO700NO3Ai. A difference correlated with the presence/absence of dissolved oxygen is that the cathodic current on ITO700NO3Ai is quite constant during the whole deposition time, while on ITO700NO3N2 the current keeps increasing, suggesting a significant increase of the active area during the reduction.

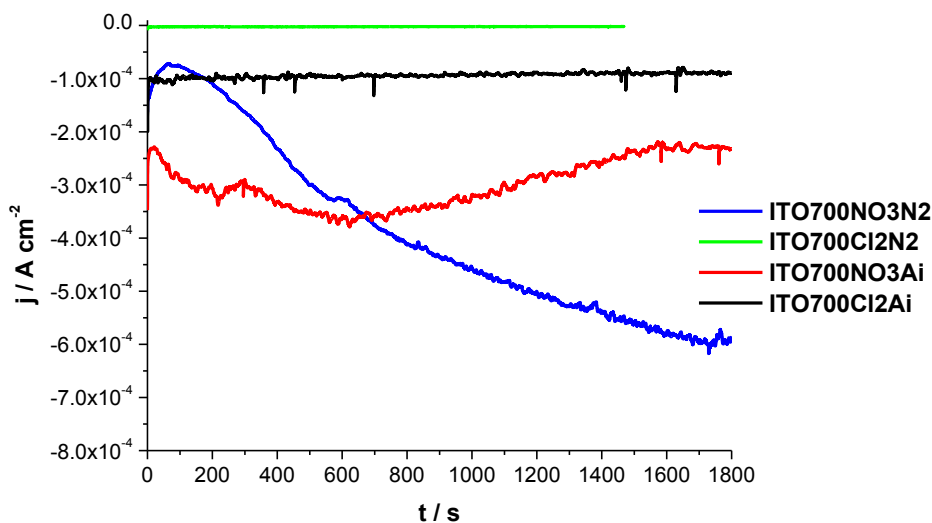


Figure 3.5. Chronoamperograms of ZnO depositions on ITO electrodes, performed in 5 mM $\text{Zn}(\text{NO}_3)_2$ or ZnCl_2 , in the presence of air or in nitrogen purged solution. Constant potential bias -0.700 V at 85°C .

Figure 3.6 reports the chronoamperograms recorded on 3D-NEE. The time transient current recorded in ZnCl_2 solution resembles very much the one recorded at -0.550 V confirming the operativity of the oxygen reduction process at potentials above -0.400 V. Instead, the chronoamperograms recorded in $\text{Zn}(\text{NO}_3)_2$ solution almost overlap, indicating that, at this potential, the presence of oxygen doesn't affect significantly the deposition process; the deposition process now appears to be controlled by the nitrate reduction reaction. For both aerated and de-aerated solutions, at the 3D-NEE, the cathodic current increases with time and achieves a plateau after 600 s, suggesting again a diffusion controlled limitation related to the operativity, at the 3D-NEE, of a total overlap diffusion regime [23].

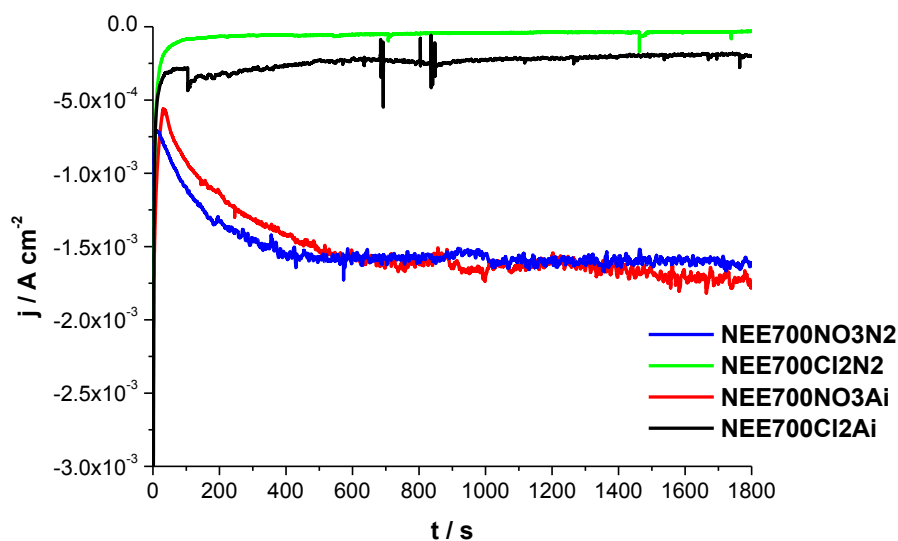


Figure 3.6. Chronoamperograms of ZnO depositions on 3D-NEE electrodes, performed in 5 mM $\text{Zn}(\text{NO}_3)_2$ or ZnCl_2 , in the presence of air or in nitrogen purged solution. Constant potential bias -0.700 V at 85°C .

Morphological and structural characterization

The morphological characterization of the different nanostructures obtained from the electrochemical depositions of Figures 3.3, 3.4, 3.5 and 3.6 was performed by SEM and FEG-ESEM analyses. Relevant images, reported in Figures 3.7, 3.8, 3.9 and 3.10, indicate that at both ITO and 3D-NEE, nanowires and nanorods are formed, however with different geometries and morphologies which depend on the experimental conditions adopted, (i.e. applied potential, zinc oxide precursor and oxygen concentration).

As far as the ITO550 series is concerned (Figure 3.7), as expected on the basis of the relevant chronoamperogram in Figure 3.3, no deposit is visible for ITO550NO3N2 and ITO550Cl2N2. For all the other deposition conditions, NWs with randomly distributed orientation were grown. Note that, for this series, the morphology of the NWs is mainly influenced by the oxygen concentration, in fact both ITO550NO3Ai and ITO550Cl2Ai present low density ZnO fibers with diameter of 200-300 nm while ITO550NO3O2 and ITO550Cl2O2 present nanofibers 90 nm in diameter.

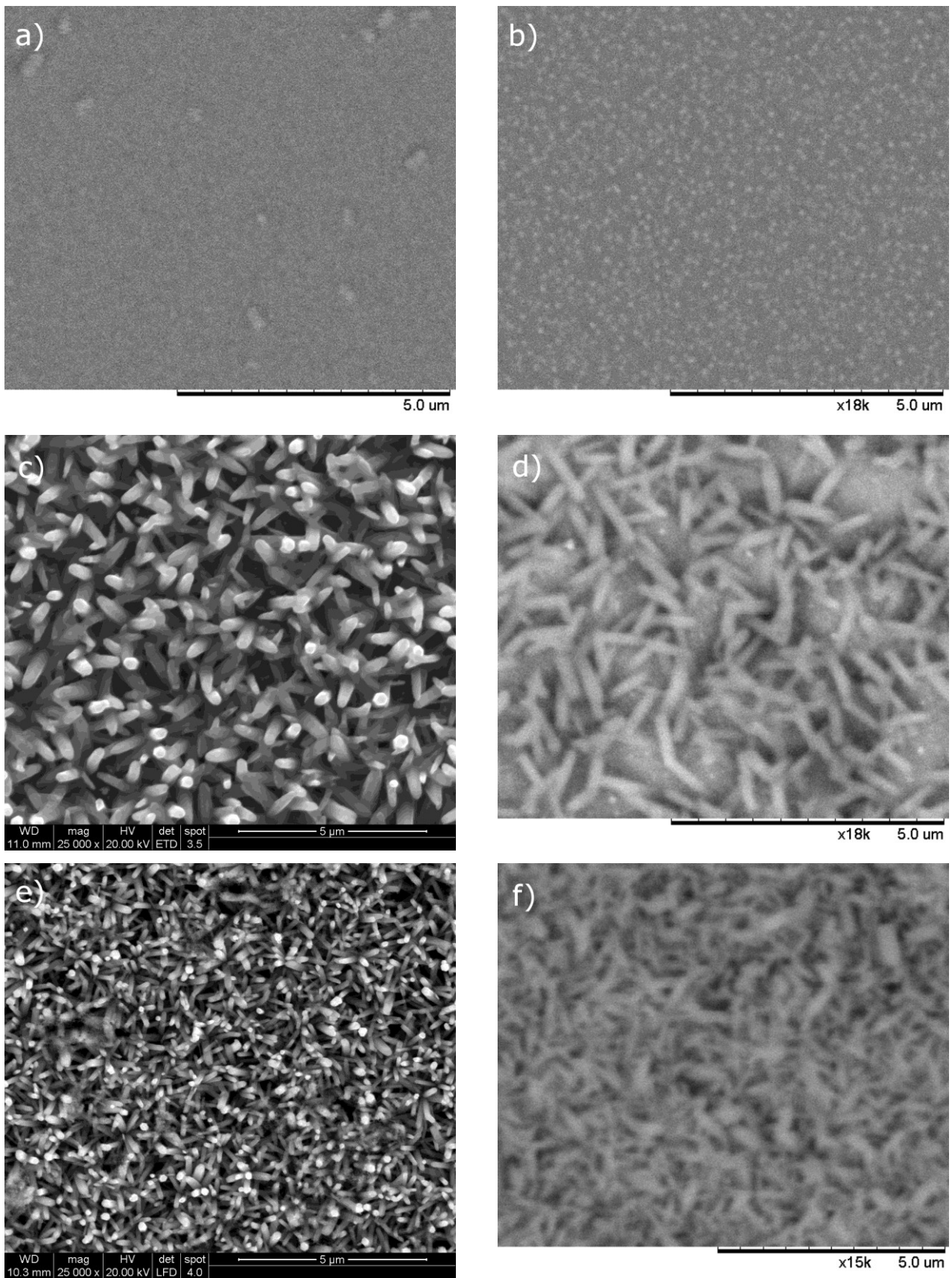


Figure 3.7. FEG-ESEM images of ITO electrodes after 30 min ZnO electrodeposition using a potential of -0.550 V: ITO550NO3N2 a), ITO550Cl2N2 b), ITO550NO3Ai c), ITO550Cl2Ai d) ITO550NO3O2 e) ITO550Cl2O2 f).

Linear and Hierarchically Branched ZnO Nanofibers

In Figure 3.8 SEM characterization of the ITO700 series is reported. As expected from the chronoamperogram, in absence of oxygen and NO_3^- in the solution (ITO700Cl2N2), no deposits are present at such a potential, while the nanofibers obtained at ITO700Cl2Ai are pretty much alike the one obtained at -0.550 V, stating that the applied potential doesn't influence the morphology of the nanofibers when ZnCl_2 is used as precursor. When $\text{Zn}(\text{NO}_3)_2$ is used, instead, the NWs obtained in deoxygenated solution are 200-300 nm in diameter, but when the deposition is performed in the presence of air, the diameter of the NWs is 600 nm.

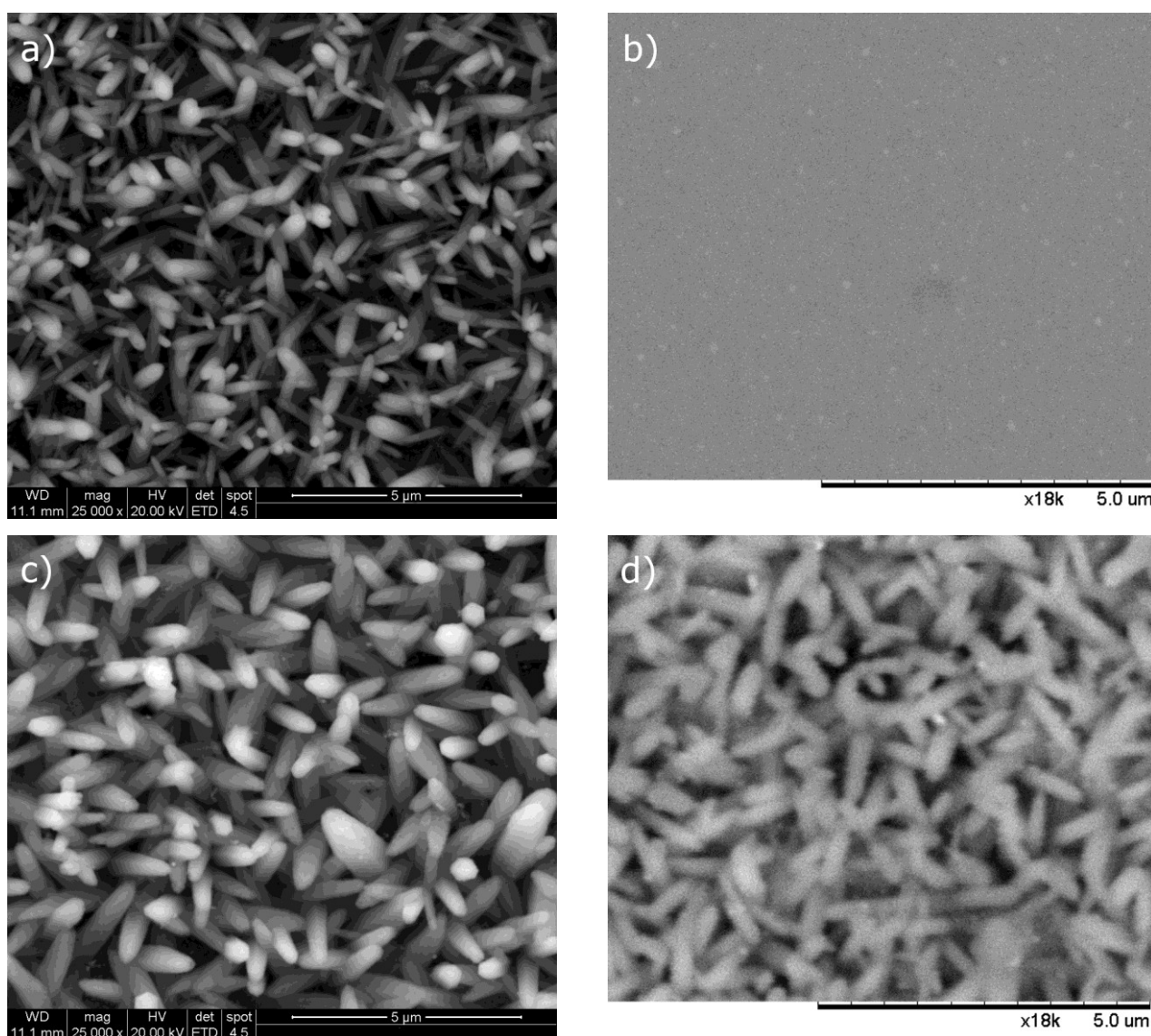


Figure 3.8. FEG-ESEM images of ITO electrodes after 30 min ZnO electrodeposition using a deposition potential of -0.700 V: ITO700NO3N2 a), ITO700Cl2N2 b), ITO700NO3Ai c), ITO700Cl2Ai d).

These results are apparently in contrast with the model presented very recently by Khajavi et al. [31], which states that an higher deposition current (and, consequently, an higher pH at the electrode surface), leads to thinner ZnO nanorods. Actually, it must be stressed that in our synthetic route the electrodes were not pre-covered by a ZnO seed layer deposited by spray pyrolysis, as done in ref. [31]. Elias et al. [32] demonstrated indeed that the presence of such a layer (named “buffer layer”) plays an important role in the nucleation process in the first steps of the deposition. These evidences indicate that in the absence of nanocrystals previously deposited on the substrate (buffer layer), the cathodic current density in the first minutes of the deposition is crucial in defining the morphology of the NWs, since a higher current means larger ZnO crystallites and, subsequently, thicker fibers.

In Figure 3.9, the SEM images of the 3D-NEEs used for the ZnO depositions at -0.550 V, are reported. Yet again, no deposits are visible in absence of dissolved oxygen or NO_3^- . In all the other cases, ZnO NWs grow directly on the gold nanowires which constitute the backbone for a hierarchically branched architecture. Note that the NWs grown from $\text{Zn}(\text{NO}_3)_2$ precursor are much denser with regard to the one obtained from ZnCl_2 solutions. For both ZnO precursors, the diameter and the length of the needles grow with the increase of the oxygen concentration, being 50-60 nm in diameter and 500 nm in length for the smallest (NEE550Cl2Ai) and nearly 200 nm in diameter and 1 μm in length for the biggest (NEE550NO3O2). This is in accordance with a higher charge measured from the chronoamperometric curve. The ZnO needles have a significantly smaller diameter than NWs grown on flat ITO electrodes, operating under the same deposition conditions. Such a difference in morphology can be explained by a constrain effect, in which the lateral growth of the metal oxide is limited by the gold nanowires diameter and density. Beyond geometrical effects, one of the reason leading to higher aspect ratio ZnO rods on 3D-NEE substrate, can be related also to the fact that the gold nanowires are made of merged gold nanoparticles [27]. It was indeed demonstrated that gold nanoparticles play a catalytic effect on ZnO growth and on the morphology and orientation of ZnO nanofibres [33], leading to thinner, longer and more parallel aligned nanorods than on other substrates. Note that, with respect to the ZnO nanobranches on ZnO NWs described by Baxter & Aydil [34], our ZnO subnanostructures are approximately 10 times longer, with only 3 times higher diameter.

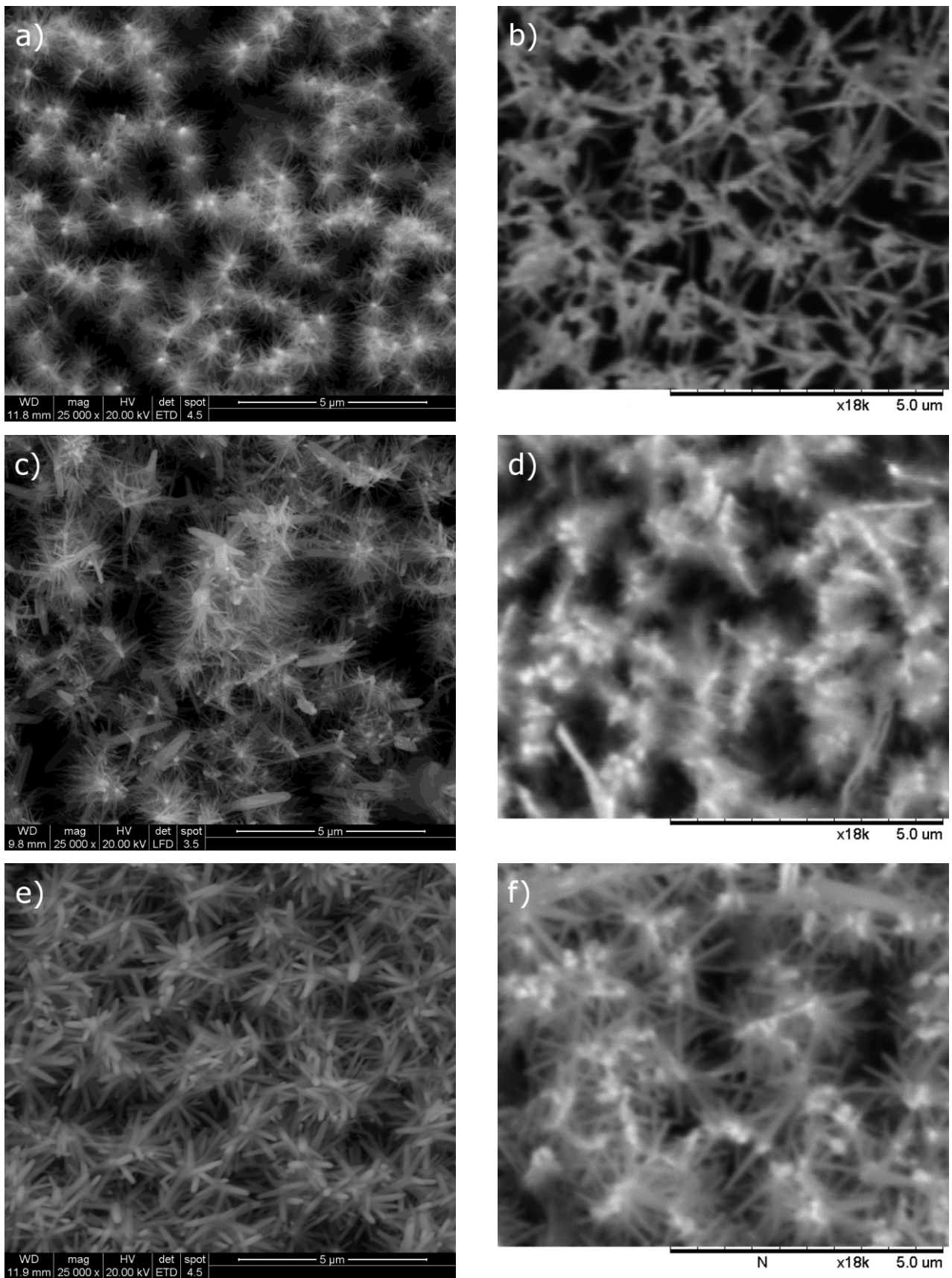


Figure 3.9. FEG-ESEM images of 3D-NEE electrodes after 30 min ZnO electrodeposition using a deposition potential of -0.550 V: NEE550NO3N2 a), NEE550Cl2N2 b), NEE550NO3Ai c), NEE550Cl2Ai d) NEE550NO3O2 e) NEE550Cl2O2 f).

Linear and Hierarchically Branched ZnO Nanofibers

The SEM pictures referring to NEE700NO3N2 and NEE700NO3Ai show overgrown NWs without a defined morphology (Figure 3.10). Apparently a too fast deposition leads to a disordered growth, because a too high concentration of OH^- is generated on the surface of the electrode, so disrupting the hierarchical growth mechanism. NEE700Cl2N2, in accordance to the negligible current recorded during the deposition, shows no deposits, while NEE700Cl2Ai shows short and thin NWs growing from the gold wires, with dimensions similar to the one reported for NEE550Cl2Ai.

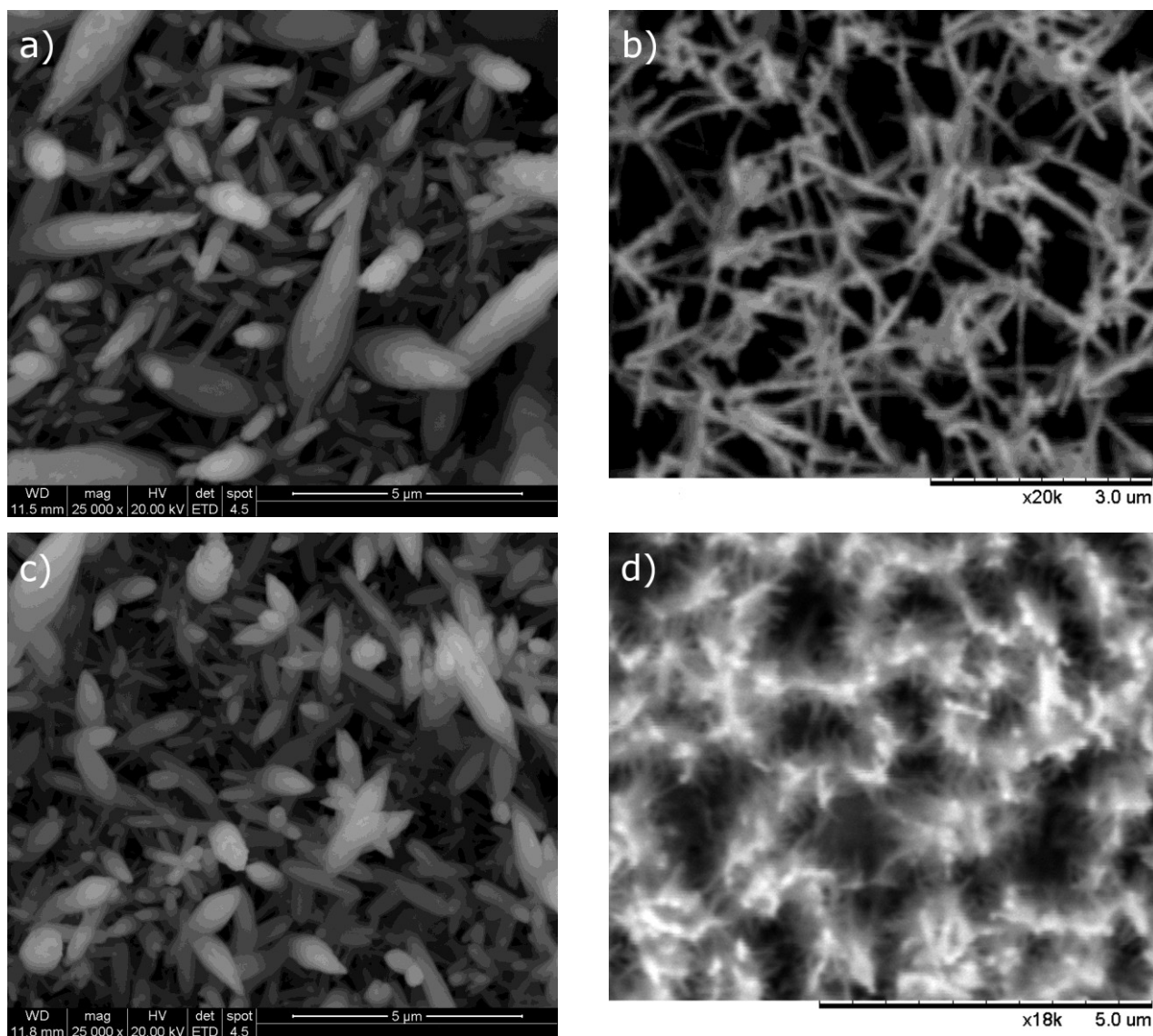


Figure 3.10. FEG-ESEM images of 3D-NEE electrodes after 30 min ZnO electrodeposition using a deposition potential of -0.700 V: NEE700NO3N2 a), NEE700Cl2N2 b), NEE700NO3Ai c), NEE700Cl2Ai d).

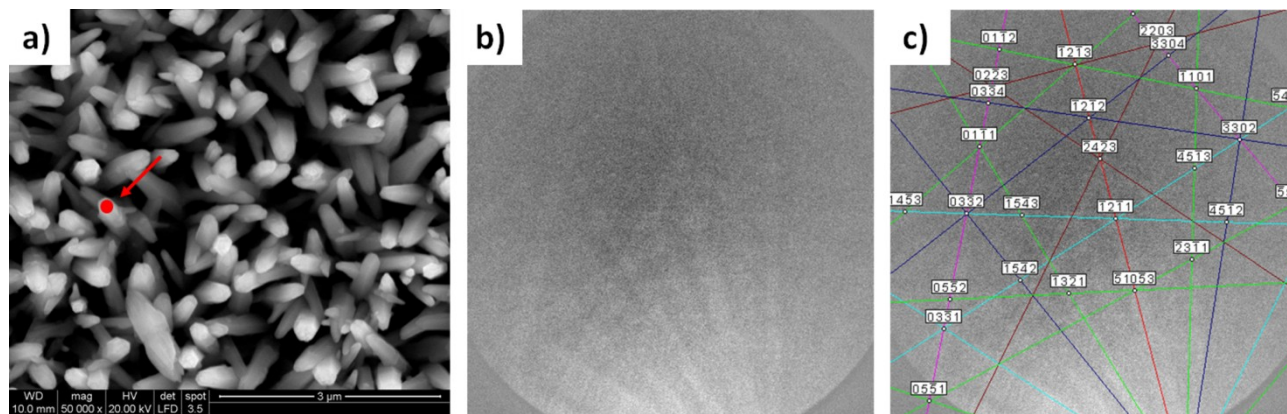
The crystalline phase identification was performed by EBSD on two representative samples for both NEE and ITO, namely ITO550NO3Ai and NEE550NO3Ai. This characterization

technique, suitable for any crystalline material, was developed in the 1980s and allows one to obtain crystallographic information such as individual grain orientations, local texture, point-to-point orientation correlations and phase identification and distributions [35].

Even if it was proved that EBSD allows phase identification of submicrometer crystalline particles [36,37] and permits to determine the crystallographic orientation of nanostructures [25, 38] there are still few applications of this technique to the characterization of nanostructures [39].

In this study the EBSD patterns were acquired in situ on ZnO NWs grown on flat ITO electrode, and on ZnO NWs grown from the gold nanowires. The fibers were sampled on different spots of the surface at their top head in order to avoid pattern shadowing by neighboring fibers; note that such an effect could occur in the present samples because their morphology is made of a very dense ensemble of fibers. The collected EBSD patterns were compared with the reference patterns calculated for the possible crystallographic phase, that, for the elemental composition of the fibers investigated, are hexagonal wurtzite structure (i.e. zincite), and cubic zinc blende structure.

The EBSD patterns collected both from ITO550NO3Ai and NEE550NO3Ai, result correctly indexed with the pattern calculated for the hexagonal wurtzite structure of zincite (Fig. 3.7 b-c, Fig. 3.8 b-c).



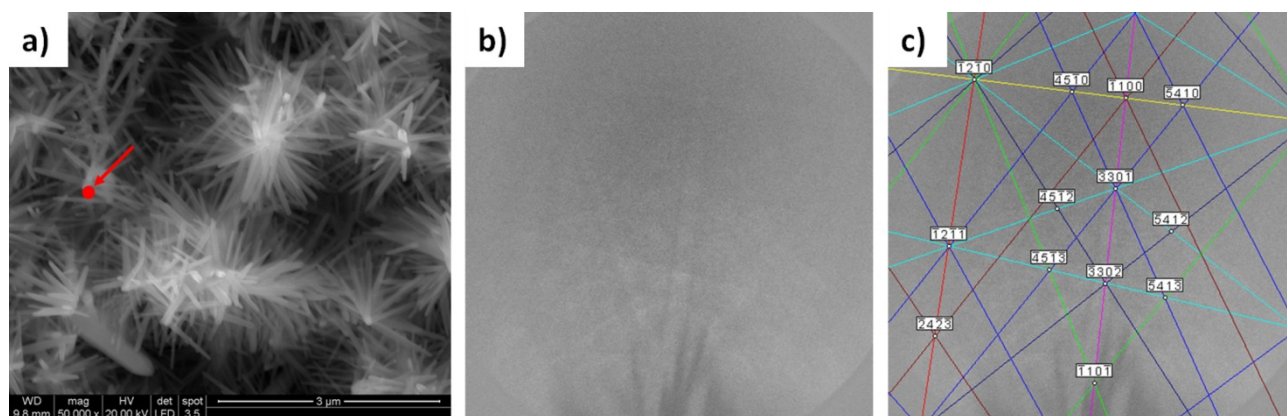


Figure 3.12. (a) FEG-ESEM secondary electron image NEE550NO3Ai. (b) EBSD pattern collected from ZnO NWs on the spot marked by the •. (c) EBSD simulated pattern of hexagonal wurtzite structure overlaid on pattern of (b).

Photoelectrochemical water oxidation activity

In order to evaluate the effect of the nanostructuring of ZnO NWs on the photocatalytic properties of the material, we performed the compared photoelectrochemical characterization of ZnO NWs grown both on ITO and on 3D-NEE. To this aim we studied the photoelectrochemical oxidation of water. For the sake of clarity, only photocurrents generated at ITO550NO3Ai (dotted line) and NEE550NO3Ai (full line) are reported in Figure 3.13.

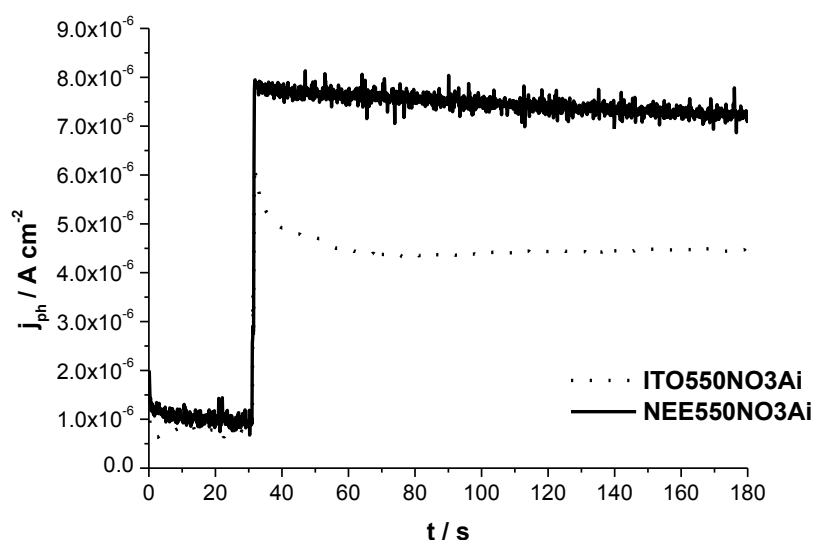


Figure 3.13. Photocurrent measured at 0.400 V vs Ag/AgCl sat. in 0.1 M phosphate buffer solution pH 7 over 180 seconds. Dotted line ITO550NO3Ai, full line NEE550NO3Ai.

Linear and Hierarchically Branched ZnO Nanofibers

The current measured under UV irradiation includes the current related to the photoelectrochemical oxidation at the semiconductor electrode plus the double layer charging current and net photocatalysed residual currents. Since also charging and residual currents scale with the surface area of the working electrode, it is necessary to evaluate the contribution of these currents, in order to extract the real photoelectrochemical contribution from the overall current. For this reason, a preemptive polarization measurements in the dark was performed (first 30 s on the plots), afterwards, the UV lights were turned on and the photocurrent was recorded. The final photocurrent values taken into account are indeed the difference between the current measured in the dark and the plateau current recorded after 140 s of irradiation. Figure 3.14 reports the photocurrent (measured as described above) for all the prepared electrodes.

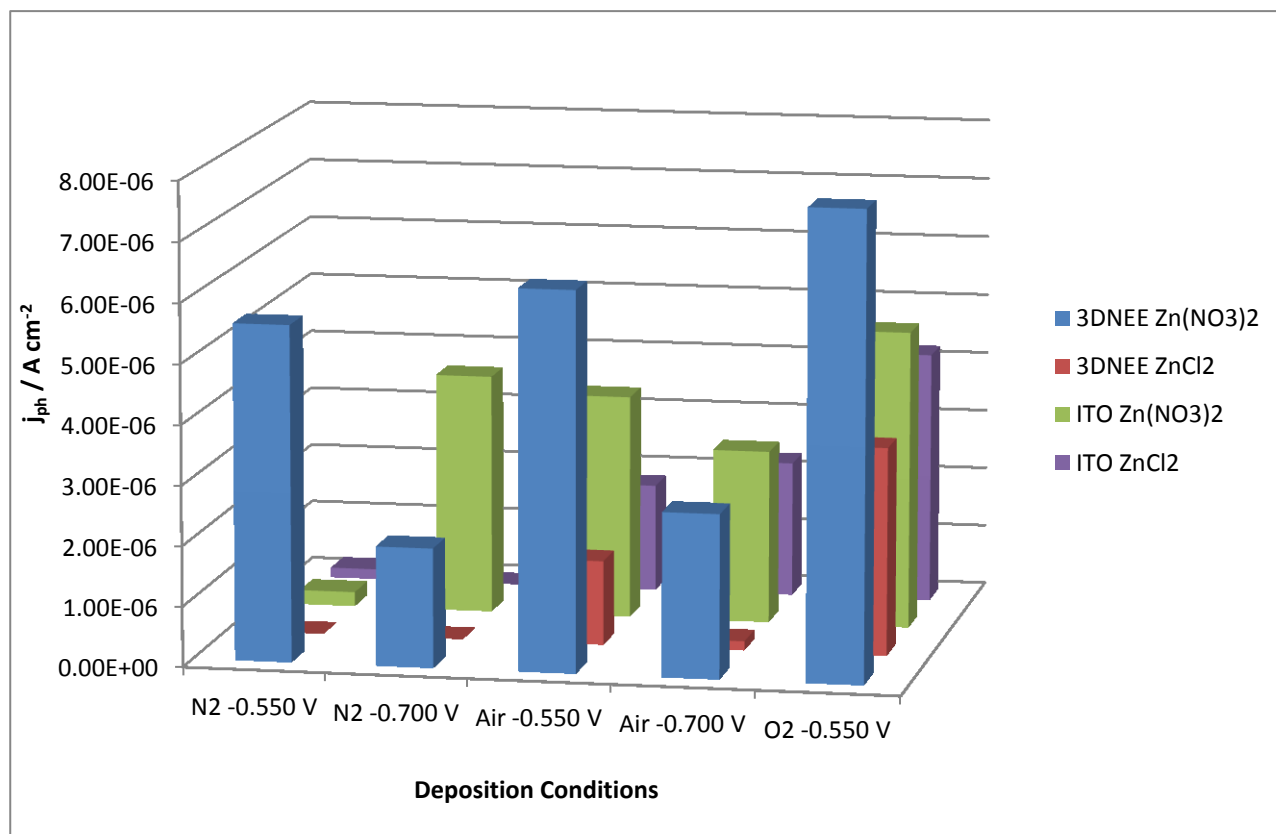


Figure 3.14. Histogram representing the photocurrent values recorded with both linear and branched nanofibres electrodes.

As expected, the electrodes characterized by a negligible deposition current (i.e. ITO550NO3N2, ITO550Cl2N2, NEE550Cl2N2, ITO700Cl2N2, NEE700Cl2N2) gave extremely low photocurrents, confirming that almost no ZnO has been deposited. ITO700NO3N2 and ITO550NO3Ai achieved comparable photocurrents, namely $4.00 \mu\text{A cm}^{-2}$, $3.73 \mu\text{A cm}^{-2}$

Linear and Hierarchically Branched ZnO Nanofibers

respectively; ITO700NO3Ai ITO700Cl2Ai and ITO550Cl2Ai gave photocurrents of $2.89 \mu\text{A cm}^{-2}$, $2.27 \mu\text{A cm}^{-2}$ and $1.80 \mu\text{A cm}^{-2}$. The higher photocurrent at ITO700NO3N2, ITO550NO3Ai can be related to their higher surface area, since they showed thinner and more dense ZnO NWs. The best result among linear ZnO NWs electrodes were achieved by ITO550NO3O2 and ITO550Cl2O2, where the fibers were even thinner and denser being as small as 90 nm in diameter. We can conclude that the NWs diameter and density is a key parameter in determining the efficiency of 1D nanostructured photoelectrodes.

As far as branched NWs electrodes are concerned, NEE550Cl2N2 and NEE700Cl2N2, where the deposition current approached zero, and no deposits were observed, the photocurrent is negligible. NEE550NO3N2 and NEE550NO3Ai achieved comparable photocurrents which are double in comparison with the homologous electrodes deposited at -0.700 V, even if the total charge involved in the electrodeposition of the former is lower. This confirms that the morphology of the nanostructured materials is extremely important in defining its physico-chemical properties. Note that, in any case the deposits obtained using ZnCl_2 precursor gave rise to lower photocurrent. Again the best photocurrent value, among the branched NWs electrodes, was obtained using $\text{Zn}(\text{NO}_3)_2$ precursor in oxygen saturated solution at a potential of -0.550 V.

If we compare the photocurrent achieved by the best linear and branched ZnO NWs electrodes with TiO_2 nanoparticles (NP) and NWs electrodes (see table 3.1) it is evident that ZnO based electrodes achieved photocurrent values one order of magnitude higher than the TiO_2 electrodes. This results confirm that, NWs morphology can really overtake the performances of NP film electrodes, but only when the orientation of the nanofibers allows a direct path from the tips of the nanofibers to the electrode substrate.

TiO_2 NW	TiO_2 NP	Linear ZnO NW	Branched ZnO NW
0.528	0.946	4.98	7.76

Table 3.1. Photocurrent (expressed in $\mu\text{A cm}^{-2}$) achieved by different nanostructured photoelectrodes.

On the other hand, it's important to note that the most efficient branched electrode, namely NEE550NO3O2, provides a photocurrent which is 50% higher than the best ITO electrode, (ITO550NO3O2). These results confirm that branched nanostructures improve significantly the photocatalytic performances, the overall effect being the result of a positive combination of improved electron transport efficiency and increased surface area.

The electrodes stability has been studied extending the photoelectrochemical experiments up to 120 min. Only NEE550NO3Ai and ITO550NO3Ai electrodes were taken into account as representative for both structures i.e. branched and linear nanofibres, respectively (Fig. 3.15).

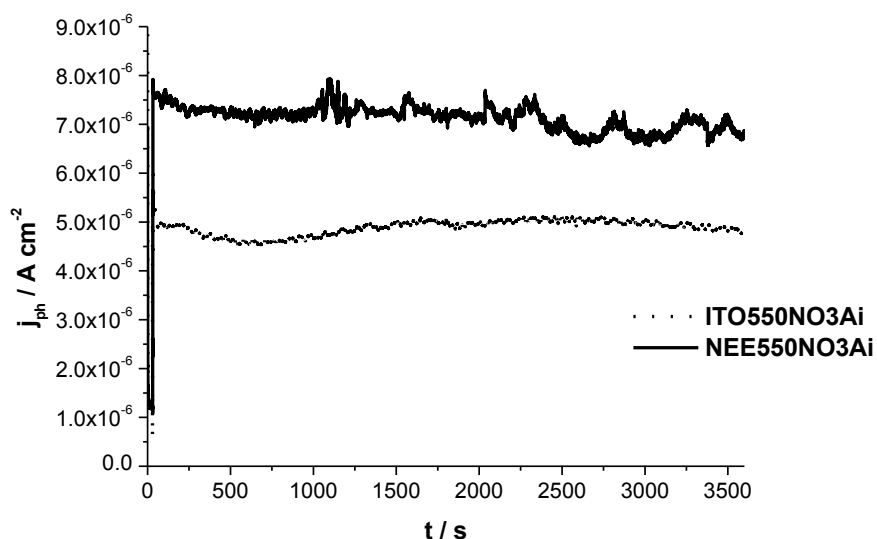


Figure 3.15. Photocurrent stability measured at 0.400 V vs Ag/AgCl sat. in 0.1 M phosphate buffer solution pH 7 over 2 hours. Dotted line ITO550NO3Ai, full line NEE550NO3Ai.

ITO550NO3Ai shows a quite stable signal over time (after two hours the photocurrent is 99% of the initial one), while with NEE550NO3Ai the photocurrent recorded after two hours decreases of approximately 6-7 %. SEM observations performed after the prolonged photoelectrochemical tests did not show any detectable change in the structure of both electrodes. These evidences indicate that the slight decrease in photocurrent with time observed with the branched NEE is due more probably to the entrapment of small oxygen bubbles within the intricate structure of ZnO nanoneedles rather than to photochemical degradation of the ZnO nanofibers. Note that, in any case, the photocurrent density at the branched NEE is always significantly higher than that generated by the linear nanofibers on ITO. Further investigations on the role of gas evolution are presently in progress, looking on one side to the possibility to avoid or minimize the effect of gas entrapment and, on the other, by studying the use of the branched nanofibers for catalyzing photoelectrochemical reactions which do not generate gas.

3.4 Conclusions

This is the first time that ZnO branched nanostructures are obtained by a relatively simple combination of wet-chemistry methods, (which include the chemical growth of substrate NWs, in this case Au in nanoporous templating membranes) combined with the electrochemical growth of ZnO sub-nanostructures. Notwithstanding its easiness, the method shows to be effective in improving the photoelectrochemical performances of the hierarchically branched nanoelectrodes, indicating interesting prospects for their photoelectrochemical application. Interestingly, 3D-NEE showed improved catalytic properties both on the electrochemical reactions involved in the deposition and for the controlled growth of the ZnO NWs substructures. Finally, we demonstrated that EBSD constitutes a new efficient analytical tool for phase identification analysis of complex nanostructures such as the hierarchical ZnO nanostructures prepared here. The obtained results support the application of this technique as a valuable alternative to XRD analysis, with the great advantage of obtaining precise structural information on individual nanostructures.

References

- [1] M. H. Huang, S. Mao, H. Feick, H. Yan, Y. Wu, H. Kind, E. Weber, R. Russo, P. Yang, *Science* **292** (2001) 1897
- [2] Q. Zhang, C. S. Dandeneau, X. Zhou, G. Cao, *Adv. Mater.* **21** (2009) 1
- [3] L. E. Greene, M. Law, D. H. Tan, M. Montano, J. Goldberger, G. Somorjai, P. Yang, *Nano Lett.* **5** (2005) 1231
- [4] C. Ma, D. Moore, Y. Ding, J. Li, Z. L. Wang, *Int. J. Nanotechnol.* **1** (2004) 431
- [5] P. X. Gao, Z. L. Wang, *Small* **1** (2005) 945
- [6] Z. Peng, G. Dai, P. Chen, Q. Zhang, Q. Wan, B. Zou, *Mater. Lett.* **64** (2010) 898
- [7] G. Centi, S. Perathoner, *Eur. J. Inorg. Chem.* **26** (2009) 3851
- [8] S. P. Albu, H. Tsuchiya, S. Fujimoto, P. Schmuki, *Eur. J. Inorg. Chem.* **27** (2010) 4351
- [9] K. Shankar, J. I. Bashan, N. K. Allam, O. K. Varghese, G. K. Mor, X. Feng, M. Paulose, J. A. Seabold, K.-S. Choi, C. A. Grimes, *J. Phys. Chem. C* **113** (2005) 6327
- [10] G. Shen, Y. Bando, C.-J. Lee, *J. Phys. Chem. B* **109** (2005) 10779
- [11] J. Elias, R. Tena-Zaera, C. Lévy-Clément, *J. Electroanal. Chem.* **621** (2008) 171
- [12] J. Cui, J. Gibson, *J. Phys. Chem. B* **109** (2005) 22074
- [13] F. J. Sheini, I. S. Mulla, D. S. Joag, M. A. More, *Thin Solid Films* **517** (2009) 6605
- [14] B. Canava, D. Lincot, *J. Appl. Electrochem.* **30** (2000) 711
- [15] A. Goux, T. Pauporté, J. Chivot, D. Lincot, *Electrochim. Acta* **50** (2005) 2239
- [16] F. Xu, Y. Lu, Y. Xie, Y. Liu, *J. Solid State Electr.* **14** (2010) 63
- [17] L. Xu, Q. Chen, D. Xu, *J. Phys. Chem. C* **111** (2007) 11560
- [18] X.-J. Wu, F. Zhu, C. Mu, Y. Liang, L. Xu, Q. Chen, R. Chen, D. Xu, *Coordin. Chem. Rev.* **254** (2010) 1135
- [19] J. Elias, C. Lévy-Clément, M. Bechelany, J. Michler, G.-Y. Wang, Z. Wang, L. Philippe, *Adv. Mater.* **22** (2010) 1607
- [20] V. P. Menon, C. R. Martin, *Anal. Chem.* **67** (1995) 1920
- [21] P. Ugo, L. M. Moretto, in: C. Zoski (Eds.) *Handbook of Electrochemistry* (2007) Elsevier, Amsterdam
- [22] S. Yu, J. Wharton, N. Li, C. R. Martin, *Nano Lett.* **3** (2003) 815
- [23] M. De Leo, A. Kuhn, P. Ugo, *Electroanal.* **19** (2007) 227
- [24] K. Z. Baba-Kishi, *J. Mater. Sci.* **37** (2002) 1715
- [25] A. Gambirasi, S. Cattarin, M. Musiani, L. Vázquez-Gómez, E. Velato, *Electrochim. Acta* **56** (2011) 8582

- [26] B. Brunetti, P. Ugo, L. M. Moretto, C. R. Martin, *J. Electroanal. Chem.* **491** (2000) 166
- [27] M. De Leo, F. C. Pereira, L. M. Moretto, P. Scopece, S. Polizzi, P. Ugo, *Chem. Mat.* **19** (2007) 5955
- [28] P. Ugo, L. M. Moretto, F. Vezzà, *Chem. Phys. Chem.* **3** (2002) 917
- [29] P. Ugo, in: C. A. Grimes, E. C. Dickey, M. V. Pishko (Eds.), *Encyclopedia of Sensors* (2005) American Scientific Publishers, Stevenson Ranch
- [30] M. De Leo, F. C. Pereira, L. M. Moretto, P. Scopece, S. Polizzi, P. Ugo, *Chem. Mater.* **19** (2007) 5955
- [31] M. R. Khajavi, D. J. Blackwood, G. Cabanero, R. Tena-Zaera, *Electrochim. Acta* **69** (2012) 181
- [32] J. Elias, R. Tena-Zaera, C. Lévi-Clément, *Thin Solid Films* **515** (2007) 8553
- [33] D. Ito, M. L. Jespersen, J. E. Hutchinson, *ACS Nano* **2** (2008) 2001
- [34] J. B. Baxter, E. S. Aydil, *Appl. Phys. Lett.* **86** (2005) 053114
- [35] A. R. Schwarzer, D. P. Field, B. L. Adams, M. Kumar, A. J. Schwartz, in: A. J. Schwartz, M. Kumar, B. L. Adams, D. P. Field (Eds.) *Electron Backscatter Diffraction in Materials Science* (2009) Springer, Berlin
- [36] J. A. Small, J. R. Michael, *J. Microsc.-Oxford* **201** (2001) 59
- [37] J. A. Small, J. R. Michael, D. S. Bright, *J. Microsc.-Oxford* **206** (2002) 170
- [38] J. P. Long, B. S. Simpkins, D. J. Rowenhorst, P. E. Pehrsson, *Nano Lett.* **7** (2007) 831
- [39] Y. N. Picard, L. Mazeina, S. Maximenko, J. A. Freitas, S. M. Prokes, M. E. Twigg, *Microsc. Microanal.* **15** (2009) 402

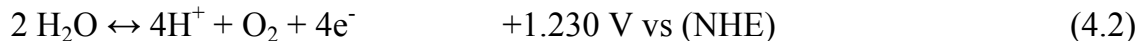
4. Asymmetrical Modification of Micro and Nanofibers by Bipolar Electrochemistry

4.1 Introduction to Bipolar Electrochemistry

Bipolar electrochemistry (BPE) occurs when an electric field induces a polarization, ΔV , on an isolated substrate (i.e. not connected to the power source) [1-3]. If such polarization is strong enough, electrochemical reactions at the opposite sides of the substrate are triggered. As a first approximation, the magnitude of ΔV must equal the difference between the standard potentials (E^0) of the two redox reactions. For example, if we want to functionalize asymmetrically a substrate with silver particles, the standard potential of Ag^{I} :



and of water oxidation, at the opposite side, have to be considered:



it follows that in this case the electric field has to generate a minimum potential difference of approximately 0.430 V.

The substrate can be any kind of conducting material. Bipolar electrochemistry does not differ from conventional electrochemistry and in principle all kind of electrochemical processes can be achieved by this technique. Literature descriptions of the various configurations that give rise to bipolar electrochemistry can be categorized into two arbitrary designations which are: open bipolar electrochemistry (see Figure 4.1a) and closed bipolar electrochemistry (see Figure 4.1b). In closed bipolar electrochemistry the substrate forms a barrier between the electrodes and divides the electrolyte in two separate areas. In such a configuration, the electrochemical cell may be described as two capacitors in series, so that the potential across the substrate is equal to the potential applied across the feeder electrodes. The main advantage of this configuration is that electrochemical reactions will occur on the substrate at relatively low field intensities [4].

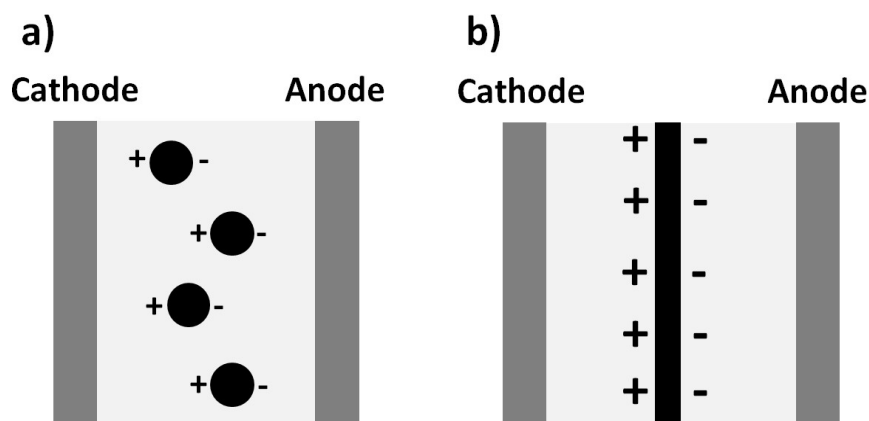


Figure 4.1. Different bipolar electrochemistry configurations. a) Example of open bipolar electrochemistry. In this case, the polarization is induced in conductive particles by an electrical field generated from the two feeding electrodes. b) Example of closed bipolar electrochemistry. The polarization is induced across a substrate by an external electric field, however, in this case, the substrate forms a barrier between the electrodes and separates the electrolyte into two areas.

In contrast, in open bipolar electrochemistry, the substrate is completely immersed in the electrolyte and the overall current, i_{s1} , flows through the solution via the migration of charged species. However in the vicinity of the substrate, the overall current will be divided into two fractions, since a fraction of the current will flow through the conducting object, i_p , and a fraction, i_{s2} , will flow through the solution [5]. Consequently, it is possible to write the following equation:

$$i_p = i_{s1} - i_{s2} \quad (4.3)$$

It follows that the ratio i_p/i_{s2} is correlated with the respective resistance of the object, R_p , and of the solution R_s [6]. Therefore, it is convenient to work with a highly resistive solution and with a highly conductive object. By this way, almost all the current passing through the system will flow through the conducting object. Moreover, in the open configuration, there is a size dependent relationship between the applied field and the onset of bipolar electrochemistry. The potential across an isolated spherical substrate (ΔV), is related to the applied electrical field (E) and the radius, r , by equation [1, 7]:

$$\Delta V = E 2r \quad (4.4)$$

This equation has been confirmed empirically by Goodridge et al. [2]. This simple relationship between the applied electric field and the potential across the substrate illustrates the need for large electric fields on spherical substrates with small radii. Since this minimum value depends upon the size of the substrate [2, 8], when particles in the range of μm or nm are used, the

electric field to be applied is large. Note that when an anisotropic particle, such as a nanowire, is used, the polarization also induces the particles to orientate in the electric field (the longitudinal axis is parallel to field lines). This means that no precautions have to be taken in order to insure their orientation during the BPE experiment. Note also that, in equation 4.4, for a wire, the length l substitutes $2r$. For example a nanowire 500 nm long, needs an applied electrical field at 10 kV cm^{-1} to produce a 0.500 V potential difference across the particle.

In closed bipolar electrochemistry, there is no such a dimension relationship, making this configuration more efficient. Nevertheless, in this configuration, the functionalization of micro and nanoparticles, would require the use of matrix for imbedding the particles and separating the two compartments of the cell. This makes the preparation of large quantities rather difficult because the modification occurs in a two-dimensional reaction space. The possibility to disperse the nanoparticles in the electrolyte solution, makes the open configuration a truly three-dimensional technique, allowing a scale-up of the production of asymmetric particles [9].

For example, very recently, Kuhn and coworkers [9-11] developed a technique for the asymmetrical modification of multiwall carbon nanotubes (MWCNT) based on a capillary electrophoresis equipment, called capillary-assisted bipolar electrodeposition (CABED). Basically, an anodic and cathodic compartment containing Pt electrodes are connected by a fused silica capillary. In the anodic side, MWCNT are suspended in the electrolyte solution of the metal salt to be deposited. The application of an intense electric field generates an electroosmotic flow inside the capillary, inducing the transport of the MWCNTs towards the cathodic compartment. The electric field also triggers the electrochemical reaction on the tips of the nanotubes: in the positively polarized side water is oxidized, on the negative side instead the metal reduction takes place. Transmission electron microscopy (TEM) characterization allowed to identify deposits with size in the order of 10 nm which increased with the length of the MWCNT, confirming that the deposits are due to bipolar electrochemistry (indeed a long tube experiences a higher V than a short one).

Semiconductor-Metal Janus particle for self sustaining water-splitting system

The goal of this chapter is to study the possible modification, in an asymmetric fashion, of semiconductor microfibers by using BPE. Such materials are particularly interesting because they can be applied for preparing novel micro-electromechanical systems (MEMS) [12], for energy conversion purposes, but also for environmental decontamination. The modification of semiconductor particles with suitable metals would allow one to combine the light harvesting properties of semiconductors with the catalytic activity of metals. Moreover, adding a metallic

junction to a semiconductor particle is a strategy to increase the photocatalytic yields. Indeed, the metallic part acts as an “electron sink” since the band bending resulting from the formation of the semiconductor-metal interface favors the separation of the charge carriers. A great number of charges can be located in the metal due to its larger electric double layer capacitance compared to the semiconductor and by this way the charge recombination probability is decreased [13]. Pradhan et al. [13] prepared Au–TiO₂ snowman-shaped particles with sizes around 10 nm. This system showed an increased activity for oxidative conversion of methanol into formaldehyde, compared to bare TiO₂ NPs. Au-TiO₂ snowman particles arrays were also more active for photocatalytic degradation of methylene blue (MB) compared to that of TiO₂ nanoparticles or Au–TiO₂ composite nanoparticles arrays [14]. These results suggest that semiconductor-metal particles can be used as efficient photocatalysts, and by engineering their components and morphology, photo-induced water splitting can be achieved.

In the following we will describe at first the results obtained in this study, by applying BPE to modify asymmetrically carbon microfibers, taken as model samples. Afterwards, the application of BPE to achieve similar goals, but using semiconductor microfibers (namely TiO₂), will be presented.

4.2 Experimental

Chemicals and materials

Acetonitrile (CH₃CN) was dried by distillation with phosphorus pentoxide (P₂O₅) in N₂ atmosphere. Aniline (C₆H₇N) pyrrole (C₄H₅N) and thiophene (C₄H₄S) were also distilled before use. The supporting electrolytes, lithium perchlorate (LiClO₄), were purchased by Aldrich, and dried at 50°C in vacuum. The solvent soluble gold salt, tetraethylammonium tetrachloroaurate [(TEA)AuCl₄], was synthesised as follows. An equimolar mixture of tetraethylammonium hydroxide [(TEA)OH] and tetrachloroauric acid (HAuCl₄) were vigorously stirred in a biphasic mixture of water and dichloromethane (ratio 1:1). After the yellow coloration was entirely transferred to the organic layer, the phases were separated. The solvent was removed from the organic fraction, and the resultant crystalline yellow solid was dried under vacuum, giving [(TEA)AuCl₄].

Electrochemical apparatus and devices

All the voltammetric analysis were performed using a CH 660 B potentiostat in a conventional three electrodes cell, in dried N₂ atmosphere. A glassy carbon (GC) electrode disc, 3 mm diameter, was employed as working electrode and two platinum coils were used as counter and pseudo-reference electrode. The GC electrode was mirror polished prior to each experiment with 0.3 and 0.05 μm alumina slurries on soft pads. After each experiment, a microvolume of ferrocene (Fc) solution in acetonitrile was added as an internal standard to set the potential scale. In order to do this, the cyclic voltammogram of ferrocene (Fc) / ferrocinium (Fc⁺) couple was recorded at 50 mV s⁻¹ ($\Delta E_p = 60$ mV) and its E_{1/2} value was determined as $\frac{E_{pf} + E_{pb}}{2}$ [15]. The E_{1/2} resulted centered at 0.040 V with respect to the Pt pseudo-reference electrode. All the other potential values reported in the following are referred to the E_{1/2} of the Fc/Fc⁺ couple.

Bipolar electrochemistry apparatus and reagents

Figure 4.2 shows the custom made bipolar electrodeposition glass cell used for BPE. It is composed by one reaction compartment, with a hole in the upper side to allow UV irradiation, in which the substrates and the reagents are located. This central chamber is separated by two glass septums (thickness 3 mm, porosity G2) from the two electrode compartments. These separators are needed in order to limit the effects of the intense electric field arising on the surface of the electrodes, such as: bubble formation and convection due to ohmic heating. Using this configuration, the electric field can be imposed for a relatively long time (in the order of few minutes) without experiencing significative problems. The central compartment is filled with a suspension of microfibers, in a solution of the redox species to be deposited. The electrodes compartments were filled with solvent containing no reactants. Gold or carbon plates were used as electrodes and connected with crocodile clips to the high power supply (Ortec 456 or Heinzinger PNC 30,000), and the electric field was applied for the desired time. In the photoelectrochemical deposition experiment, the cell was irradiated with three 'TL' 20W/05 PHILIPS UV-lamps. The carbon microfibers (CMFs) (8 μm in diameter and 200-300 μm in length) were provided by Dr. Francesco Crespi (SKW).

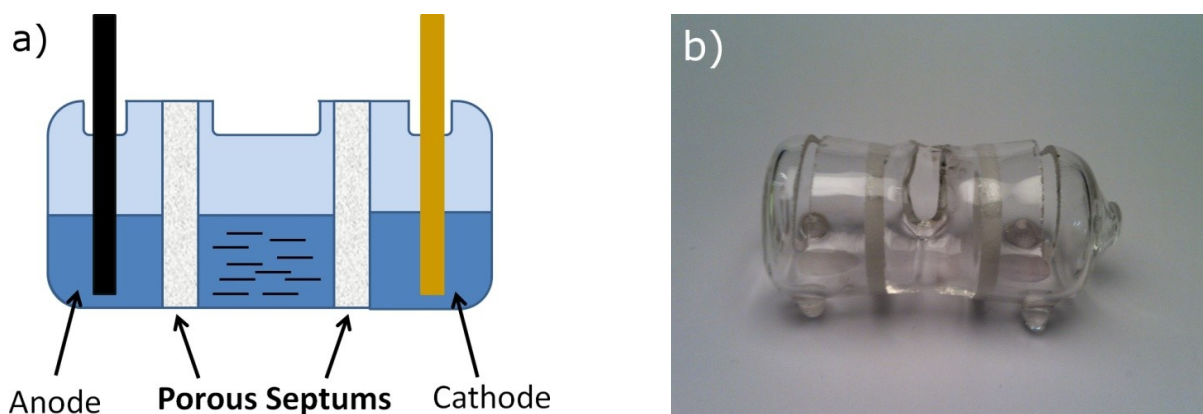


Figure 4.2. a) Schematic representation of the homemade glass cell during a BPE experiment. b) Homemade glass cell used for BPE experiments.

TiO₂ anatase electrospun nanofibers (TiO₂-NF, diameter: 150 - 400 nm, length: large distribution in the order range of hundreds of μm, see Figure 4.3) were purchased by Kertak Nanotechnology sro. The microfibers were dispersed in the solvent by sonication for 30 minutes, obtaining a dispersion of fibers with a mean length in the range of 5 - 10 μm.

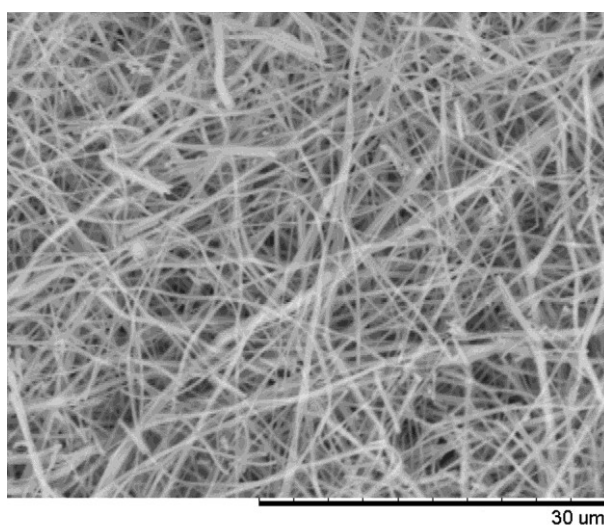


Figure 4.3. SEM image of electrospun TiO₂ nanofibers, purchase by Kertak Nanotechnology sro.

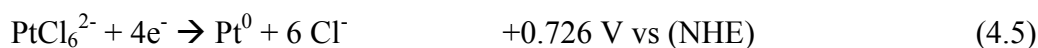
After each bipolar electrochemistry experiment, the suspension in the central compartment was filtered with a polyester nanoporous membrane (Osmonics Inc., pores diameter 200 nm), and the fibers recovered on the membrane were characterized by SEM or FEG-ESEM.

Morphological characterization

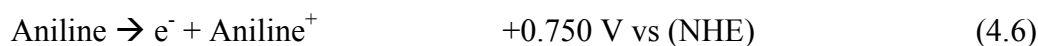
SEM and FEG-ESEM analyses were performed with a tabletop Hitachi TM3000 SEM and with a FEI Quanta FEG-ESEM, respectively. The latter was also used for the EDX characterizations.

4.3 Results and Discussion

As model to get an in depth understanding of the use of bipolar electrochemistry on quasi-1D substrates, at first we studied the asymmetrical modification of CMFs with platinum and polyaniline (PANI) in water. PANI is a conducting polymer, obtained from the oxidation of aniline, which has been studied extensively [16-22]. In order to decrease the conductivity of the solution, we suspended the fibers in a 1:2 H₂O/methanol solution. Since the experiments were conducted in hydroalcoholic solution, as an approximation, the reduction standard potential of PtCl₆²⁻ was taken into account [23]:



The aniline oxidation potential reported in the literature is [24]:



From reactions 4.5 and 4.6, follows that the outer electric field must generate a minimum potential difference of approximately 0.020 V, between the ends of each fiber. This value is rather small, so that the mixture of these two compounds were not stable at every concentration. Then, because of their intrinsic reactivity, the concentration of the metal salt and of the monomer were chosen carefully. A 3 mM (NH₄)PtCl₆ and 10 mM aniline mixture was observed to be stable for several hours, while, with higher metal concentrations, a black deposit was observed after a few minutes.

CMFs were suspended in freshly prepared solutions, and the central compartment of the cell was filled with the suspension. In order to avoid undesired water oxidation/reduction, the outer compartments (where the solution is in direct contact with the feeder electrodes) were filled with pure methanol. The modification was achieved applying a constant potential of 300 V for 5 minutes. The modified suspension in the central compartment was collected, filtered in a polyester

microfiltration membrane, and the membrane observed by SEM. Figure 4.4 shows SEM images of the functionalized carbon fibers.

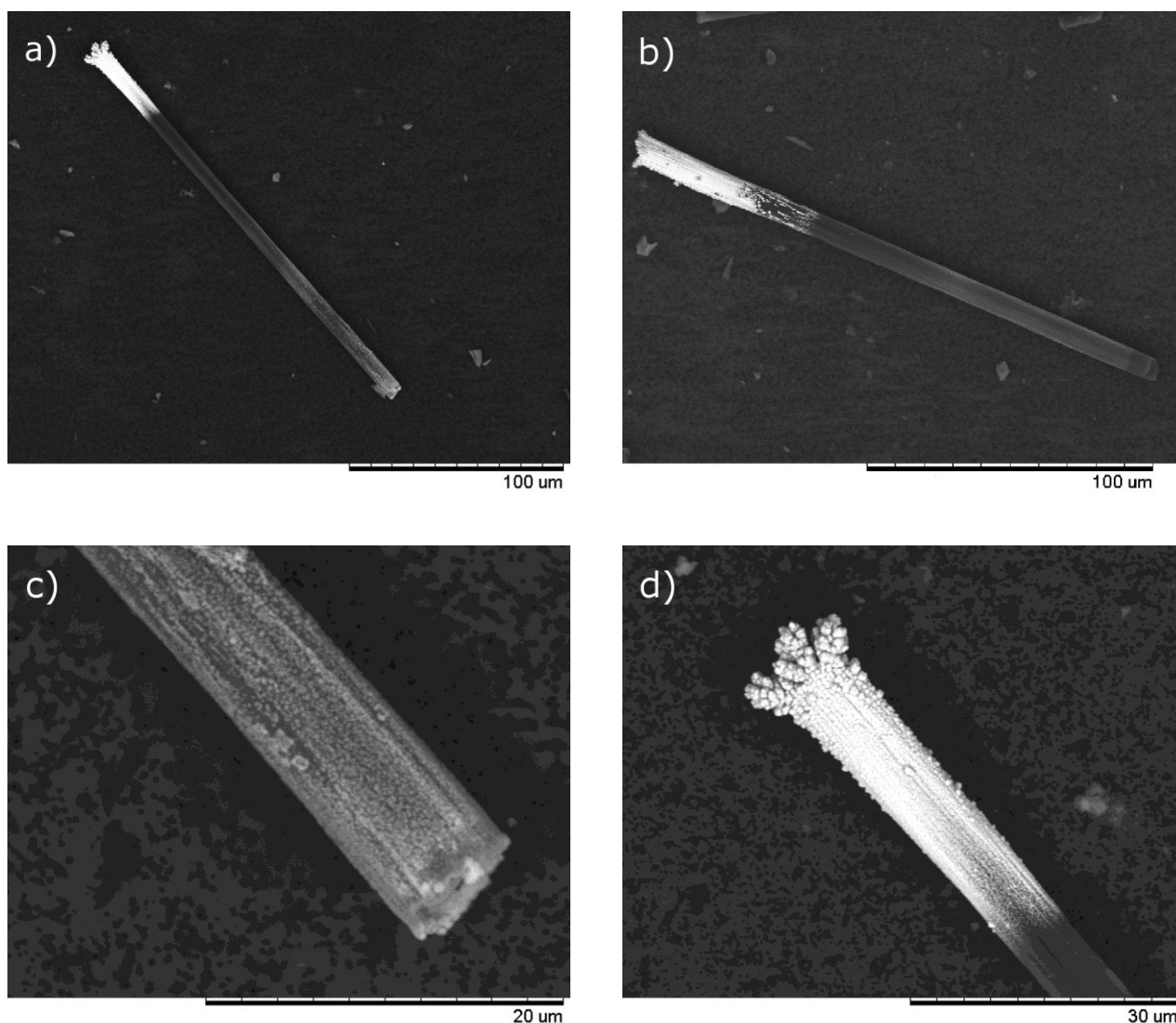


Figure 4.4. SEM pictures of CMFs modified by BPE. (a-b) Carbon fibers functionalized in asymmetrical fashion with Pt and PANI. (c) Detail of image a (PANI modified end). (d) Detail of image a (platinized end).

The fibers present a bright deposit on one side, which can be associated with the deposition of metallic platinum. In Figure 4.4d metallic dendrites, growing from the tip of the carbon fiber, are clearly visible. At the other end of the fiber, a different kind of deposit is detected, characterized by a lower contrast in the SEM image (see figure 4.4c). Microanalysis confirmed the presence of Pt on one side and N (attributed to the deposition of PANI), on the other.

Although this setup allowed us to modify micro particles, since it is based on aqueous solutions it can be used only to deposit redox couples with a relatively low potential difference. It is

indeed impossible to increase the potential difference between the feeding electrodes above 300 V due to the water conductivity, which increases i_{s1} and i_{s2} . Furthermore, the water in the central compartment of the cell can diffuse towards the feeding electrodes, with concomitant evolution of gaseous products due to water oxidation/reduction reactions.

In order to extend the number of materials which can be deposited by BPE, it is essential to increase the potential difference which can be imposed and maintained at the feeding electrodes. This can be achieved by decreasing the conductivity of the solution and hindering water reduction/oxidation at the feeder electrodes by substituting water with an aprotic dipolar solvent. Because of its electrical stability, capability to solvate and dissociate both suitable metal complexes and organic compounds, easy purification, as well as relatively low cost, we chose CH_3CN to this aim. Moreover, in order to evaluate the possibility to increase the polarization of the CMFs we deposited materials with a larger potential difference, namely gold and polythiophene (PT). Polythiophene is a conducting polymer which can be obtained by electrochemical oxidation of thiophene in acetonitrile solution [25, 26]. As far as Au is concerned, an acetonitrile soluble compound of this metal was used, namely the salt $[\text{TEA}(\text{AuCl}_4)]$.

Electrochemistry of AuCl_4^- in CH_3CN

Since the redox potentials of AuCl_4^- and thiophene in CH_3CN may significantly differ from their standard potentials in water solution, at first we studied their electrochemical behavior by voltammetric characterization. This preliminary study was necessary in order to determine the intensity of electric field to be applied to the CMF dispersion in acetonitrile, for obtaining a polarization high enough to trigger the desired electrochemical reactions.

Figure 4.5 (black line) shows the cyclic voltammogram recorded on 5 mM $[(\text{TEA})\text{AuCl}_4]$ in 0.1 M LiClO_4 acetonitrile solution at 25 mV s^{-1} using a GC disk as working electrode; the blue line is the blank CV recorded in the same supporting electrolyte. The forward scan is characterized by two peaks in the cathodic region, at -1.100 V (peak 1) and -1.700 V (peak 2), respectively. After reversing the scan direction at -2.000 V, the backward pattern presents 4 crossover points with the forward one. These features, together with the comparison with literature data [27-29] indicate that peaks 1 and 2, correspond to a two step gold reduction according to the following scheme:



In aqueous solution, the reduction of AuCl_4^- to metallic gold takes place in a single step via a three electron process [30, 31]. AuCl_2^- is not observed in aqueous solution because its formation is less favorable [27], so that the three electron reduction occurs, according to:



The different pathway in acetonitrile is probably related to the lower solubility of Cl^- in aprotic solvents than in water [27].

Note that when different voltammograms were recorded at the same scan rate, after polishing the electrode before each scan, the formation of intermediate AuCl_2^- (peak 1) was reproducible. Measurements performed by increasing the scan rate indicate that the current of peak 1 scales linearly with the square root of the scan rate, indicating a diffusion controlled process (Figure 4.5, inset).

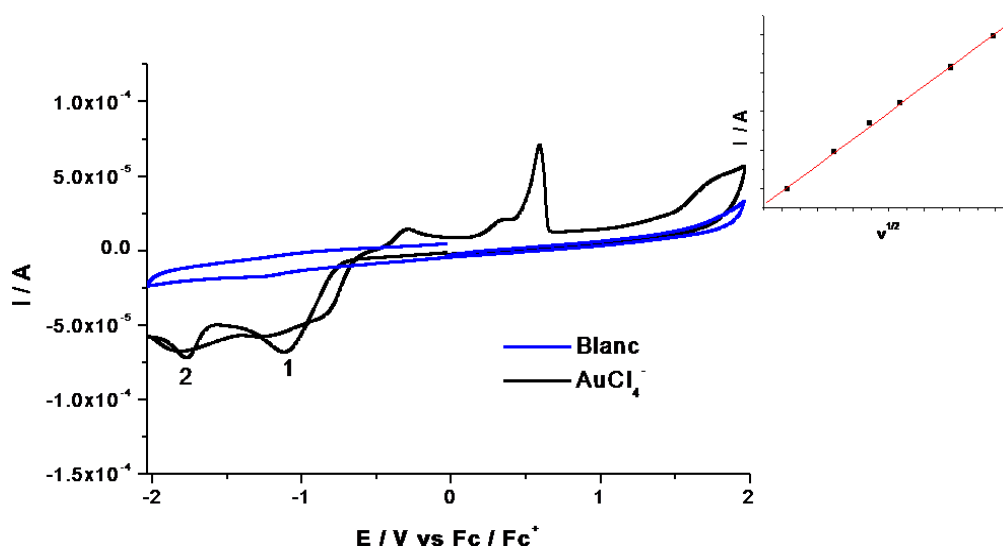
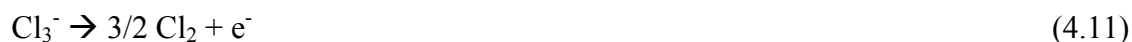


Figure 4.5. Cyclic voltammograms of a 5 mM AuCl_4^- , 0.1 M LiClO_4 in CH_3CN , (scan rate 50 mV s^{-1}). Inset, i_{p1} vs $v^{1/2}$ plot.

On the reverse oxidative sweep, a series of anodic peaks is detected at potential values more positive than -0.700 V , whose intensity is strongly affected by the scan rate. If the forward scan is limited to -1.500 V , i.e. including peak 1 only, peaks 3, 4 and 6 are not present and only peak 5 is detected (see Figure 4.6). Peak 3 and 4 are consistent with a two-step oxidation of Cl^- at a gold surface, previously described by Villagràn et al. [32], according to the following reactions:



Since peak 5 is present in both scans, it is consistent with Cl^- oxidation on the clean GC surface [33]. In the wide range scan, at more positive potentials, a broad peak is detected, which can be attributed to the oxidative dissolution of metallic gold formed at peak 2. The peak attribution is summarized in Table 4.1.

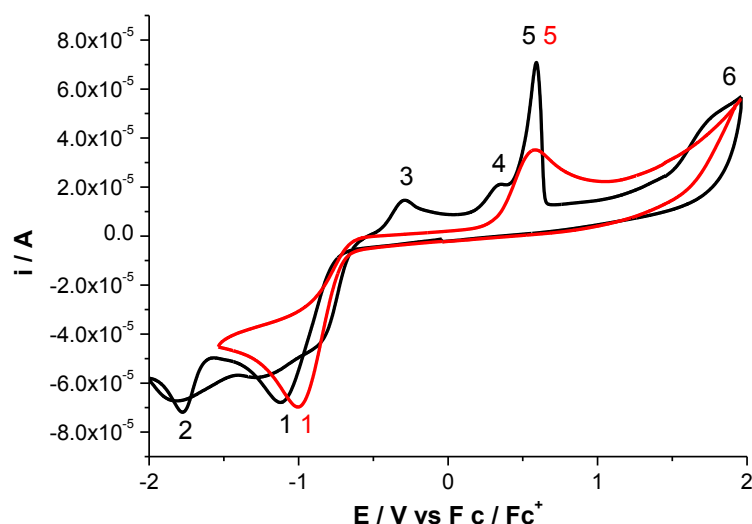


Figure 4.6. Cyclic voltammograms of a 5 mM AuCl_4^- CH_3CN solution.

Peak	Proposed Reactions
1	$\text{AuCl}_4^- + 2 \text{e}^- \rightarrow \text{AuCl}_2^- + 2 \text{Cl}^-$
2	$\text{AuCl}_4^- + \text{e}^- \rightarrow \text{Au} + 2 \text{Cl}^-$
3	$3 \text{Cl}^- \rightarrow \text{Cl}_3^- + 2 \text{e}^-$ (On Au nanoparticles)
4	$\text{Cl}_3^- \rightarrow 3/2 \text{Cl}_2 + \text{e}^-$ (On Au nanoparticles)
5	$2 \text{Cl}^- \rightarrow \text{Cl}_2 + 2 \text{e}^-$ (On GC surface)
6	$\text{Au} + \text{Cl}^- \rightarrow \text{AuCl} + \text{e}^- \rightarrow$ Oxidative dissolution

Table 4.1. Summary of the proposed reactions and peak assignments [33].

At variance with the AuCl_4^- case, the electrochemical behavior of thiophene in acetonitrile is already well known [25, 26], however its voltammetric behavior was revisited using the same experimental conditions as for the characterization of the Au complex. In particular, to the present

aims it was important to determine the thiophene potential with respect to the $E_{1/2}$ of the Fc/Fc^+ couple. The cyclic voltammogram of a 5 mM thiophene acetonitrile solution is reported in Figure 4.7. An intense anodic peak is detected at +1.425 V vs Fc/Fc^+ , consistent with the thiophene oxidation [25]. When thiophene is oxidized, a polymerization takes place, the product being oxidized polythiophene ($\text{PT}^{\delta+}$). This polymer shows conducting characteristics when electrons are added (n-doping) or removed (p-doping) from the conjugated π -orbitals. The essential structural characteristic of PT (and conducting polymers in general) is its conjugated system extending over a large number of recurrent monomer units. The electrical conductivity results from the delocalization of electrons along the polymer backbone, usually through overlap of π -orbitals, resulting in an extended π -system with a filled valence band. By doping the polymer as it is synthesized, a thick film can build up on an electrode because the polymer conducts electrons from the substrate to the surface of the film [34].

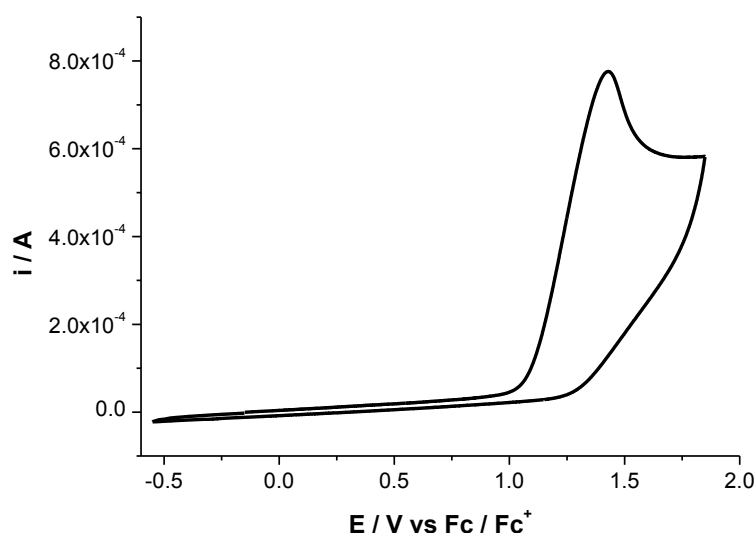


Figure 4.7. Cyclic voltammograms of a 5 mM thiophene in 0.1 M LiClO_4 CH_3CN solution. Scan rate 100 mV s^{-1} .

The polymerization mechanism of polythiophene is summarized in Scheme 4.8.

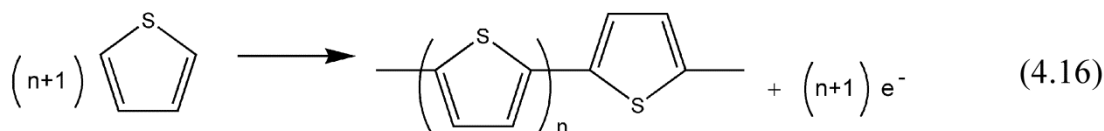
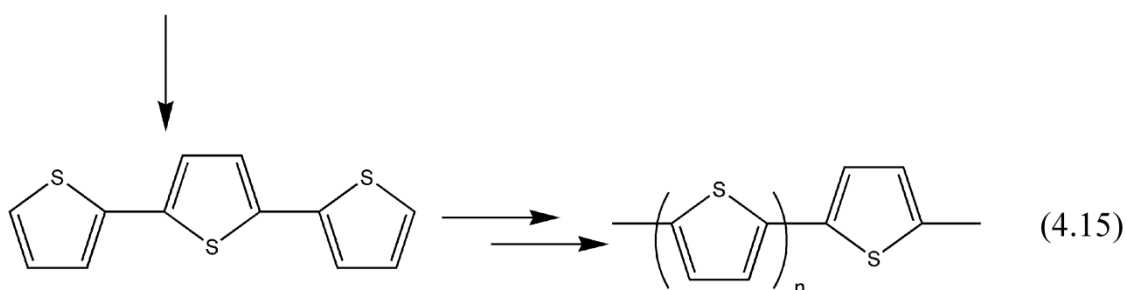
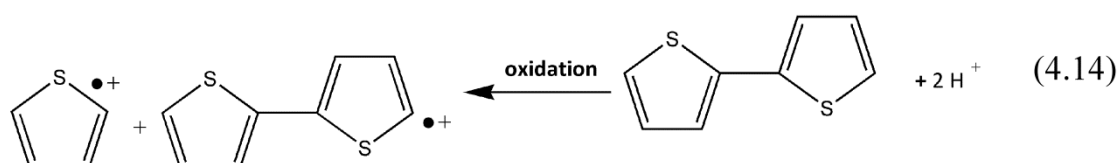
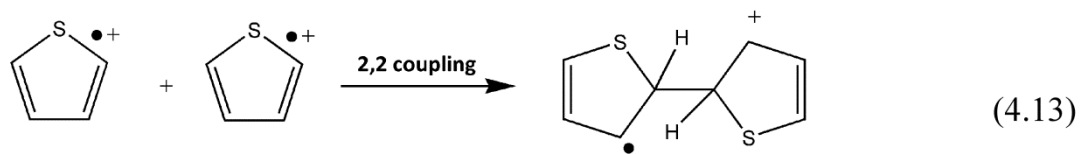


Figure 4.8. Electropolymerization mechanism of thiophene. Adapted from reference [35].

From the voltammograms reported in Figures 4.5 and 4.6, the reduction potential, for the gold deposition from AuCl_4^- in CH_3CN is -1.700 V vs Fc/Fc^+ . Note that, since the CV patterns both for AuCl_4^- and thiophene are not reversible, it is not possible to evaluate exactly E^0 values. However, an estimate of the difference in electrochemical potential (or electromotive force, EMF) to drive the electrochemical cell, in which reaction 4.8 is the cathodic process and reaction 4.16 is the anodic one, can be obtained by comparing relevant voltammetric peak potentials. Note that such a way of calculation takes into also account of eventual overpotentials necessary for making effectively operative the processes. In this case it results:

$$\text{EMF} = (E_{\text{AuCl}_4^-/\text{Au}^0}) - (E_{\text{C}_4\text{H}_4\text{S}/\text{C}_4\text{H}_4\text{S}^+}) = -1.700 \text{ V} - (1.425 \text{ V}) = -3.125 \text{ V}$$

Asymmetrical modification of GC microfibers by Bipolar Electrochemistry

Considering CMFs with a mean length of 300 μm , an electric field of 10.4 kV m^{-1} must be applied, in order to achieve a polarization of 3.125 V on the fibers. Since the distance between the feeder electrodes is 4 cm, a potential of 410 V must be applied between them. Taking into account that a potential drop is likely to occur at the glass septums of the cell, a potential of 600 V has been effectively applied in the experiments, resulting in an electric field of 12.5 kV m^{-1} . Figure 4.9 shows SEM images of CMFs recovered after the BPE experiment, modified by applying the above electric field for 5 minutes in a 2.5 mM AuCl_4^- , 15 mM thiophene acetonitrile solution, with no additional supporting electrolyte added. A metallic deposit is clearly visible on one end of the CMFs due to the different contrast between gold deposit and carbon substrate. The polythiophene end, instead, exhibits a weaker contrast with respect to the carbon fiber and therefore it is less clearly visible. In fact the production efficiency for backscattered electrons is proportional to the sample material's mean atomic number, i.e., higher atomic number material appears brighter than low atomic number material in a backscattered electron image. Note that the deposits are denser and thicker at the very end of the fibers. Moreover gold deposits protrude from the CMFs along the fibers direction confirming the presence a BPE mechanism; in fact the polarization is maximized at the extremities of the fibers. Note also that the amount of deposits increases with the length of the CMFs, since, a higher ΔV is generated between the extremities of longer fibers.

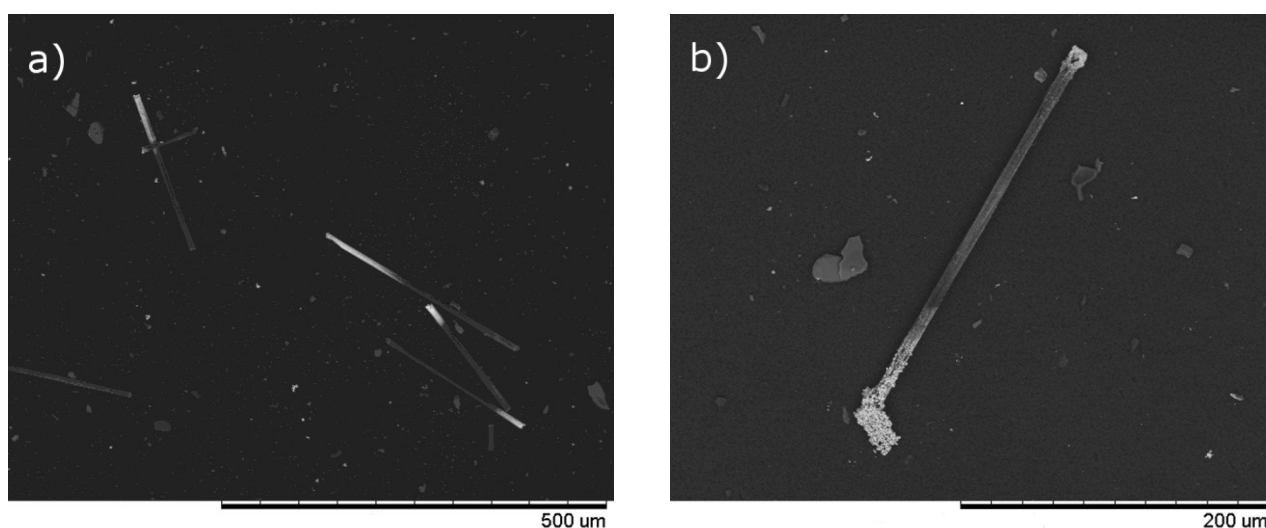


Figure 4.9. a) SEM image of CMFs asymmetrically functionalized with gold and polythiophene. b) Magnification of an asymmetrically modified CMF; a metal deposit is present on the lower tip, the polymer is visible on the upper one.

In order to confirm the nature of the deposits, EDX spectra have been recorded on the metallic end and on the organic end. Figure 4.10 shows that the metallic end is characterized by a strong Au signal around 2 and 10 keV and by a sharp carbon signal which originates most likely from the underlying carbon fiber. At the other end of the fiber (see Figure 4.11) the S signal is detected, confirming the presence of polythiophene. However, on the PT side there is still a small contribution from Au, and Cl atoms. These signals can be assigned to AuCl_4^- trapped as counterion in the polymer matrix during the monomer oxidation. In fact, during the electrochemical synthesis of a conducting polymer, counter ions dissolved in the solvent can associate with the polymer since the latter is deposited onto the electrode in its oxidized form [26].

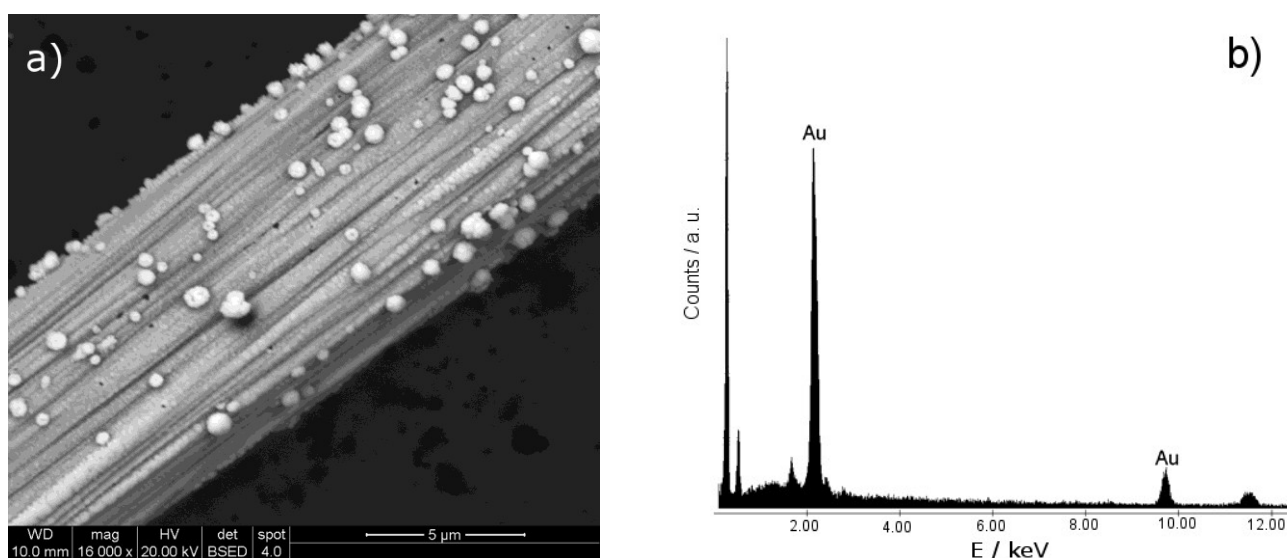


Figure 4.10. SEM image of a CMF gold modified tip (a). EDX spectra recorded for the same metalized tip (b).

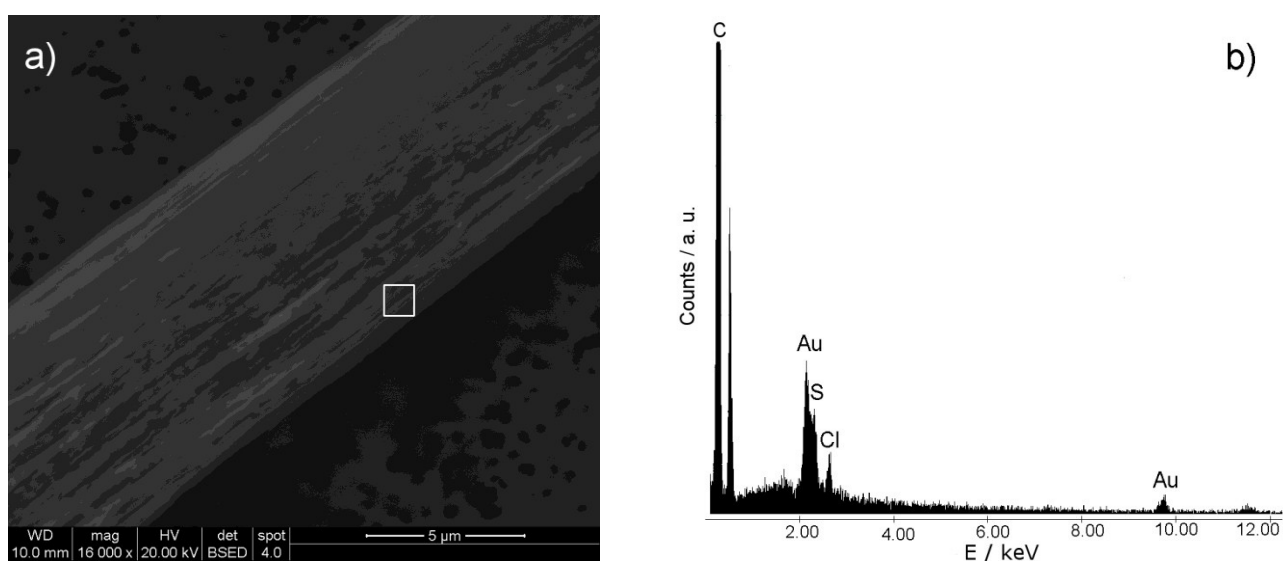


Figure 4.11. SEM image of a CMF PTmodified tip (a). EDX spectra recorded for the polymer modified tip (b).

Data in Figure 4.12 also demonstrates the possibility to control the shape and the dimension of the deposits on the fibers. By changing the deposition parameters, a direct effect on the morphology of the deposits is observed. If the electric field is imposed for a short time, namely, 1 minute, less Au and PT are deposited (see Figure 4.12a) and they coat a smaller portion of the fibers. When the redox species concentration is reduced, i.e. 1 mM AuCl_4^- and 5 mM thiophene, the deposits are thinner but, they cover a larger portion of the fibers (see Figure 4.12b).

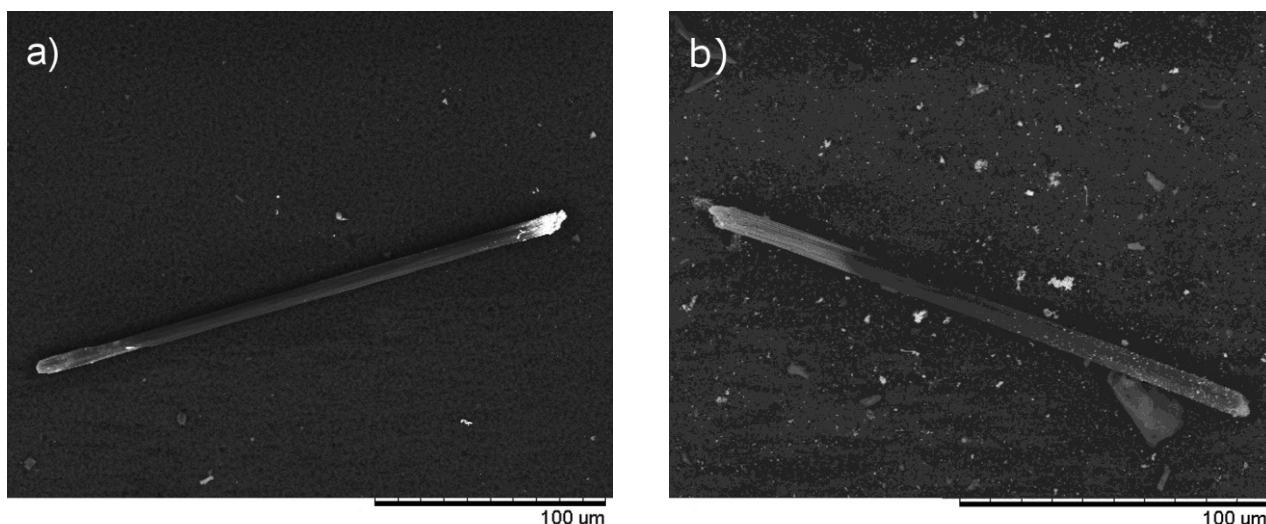


Figure 4.12. SEM images of modified CMFs with different BPE parameters: a) 2.5 mM AuCl_4^- 15 mM thiophene acetonitrile solution, deposition time 1 minute; b) 1 mM AuCl_4^- 15 mM thiophene acetonitrile solution, deposition time 5 minutes.

In order to verify the wider applicability of the method, we tried to deposit, by the same functionalization procedure, a different conducting polymer, namely polypyrrole. The modified CMFs were prepared in a 2.5 mM $[(\text{TBA})\text{AuCl}_4]$ and 15 mM pyrrole CH_3CN solution, applying an electric field of 12.5 kV m^{-1} for 5 minutes. In Figure 4.13 are reported the SEM images of CMFs after the functionalization. The deposits were characterized by EDX analysis. In Figure 4.14b the spectrum recorded on the metalized end of a carbon fiber is reported. The Au and C peaks are again clearly visible, confirming the gold deposition on the cathodic side of the fiber. At the other end of the CMF, the N signal arises, confirming the presence of polypyrrole (PPy). Again, on the polymer side, Au and Cl peaks are detected due to inglobation of metal salt as counter ion for the conducting polymer [26], (Figure 4.15b).

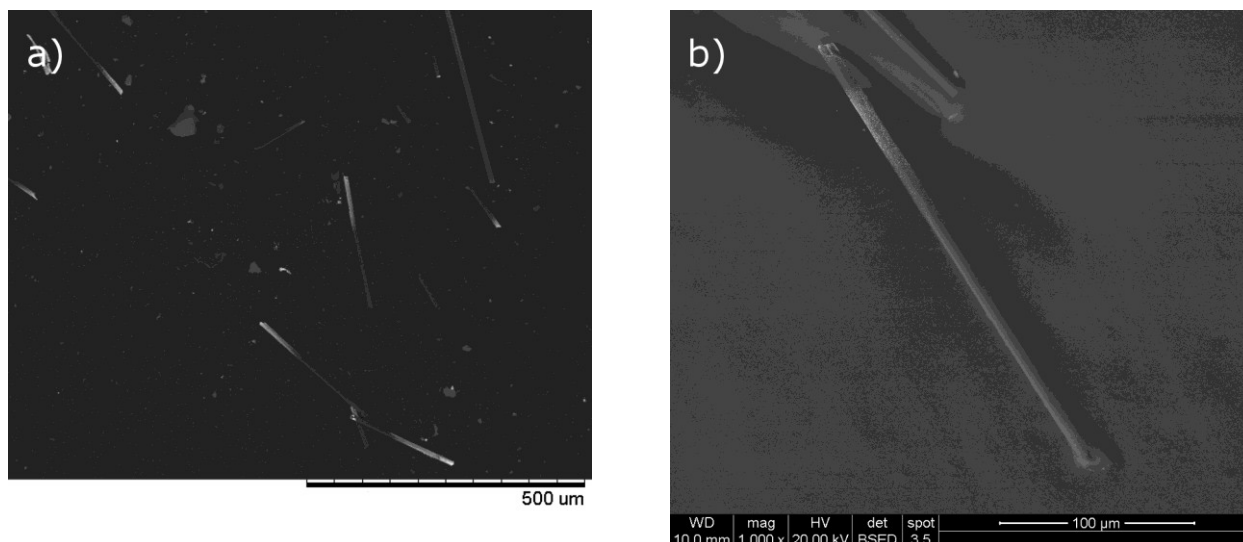


Figure 4.13. a) SEM image of CMFs asymmetrically functionalized with gold and polypyrrole. b) Magnification of an asymmetrically modified CMF; a metal deposit is present on the upper tip, the polymer is visible on the lower one.

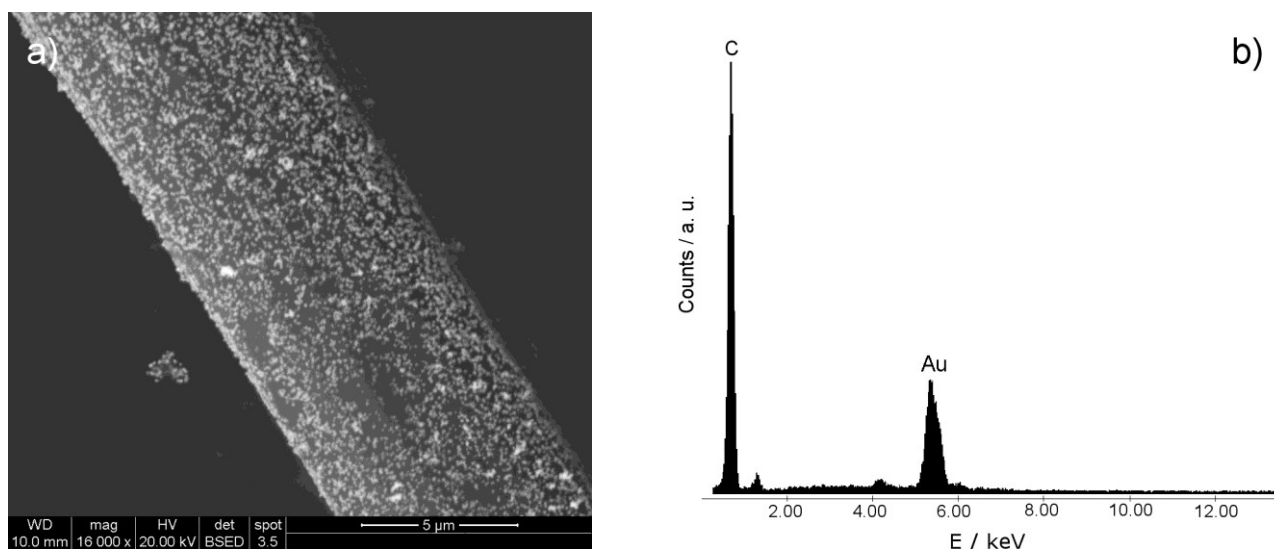


Figure 4.14. SEM image of a CMF gold modified tip (a). EDX spectra recorded from the same metalized tip (b).

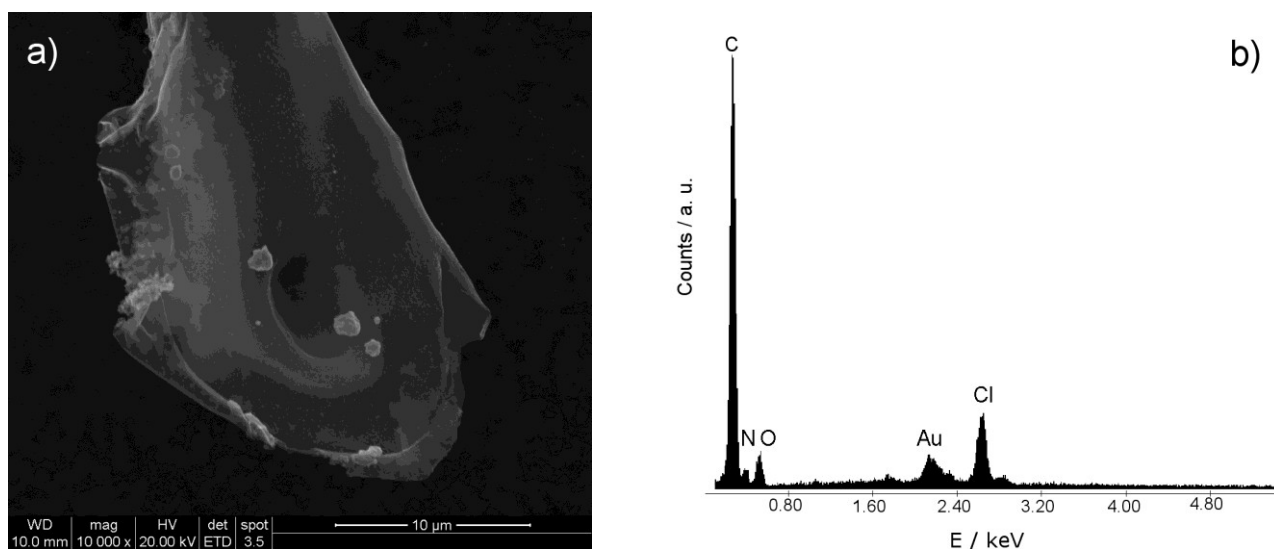


Figure 4.15. SEM image of a CMF PPY modified tip (a). EDX spectra recorded from the polymer modified tip (b).

Bipolar electrochemistry at semiconductor microfibers

In the previous section we demonstrated the possibility to exploit BPE for the modification of electrically conductive CMFs in an asymmetrical fashion. In the following section we will discuss the possibility to use BPE for the asymmetrical modification of semiconductor nanofibers. As already explained in chapter 1, the semiconductor electrochemistry differs in several points from conventional electrochemistry, in which conducting substrates/electrodes are used. Let's take into consideration BPE applied to an n-type semiconductor particle in the dark and under UV light irradiation (Figure 4.16). When the semiconductor particle is suspended in an electrolyte solution without UV irradiation (Figure 4.16a), a space charge region will form all over the particle surface., and if an external electric field is applied, a polarization will take place. The particle will be characterized by a cathodic side, rich in electrons (in the CB) and by an anodic side, poor in electrons (in the CB). The bands will bend accordingly to this polarization so that an accumulation layer will be generated on the cathodic side and a depletion or an inversion layer will be generated on the anodic side. In the anodic side, the hole concentration is very low, since in n-type semiconductors the VB is completely filled, and consequently the oxidation reactions will take place at a really slow extent. The accumulation layer, instead, is characterized by an excess of majority carriers (electrons), therefore the charge transfer ability of the cathodic side approaches that of a conductor particle. Anyway, the CB in a short time will be impoverished in electrons, because they are not replenished from the anodic side, and soon the reduction process will stop. However, when the particle is irradiated with light, the electrons will be promoted from the VB to the CB. At the same time, the holes left behind (in the VB) by the promoted electrons will accumulate on the anodic side, triggering oxidation reactions (see Figure 4.16b). Note that reduction by an electron in the CB can take place when E_{redox} lies below the CB lower edge; oxidation by holes in the VB can take place when E_{redox} lies above the upper edge of the VB.

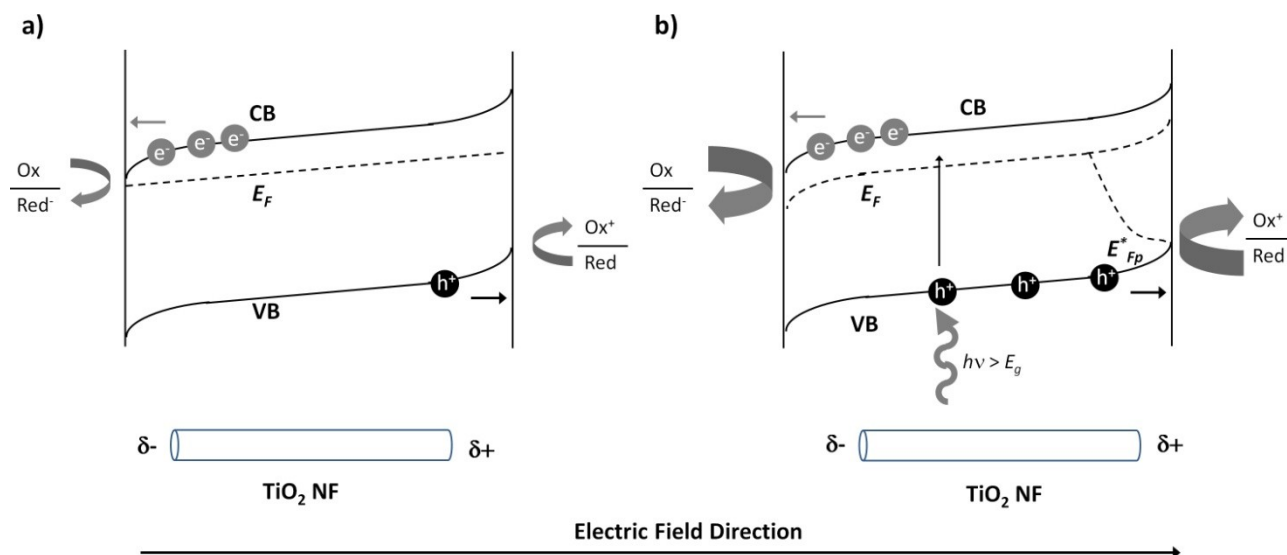


Figure 4.16. Schematic representation of photoelectrochemical mechanism of TiO₂ nanofibers inside an electric field in the dark (a) and under UV irradiation.

From a mechanistic view point, the energy needed to trigger the electrochemical reaction is mainly provided by the incident light, while the electric field allows an efficient charge separation and, more importantly, the generation of an asymmetric space charge region into the particle. This is particularly important in open configuration bipolar electrochemistry, in which reaching intense enough electric field may be an issue. In this thesis, the asymmetrical functionalization of TiO₂-NFs by photoassisted bipolar electrochemistry is studied for the first time. The electrochemical reactions exploited in the particle modification are AuCl₄⁻ reduction and thiophene polymerization.

At first, the mechanism was studied on a macroscopic substrate, using a semiconductor electrode. An ITO slide, 5 mm x 2 mm, covered with ZnO NW by the same procedure described in chapter 3 for the preparation of ITONO355002, was placed in the central compartment of a three compartment cell. The central compartment was also filled with 5 mM [(TEA)AuCl₄] and 20 mM thiophene acetonitrile solution. The outer compartments were filled with pure acetonitrile. An electric field of 200 V m⁻¹ was applied for 5 minutes shining the surface of the ZnO-ITO slide with UV light.

Note that the polarization generated on the substrate by this electric field is 1 V, which is not enough to achieve bipolar electrochemistry between these redox couples. In fact, a potential difference of at least 3.125 V was calculated in the previous paragraph.

In Figure 4.17 are reported the SEM images obtained from the ZnO-ITO slide after BPE under UV irradiation. On the anodic side of the slide a dark deposit is grown on the surface of ZnO NWs, on the opposite side, instead, metallic particles are visible on the surface of the NWs. The

morphology and the contrast of the deposits are consistent with PT and gold. The deposits were present exclusively at the extremities of the slide, no deposits were detected in the middle of the slide.

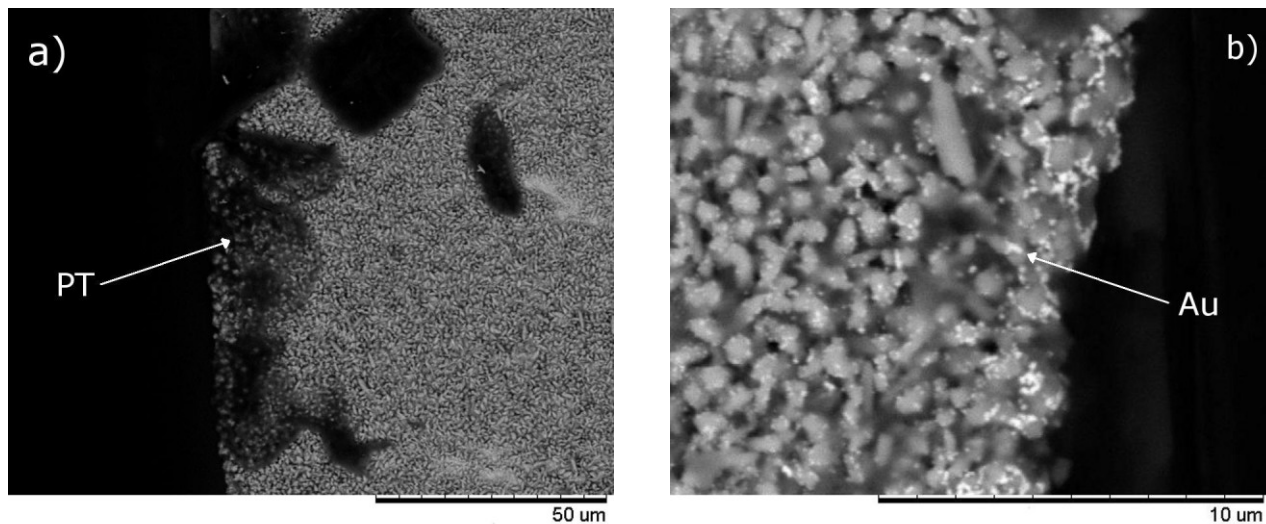


Figure 4.17. SEM images of the anodic (a) and cathodic (b) end of ZnO-ITO slide, after the application of an electric field of 200 V m^{-1} for 5 minutes under UV light irradiation.

When the same experiment was repeated in the dark, no deposits were observed on the ZnO NWs (see Figure 4.18).

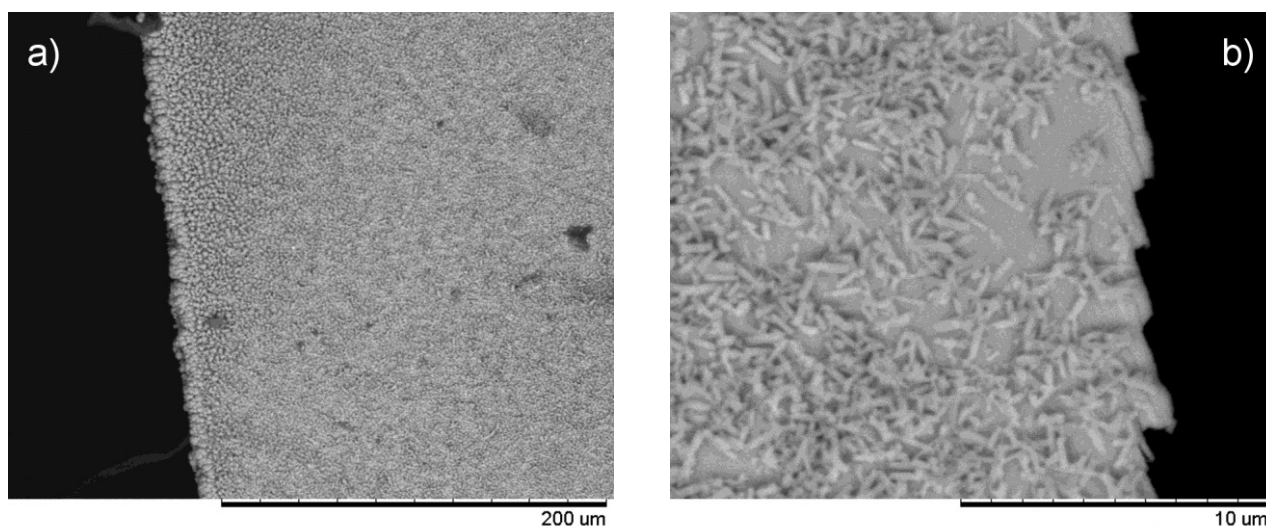


Figure 4.18. SEM images of the anodic a) and cathodic b) end of ZnO-ITO slide, after the application of an electric field of 200 V m^{-1} for 5 minutes in the dark.

These results confirm a photoassisted bipolar electrochemistry mechanism, in fact the slide was asymmetrically functionalized, applying an electric field which is not intense enough to allow the electrochemical reactions.

Encouraged by these evidences we tried to repeat the experiment in a micrometric scale, by using TiO₂-NFs as substrate. Note that ZnO and TiO₂ are considered interchangeable materials and are used for the same applications because they have comparable band gaps and their energy bands lie almost at the same energetic levels [36].

TiO₂-NFs were dispersed in a 2.5 mM [(TEA)AuCl₄] and 15 mM thiophene acetonitrile solution, and the suspension placed in the central compartment of the BPE cell. When an electric field of 15 kV m⁻¹ was applied for 5 minutes in the dark no deposits were observed, confirming the results obtained in the millimeter scale (see Figure 4.19). When no electric field was applied, but the suspension was irradiated for 5 minutes with UV light, small metallic deposits, randomly located all over the particles are clearly visible on the surface of the TiO₂-MF (see Figure 4.20). This confirms that the photogenerated electrons have enough energy to reduce AuCl₄⁻ to metallic gold. The organic deposits were not visible, but this may be due to a difficulty in detecting small polymer particles by using SEM.

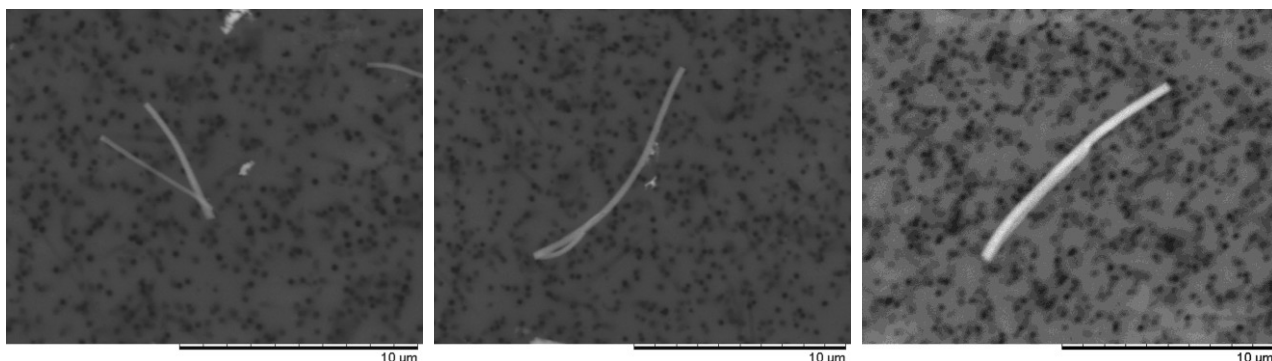


Figure 4.19. SEM images of TiO₂-NFs after the application of an electric field of 15 kV m⁻¹ for 5 minutes in the dark.

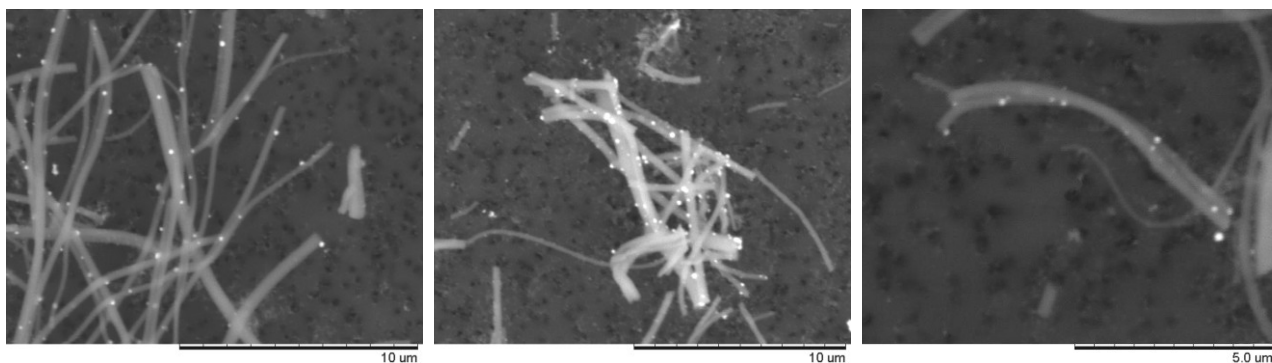


Figure 4.20. SEM images of TiO₂-NFs after 5 minutes irradiation with UV light.

When both UV light and electric field are applied at the same time on the TiO₂ NFs suspension, the metallic deposits were solely located at one tip of the NFs (see figure 4.21). The application of the external electric field allowed to restrict the electrochemical reactions to the tips of the nanofibers, allowing asymmetrical modification at relatively low electric field intensity.

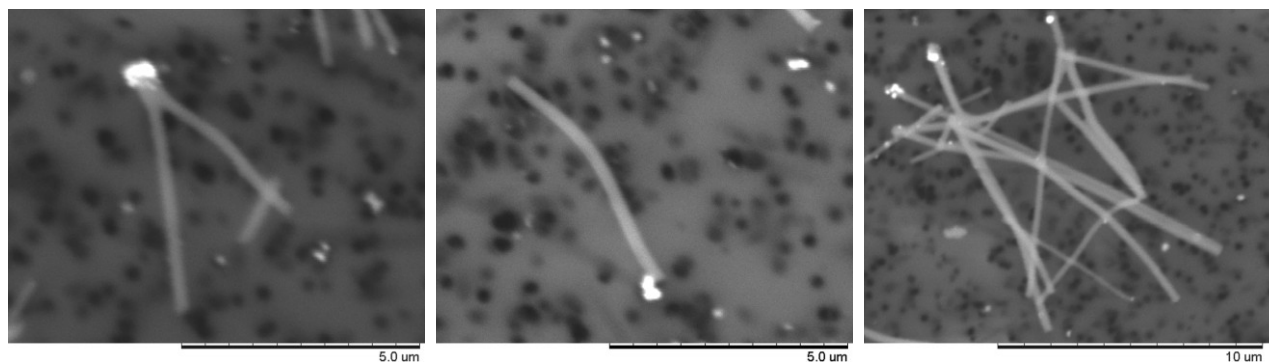


Figure 4.21. SEM images of TiO₂-NFs after the application of an electric field of 15 kV m⁻¹ for 5 minutes under UV irradiation.

4.4 Conclusions

BPE electrochemistry was successfully applied for the asymmetrical modification of conducting particles. Metals and conducting polymers were deposited, demonstrating the versatility of this technique. Moreover BPE was applied to the functionalization of TiO₂ nanofibers as small as 5 μm in length. In this case the electrochemical reactions proceeded through a photo-assisted mechanism, in which the UV light provided the energy necessary to the electrochemical reaction, while the electric field was responsible for the charge separation, restricting the deposition to the end of the NFs. Their synergic activity allowed to obtain asymmetrical modification of the NFs at an applied potential lower than the one to be applied on conducting particles of the same dimensions. The asymmetrical modification of anisotropic particles, allows to open a whole plethora of applications ranging from energy production, depollution, synthesis and analytical chemistry.

Moreover, since this technique does not require an interface to immobilize the particles, it can be considered a real 3D modification technique. Scaling up such a process, by using cell volumes in the liter range, would allow to synthesize a large number of asymmetrical particles. This is particularly important for mass scale production and eventually commercialization.

References

- [1] D. C. Eardley, D. Handley, S. P. S. Andrew, *Electrochim. Acta.* **18** (1973) 839
- [2] F. Goodridge, C. J. H. King, A. R. Wright, *Electrochim. Acta.* **22** (1977) 929
- [3] K. Kusakabe, S. Morooka, Y. Kato, *J. Chem. Eng. Jpn.* **15** (1982) 45
- [4] G. Pourcelly, *Russ. J. Electrochem. (Engl. Transl.)* **38** (2002) 919
- [5] G. Loget, A. Kuhn, *Anal. Bioanal. Chem.* **400** (2011) 1691
- [6] F. Mavré, R. K. Anand, D. R. Laws, K. F. Chow, B. Y. Chang, J. A. Crooks, R. M. Crooks, *Anal. Chem.* **82** (2010) 8766
- [7] D.-L. Lu, K.-I. Tanaka, *J. Phys. Chem. B* **101** (1997) 4030
- [8] H. J. Keh, W. J. Li, *J. Electrochem. Soc.* **141** (1994) 3103
- [9] C. Warakulwit, T. Nguyen, J. Majimel, M. H. Delville, V. Lapeyre, P. Garrigue, V. Ravaine, J. Limtrakul, A. Kuhn, *Nano Lett.* **8** (2008) 500
- [10] G. Loget, G. Larcade, V. Lapeyre, P. Garrigue, C. Warakulwit, J. Limtrakul, M. H. Delville, V. Ravaine, A. Kuhn, *Electrochim. Acta* **55** (2010) 8116
- [11] Z. Fattah, G. Loget, V. Lapeyre, P. Garrigue, C. Warakulwit, J. Limtrakul, L. Bouffier, A. Kuhn, *Electrochim. Acta* **56** (2011) 10562
- [12] J. Lueke, W.A. Moussa *Sensors* **11** (2011) 1433
- [13] S. Pradhan, D. Ghosh, S. Chen, *ACS Appl. Mater. Interfaces* **1** (2009) 2060
- [14] X. Fu, J. Liu, H. Yang, J. Sun, X. Li, X. Zhang, Y. Jia, *Mater. Chem. Phys.* **130** (2011) 334
- [15] A. J. Bard, L. R. Faulkner, *Electrochemical Methods* (1980) Wiley, New York
- [16] X. Liu, L. Zhang, Y.-B. L. , L.-J. Bian, Z. Su, L.-J. Zhang, *J. Mat. Sc.* **22** (2005) 2461
- [17] R. W. Murray, *Acc. Chem. Res.* **13** (1980) 135
- [18] M. E. G. Lyons, *Electroactive Polymer Electrochemistry Part. 1: Fundamentals* (1994) Plenum Press, New York
- [19] C. Simionescu, I. Cianga, M. Grigoras, *Roum. Chem. Quart. Rev.* **3** (1995) 3
- [20] E. M. Genies, A. A. Syed, C. Tsintavis, *Mol. Cryst. Liq. Cryst.* **57** (1984) 2254
- [21] D. M. Mohilner, R. N. Adams, W. J. Argersinger Jr., *J. Am. Chem. Soc.* **84** (1962) 3618
- [22] C. Q. Cui, L. H. Ong, T. C. Tan, J. Y. Lee, *Synthetic Met.* **58** (1993) 147
- [23] A. J. Bard, R. Parsons, J. Jordan, *Standard Potentials in Aqueous Solution* (1985) Marcel Dekker Inc., New York
- [24] D. Bejan, A. Duca, *CCACAA* **71** (1998) 745
- [25] J. Roncali, *Chem. Rev.* **92** (1992) 711
- [26] M. Can, K. Pekmez, N. Pekmez, A. Yildiz, *Synthetic Met.* **104** (1999) 9

- [27] L. M. A. Monzon, F. Byrne, J. M. D. Coey, *J. Electroanal. Chem.* **657** (2011) 54
- [28] A. D. Goolsby, D. T. Sawyer, *Anal. Chem.* **40** (1968) 1978
- [29] U. Koelle, A. Laguna, *Inorg. Chim. Acta* **290** (1999) 44
- [30] K. B. Holt, G. Sabin, R. G. Compton, J. S. Foord, F. Marken, *Electroanal.* **14** (2002) 797
- [31] O. M. Magnussen, K. Kryg, A. H. Ayyad, J. Stettner, *Electrochim. Acta* **5** (2008) 3449
- [32] C. Villagràn, C. E. Banks, C. Hardacre, R. G. Compton, *Anal. Chem.* **76** (2004) 1998
- [33] L. Aldous, D. S. Silvester, C. Villagràn, W. R. Pitner, R. G. Compton, M. C. Lagunas, C. Hardacre, *New J. Chem.* **30** (2006) 1576.
- [34] J.-C. Vidal, E. Garcia-Ruiz, J.-R. Castillo, *Electrochim. Acta* **49** (2004) 2031
- [35] S. Sadki, P. Schottland, N. Brodie, G. Sabouraud, *Chem. Soc. Rev.* **29** (2000) 283
- [36] Q. Zhang, C. S. Dandeneau, X. Zhou, G. Cao, *Adv. Mater.* **21** (2009) 1

5. Concluding Remarks

In this thesis, different ceramic metal oxide nanostructures were prepared by using different synthetic procedures (chapter 2-3). The obtained nanomaterials were tested as photoanodes for improving the performances of photoelectrochemical cells in reaction of interest in the energy field. A sol-gel templated procedure, for the preparation of TiO₂-anatase nanofibers, was developed using track-etched porous membranes as structure directing agents. By this procedure, arrays of self standing nanowires, with diameter as small as 200 nm and with an aspect ratio of 30, were obtained. Unfortunately it was not possible to obtain an effective electrical contact between the TiO₂ nanofibers array and a transparent conductive electrode, without disrupting the long range structure of the semiconductor material. Therefore it was not possible to fully exploit the potentials of this material, which are fast electron transport and electron-hole separation efficiency. These characteristics are maximized when the orientation of the nanofibers allows a direct path from the tips of the nanofibers to the electrode substrate. This limit was overcome by testing an alternative synthetic approach. To this aim, the electrochemical deposition of ZnO nanofibers on a flat ITO substrate was studied and the best deposition conditions were found. The photoelectrochemical tests performed on these structures showed a significant improvement in the photocurrent when compared with TiO₂ nanoparticles electrode or TiO₂ nanofibers electrode, demonstrating the advantage of using ordered quasi 1-D nanostructures for photoelectrochemical applications. With the goal to increase the surface area of ZnO nanofibers, keeping the electron transport efficiency as high as possible, we studied the deposition of branched nanofibers, using a Au-3D-NEE as substrate in the ZnO deposition. The electrodes obtained are characterized by the presence of ZnO branched nanofibers. These hierarchically structured nanofibers showed further improved performances, furnishing higher water oxidation photocurrents in comparison with the other above listed electrode materials. These results demonstrate the importance to tailor the morphology of the nanostructures on the final application it is designed for. With the purpose of characterizing these nanomaterials, we demonstrated that EBSD can be used as an efficient analytical technique for phase identification analysis of complex nanostructures such as the ZnO nanofibers prepared here. The obtained results support the application of this technique as a valuable alternative to XRD analysis, with the great advantage of obtaining precise structural information on individual nanoobjects.

Further efforts should be devoted to sensitize these promising structures in order to allow visible light adsorption, improving their applicability in the field of solar energy conversion. To this aim, the integration of branched ZnO nanofibers in DSSCs will be a future goal.

Concluding Remarks

In the last chapter, a novel technique for the asymmetrical modification of micro and nano-objects was studied. Bipolar electrochemistry was developed, over the last years, in the NSysA laboratories, at the Institute of Molecular Sciences (ISM) of the University of Bordeaux, where part of this specific work was done. At first, the asymmetrical modification of carbon microfibers with metals and conducting polymers was studied. Particular focus was put on optimizing the experimental conditions for the deposition of gold (on one side of carbon fibers) and conducting polymers (on the other), in acetonitrile solution. It is worth noting that, for this goal, we gained fundamental informations on the electrochemistry of an Au(III) complex soluble in acetonitrile, namely [TEA(AuCl₄)]. These informations and know-how so acquired were applied to the asymmetrical modification of TiO₂ nanofibers by bipolar electrochemistry. We demonstrated that the integration of UV irradiation with the application of a strong electric field to an acetonitrile dispersion of TiO₂ nanofibers, allow one to perform the asymmetrical deposition of two different materials at the opposite sides of the semiconductor nanowires. From the evidences presented, the mechanism of the process can be described as photoassisted bipolar electrochemistry, since the incident light provides the driving force for the electrochemical reactions by exciting electrons to the conduction band and producing holes in the valence band, while the external field has the purpose to efficiently separate the photogenerated charges, confining them at the opposite ends of the fibers, where the electrochemical reactions take place. At the best of our knowledge, this is the first time that bipolar electrochemistry and light irradiation are used for the synergic asymmetric modification of semiconductor nanoobjects.

Appendix A

Basics of EBSD

For EBSD, a beam of electrons is focused on the point of interest on a tilted crystalline sample in the SEM. The mechanism by which the diffraction patterns are formed is complex, but the following describes the principal features. The atoms in the material inelastically scatter a fraction of the electrons, with a small loss of energy, to form a divergent source of electrons close to the surface of the sample. Some of these electrons are incident to atomic planes at angles which satisfy the Bragg equation:

$$n\lambda = 2d \sin\theta$$

where n is an integer, λ is the wavelength of the electrons, d is the spacing of the diffraction planes, and θ is the angle of the incidence of the electrons on the diffracting plane. When used to form an image on the fluorescent screen, the regions of enhanced electron intensity between the cones produce the characteristics Kikuchi bands of electron backscatter diffraction pattern.

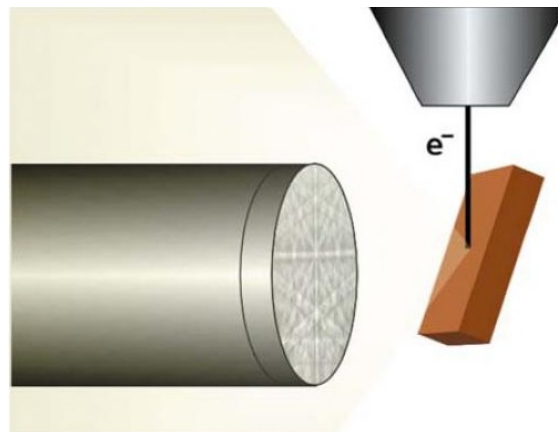


Figure A1. Representation of SEM chamber showing the typical experimental arrangement for EBSD

The center lines of the Kikuchi bands correspond to the projection of the diffracting planes on the phosphor screen. Hence, each Kikuchi band can be indexed by the Miller indices of the diffracting crystal plane which formed it. Each point on the phosphor screen corresponds to the intersection of a crystal direction with the screen. In particular, the intersections of Kikuchi bands

correspond to the intersection of zone axes in the crystal with the phosphor screen. These points can be labeled by the crystal direction for the zone axis.

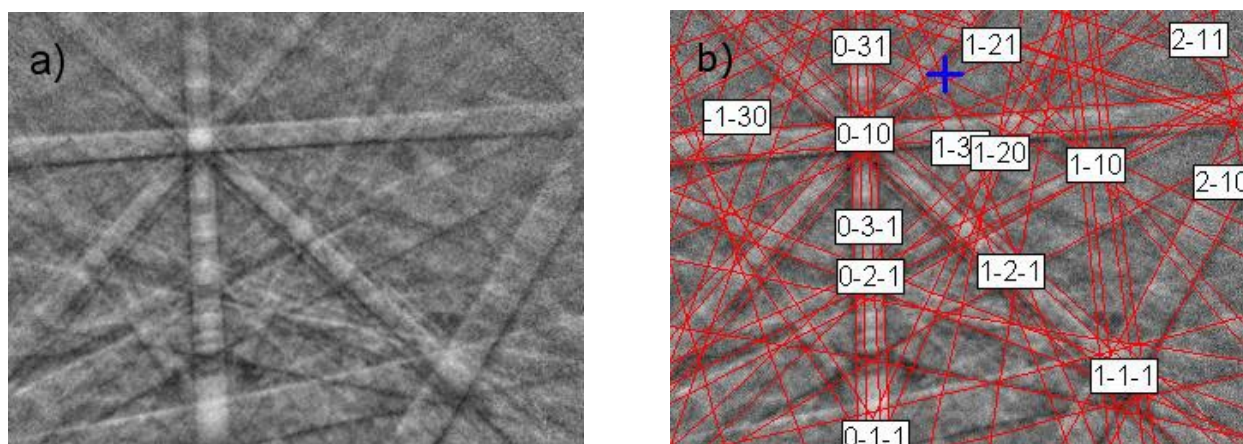


Figure A2. Diffraction pattern from nickel, collected at 20 kV accelerating voltage (a). Indexed diffraction pattern (b).

The pattern is a gnomonic projection of the diffracted cones of electrons onto the phosphor screen. Consider a sphere with center O and point P on its surface. The projection plane is the plane tangent to the sphere at its north pole N . The line OP intersects the projection plane at p , and this point is the gnomonic projection of P . The line LM is gnomonic projection of the plane with normal OP . For EBSD, O is the point on the sample where the diffracted electrons are generated, the projection plane is the phosphor screen and N is the pattern center. Electrons are diffracted into a region defined by a pair of cones with axes normal to the diffracting plane and semi angle $(90 - \theta)$, where θ is the Bragg angle. The gnomonic projections of these cones are the edges of the Kikuchi bands are the gnomonic projection of the crystal plane the centre lines of the Kikuchi bands. The edges of the bands project as hyperbolae onto phosphor screen. However, because the cone semiangle is close to 90° these appear as straight lines on the diffraction pattern, although further from the pattern centre the hyperbolic shape can be seen^{2,3}.

² A. R. Schwarzer, D. P. Field, B. L. Adams, M. Kumar, A. J. Schwartz, in: A. J. Schwartz, M. Kumar, B. L. Adams, D. P. Field (Eds.) *Electron Backscatter Diffraction in Materials Science* (2009) Springer, Berlin

³ J. A. Small, J. R. Michael, *J. Microsc.-Oxford* **201** (2001) 59

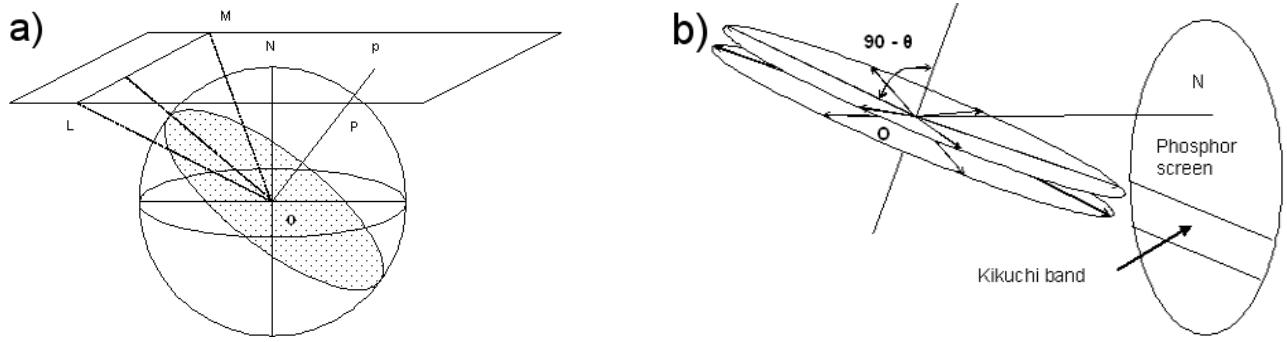


Figure A3. The gnomonic projection. The line LM is the gnomonic projection of the plane with normal OP (a). Gnomonic projection in EBSD (b).

Appendix B

Publications in international journals and books

- Michael Ongaro, Arianna Gambirasi, Monica Favaro, Paolo Ugo, Electrochemical Synthesis and Characterization of Hierarchically Branched ZnO Nanostructures on Ensembles of Gold Nanowires. *Electrochim. Acta*, 2012, 78, 539.
- Michael Ongaro, Paolo Ugo, Bioelectroanalysis with Nanoelectrode Ensembles and Arrays, *Anal. Bioanal. Chem.*, in press.
- Michael Ongaro, Paolo Ugo, Voltammetric Nanoelectrode Ensembles Based on Templated Metal Nanowires in Track-Etched Polymer Membranes, in: S. Inamuddin (Ed.) *Advanced Functional Polymers and Composites: Materials, Devices and Allied Applications*, Nova Science Publishers, New York, in press.

Oral presentations to national/international scientific meetings

- YISAC 2010, Venice (June 29th – July 1st 2010): “Metal Oxide Nanofibres for Sensing Applications by Improved Sol-Gel Template Synthesis”. Michael Ongaro, Andrea Mardegan, Paolo Ugo
- YISAC 2011, Novi Sad (June 28th – July 1st 2011): “3-D Ensembles of Linear and Branched Semiconductor Nanoelectrodes for Gas Sensing and Photoelectrochemical Applications”. Michael Ongaro, Arianna Gambirasi, Monica Favaro, Paolo Ugo
- YISAC 2012, Nova Gorica (June 27th - June 30th 2012): “Electrochemical Synthesis and Characterization of Hierarchical Branched Nanostructures: ZnO Nanorods on Ensembles of Gold Nanowires”. Michael Ongaro, Arianna Gambirasi, Monica Favaro, Paolo Ugo

Poster contributions to national/international scientific meetings

- SCI 2010, Como (September 12th – 16th 2010): “Metal Oxide Nano-fibers for Sensing Applications by Improved Sol-Gel Template and Electrochemical Synthesis”. Michael Ongaro, Andrea Mardegan, Alessandro Patelli, Paolo Scopece, Paolo Ugo
- ISE 2010, Nice (September 26th – October 1st 2010): “TiO₂ Nanofibers for Energy Conversion by Improved Sol-Gel Template Synthesis”. Michael Ongaro, Andrea Mardegan, Paolo Scopece, Alessandro Patelli, Paolo Ugo
- ELECNANO 4, Paris (May 23rd – 26th 2011): “3-D Ensembles of Linear and Branched ZnO Nanoelectrodes for Photoelectrochemical Applications”. Michael Ongaro, Arianna Gambirasi, Monica Favaro, Paolo Ugo
- ISE 2012, Prague (August 19th - 4th 2012): “Electrochemical Synthesis and Characterization of Hierarchical Branched Nanostructures: ZnO Nanorods on Ensembles of Gold Nanowires”. Michael Ongaro, Arianna Gambirasi, Monica Favaro, Paolo Ugo